<center>═══════════ **PHYSICS** ═══════════</center>

Electromagnetically Induced Transparency and Controlling the Time Shape of Laser Pulses

V. G. Arkhipin and I. V. Timofeev

Presented by Academician V.F. Shabanov October 26, 2004

Received October 26, 2004

1. The development of new methods for controlling optical properties of a medium and the time shape of laser pulses is an important physical problem of fundamental and applied significance. The solution of this problem is urgently required in the areas of spectroscopy of fast processes, quantum control of atoms and molecules, optoelectronics and optical communication, etc. From this standpoint, the phenomenon of electromagnetically induced transparency (EIT) presents extremely interesting and rather unique opportunities [1–3]. Although the majority of studies on EIT have been carried out for atomic media (see reviews [3–6] and references therein), the relevant ideas have also undergone further development in the context of solid-state systems [7].

EIT is a quantum-interferential phenomenon arising as a result of the interaction between two laser fields and a three-level quantum system. The essence of the phenomenon is that one of the fields, called the controlling field, modifies the optical state of a medium at the frequency of the other (probe) field. In the general case, the intensity of the probe field may be comparable with that of the controlling field. Under conditions of EIT, the substance turns out to be in a coherent state with unusual properties [3–6]. For example, an optically dense medium becomes transparent for the probe field in the single-photon resonance region, whereas the dispersion of the refractive index strongly increases. Under these conditions, optical pulses can run to distances significantly exceeding the resonance length of the single-photon absorption (see, e.g., [8, 9]). The controlling field can control the group velocity of the probe-pulse propagation and can even reduce this velocity down to zero or to a negative value [5]. At group velocities on the order of 1–100 m s^{-1}, a spatial compression of the probe pulse occurs. As a result, it is completely localized in a medium. This phenomenon makes it possible to write down, store, and read out

_____

Kirenskiĭ Institute of Physics, Siberian Division,
Russian Academy of Sciences, Akademgorodok,
Krasnoyarsk, 660036 Russia
e-mail: avg@iph.krasn.ru; tiv@iph.krasn.ru

optical pulses [5, 6, 10] and opens the door to new approaches to the development of quantum memory [6].

EIT is used for controlling characteristics of optical radiation, for example, the generation of femtosecond and subfemtosecond pulses (see, e.g., [11]). At present, methods of controlling femtosecond pulses are developed sufficiently well and are applied in spectroscopy, microscopy, and optical monitoring [12]. However, the situation is not so good in the case of picosecond and nanosecond pulses.

In this paper, we discuss a new possibility for controlling the shape and duration of laser pulses on the basis of the EIT phenomenon. Using as an example the time compression of pulses, we now consider the principal concept of the control. Let the probe pulse propagate inside a three-level medium in the presence of a coupling pulse interacting with the adjacent transition (Fig. 1). The envelope of the latter pulse varies with time according to a certain law. Since, in the case of EIT, the propagation velocity of the probe pulse depends on the coupling-pulse intensity at a given instant of time, different parts of the probe pulse move at different velocities. It is important that one can control this velocity by variation of the coupling-pulse shape. For example, the envelope of the coupling pulse at the boundary of the medium can be chosen in a manner such that the propagation velocity of the trailing edge of the probe pulse will be higher than the velocity of its leading edge. As a result, the pulse is compressed with time. Varying the shape of the coupling pulse, it is possible to obtain various shapes for the probe-pulse envelope.

Thus, we here propose an efficient method for controlling the shape and duration of laser pulses, which is based on employing additional controlling radiation that interacts with the adjacent transition under conditions of EIT.

2. We now consider the interaction between a three-level medium and two optical pulses possessing envelopes $E_p(t)$ and $E_c(t)$ (Fig. 1). These pulses propagate in the same direction along the z axis. Probe pulse E_p resonantly interacts with the transition between the ground $|0\rangle$ and excited $|1\rangle$ states, whereas coupling pulse E_c interacts with levels $|2\rangle$ and $|1\rangle$. The dipole $|2\rangle$–$|0\rangle$
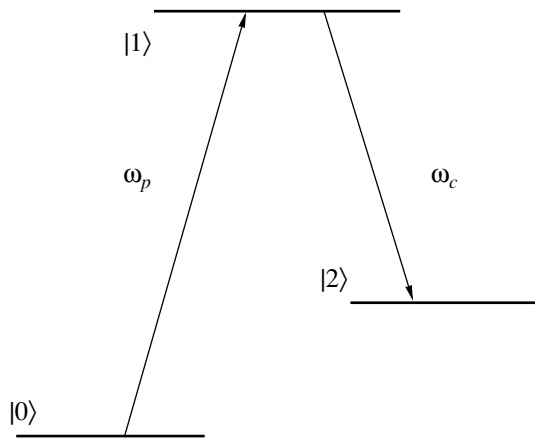
Fig. 1. Energy diagram for a three-level atom resonantly interacting with a probe (ω_p) and coupling (ω_c) pulse.

transition is forbidden. Further, we suggest that pulse durations T_p and T_c are much shorter than all relaxation times and that $T_p < T_c$.

The evolution of the probe and coupling pulses is described by the usual self-consistent set of Maxwell–Schrödinger equations. In the coordinate system with the local time $\tau = t - \dfrac{z}{c}$, this set is of the form

$$\frac{\partial a_0}{\partial \tau} = iG_p^* a_1, \quad \frac{\partial a_2}{\partial \tau} = iG_c^* a_1,$$
$$\frac{\partial a_1}{\partial \tau} = i(G_p a_0 + G_c a_2), \tag{1}$$

$$\frac{\partial G_p}{\partial z} = iK_p a_1 a_0^*, \quad \frac{\partial G_c}{\partial z} = iK_c a_1 a_2^*. \tag{2}$$

Here, $a_{0,1,2}$ are the amplitudes of atomic-state probabilities; $2G_p = \dfrac{d_{10}E_p}{\hbar}$, $2G_c = \dfrac{d_{12}E_c}{\hbar}$ are Rabi frequencies; $K_p = \pi\omega_p|d_{10}|^2\dfrac{N}{\hbar c}$, $K_c = \pi\omega_c|d_{12}|^2\dfrac{N}{\hbar c}$ are the propagation coefficients; d_{ij} are the matrix elements of the electric dipole moment for the $|i\rangle$–$|j\rangle$ transition ($i, j = 0, 1, 2$); $\omega_{p,c}$ and $k_{p,c}$ are the carrier frequencies and wave numbers (in vacuum), respectively; N is the atomic concentration; and c is the speed of light in vacuum.

Equations (1) for probability amplitudes are written for zero single-photon detunings $\omega_{10} - \omega_p = \omega_{12} - \omega_c = 0$. We consider all atoms to be in the ground state $|0\rangle$ at the initial instant of time; i.e., $a_0(-\infty, z) = 1$, $a_1(-\infty, z) = a_2(-\infty, z) = 0$, and the fields $E_{p,c}(t)$ being given at the medium boundary $z = 0$: $E_{p,c}(t, z = 0) = E_{0p,0c}(t)$.

Equations (1) and (2) must be solved by a self-consistent method. In the general case, this procedure can be realized numerically. An essential simplification is

attained in the adiabatic approximation [13]. In this case, the solution to set (1) can be represented in the form (see, e.g., [8, 9])

$$a_0 = \cos[\theta(\tau)], \quad a_2 = -\sin[\theta(\tau)],$$
$$a_1 = -\frac{G_c\dot{G}_p - G_p\dot{G}_c}{G^3} = i\frac{\dot{\theta}}{G}. \tag{3}$$

The displacement angle θ is defined by the expression $\tan\theta = \dfrac{G_p}{G_c}$, where $G(\tau) = \sqrt{|G_p(\tau)|^2 + |G_c(\tau)|^2}$ is the generalized Rabi frequency. The dot from above denotes differentiation with respect to the local time τ: $\dot{\theta} = \dfrac{\partial\theta}{\partial\tau}$, etc. In the general case, envelopes G_p and G_c depend on the z coordinate.

The criterion of applicability for the adiabatic approximation can be written as

$$\left|\frac{\dot{G}_c G_p - \dot{G}_p G_c}{G^3}\right| \ll 1. \tag{4}$$

A detailed analysis of the adiabaticity condition with allowance for pulse propagation has been performed in [9].

It follows from formulas (3) and (4) that, in the adiabatic limit, the population of the intermediate state in the interaction process is close to zero, ($|a_1| \ll 1$). This implies that for transitions $|0\rangle$–$|1\rangle$ and $|2\rangle$–$|1\rangle$ the absorption is small. Therefore, the pulses run to a distance that considerably exceeds the length of the resonance linear absorption of probe radiation. This phenomenon is also interpreted in terms of coherent population trapping (CPT): atoms are excited into a coherent superposition of lower states $|0\rangle$ and $|2\rangle$, which is called the CPT state, or dark state [14]. In this state, atoms cease to interact with optical pulses. The EIT phenomenon arises as a result of this process.

Using expression (3), we can represent Eq. (2) in the form

$$\frac{\partial G_p}{\partial z} = -K_p\frac{\dot{\theta}}{G}\cos\theta, \quad \frac{\partial G_c}{\partial z} = K_c\frac{\dot{\theta}}{G}\sin\theta. \tag{5}$$

In the general case, the set of Eqs. (5) can be solved only numerically.

For $K_p = K_c$, it is easy to show from (5) that the generalized Rabi frequency G is independent of the z coordinate:

$$G(\tau, z) = G(\tau, z = 0)$$
$$= G_0(\tau) = \sqrt{|G_{0p}(\tau)|^2 + |G_{0c}(\tau)|^2}. \tag{6}$$

From this, it follows that arbitrary variations occurring in the probe field are compensated by corresponding
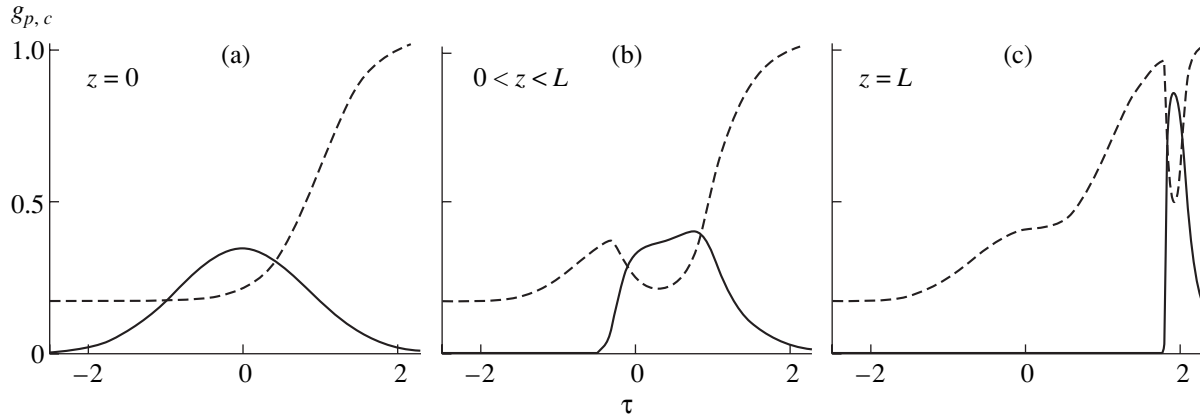
Fig. 2. Time profile of normalized Rabi frequencies for the probe pulse $g_p = \dfrac{G_p(\tau)}{G_{\max}}$ ($G_{\max}$ is the maximum value of the effective

Rabi frequency) and coupling pulse $g_c = \dfrac{G_c(\tau)}{G_{\max}}$ (dashed curve) in the case of different values of z coordinates inside the medium:

(a) at the input of the medium, $z = 0$, $G_p(\tau = 0, z = 0)$ $T_p = 20$; (b) at a certain distance z; and (c) at the output of the medium, $z = L$.

changes in the controlling field. In this case, the set of Eqs. (5) is reduced to one equation for $\theta(\tau, z)$:

$$\frac{\partial \theta}{\partial \tau} + \frac{G_0^2(\tau)}{K}\frac{\partial \theta}{\partial z} = 0. \qquad (7)$$

The solution to Eq. (7) can be written as

$$\theta(\tau, z) = \theta_0(Z^{-1}(Z(\tau) - z)) = 0, \qquad (8)$$

where $Z(\tau) = K^{-1}\int_{\infty}^{\tau} G_0^2(\tau', 0)d\tau'$, Z^{-1} is the function inverse to Z, and $\theta_0 = \theta(\tau, z = 0)$.

The function $\theta(\tau, z)$ allows us to find

$$\begin{aligned} G_p &= G_0(\tau)\sin[\theta(\tau, z)], \\ G_c &= G_0(\tau)\cos[\theta(\tau, z)]. \end{aligned} \qquad (9)$$

Analysis of Eqs. (9) [with allowance for (8)] shows that the evolution of the probe pulse depends on the time shape of the coupling pulse at the boundary $z = 0$ of the medium. Figure 2 displays the evolution [described by solution (9)] of the Rabi frequency for the probe and coupling pulses as a function of the z coordinate. The shape of the pulses at the boundary $z = 0$ of the medium is shown in Fig. 2a. As is seen, a time compression of the probe pulse occurs under the conditions indicated. The probe-pulse duration significantly decreases at the output of the medium compared to the input duration. From a physical standpoint, this behavior is associated with the fact that under the indicated conditions in the medium, the propagation velocity of the probe-pulse trailing edge is higher than that of the leading edge. The constraints for the compression are

stipulated by the finite width of the transparency window in which the probe pulse can propagate without absorption and also by the adiabaticity conditions.

The pattern of the space–time pulse evolution is similar to the propagation of adiabatons [8]. However, in our case, the pulse duration and the pulse shape vary with pulse propagation, the envelopes of both pulses changing consistently. Therefore, they may be called quasi-adiabatons. Thus, we can speak on the coherent control of the probe-pulse shape by the coupling pulse under the EIT conditions.

It is worth noting that the compression effect does not depend on details of the coupling-pulse time structure. It is sufficient to have a region in which the pulse amplitude (adiabatically) increases. The narrowing effect also arises in the case of a linear variation law for the coupling-pulse envelope. If the coupling-pulse amplitude becomes constant (with respect to time), then, as in [8], we have adiabatons at the output of the medium.

The results obtained are highly consistent with data obtained by the numerical solution of the self-consistent set of Maxwell–Schrödinger equations (1), (2) for the region of parameter in which the adiabaticity condition is fulfilled.

The compression of the probe pulse, which was demonstrated above, is a specific case in which coherent control of the probe pulse shape was achieved by means of EIT. Choosing the time shape of a coupling pulse, it is possible, e.g., to broaden the probe pulse and to form its flat-top or two-bump shape, etc.

3. Thus, it has been theoretically demonstrated that it is possible to control the envelope and duration of a probe pulse on the basis of the EIT phenomenon. This method is applicable to the control of pulses in a wide

duration region and in a broad range of spectral wavelength.

The method proposed for the coherent control of laser-pulse time shape can be useful in optical-communication technologies, in processing optical signals, and in nonlinear optics.

ACKNOWLEDGMENTS

REFERENCES

1. S. G. Rautian, G. I. Smirnov, and A. M. Shalagin, in *Nonlinear Resonances in Spectra of Atoms and Molecules* (Nauka, Novosibisrk, 1979), p. 310 [in Russian].

2. A. K. Popov, *Introduction to Nonlinear Spectroscopy* (Nauka, Novosibirsk, 1983) [in Russian].

3. S. E. Harris, Phys. Today **50** (7), 36 (1997).

4. M. D. Lukin, P. H. Hemmer, and M. O. Scully, Adv. At., Mol., Opt. Phys. **42**, 347 (2000).

5. A. B. Matsko, O. Kocharovskaya, Yu. Rostovtsev, *et al.*, Adv. At., Mol., Opt. Phys. **46**, 191 (2001).

6. M. D. Lukin, Rev. Mod. Phys. **75**, 457 (2003).

7. E. Kuznetsova, O. Kocharovskaya, P. Hemmer, *et al.*, Phys. Rev. A **66**, 063802 (2002).

8. R. Grobe, F. T. Hioe, and J. Eberly, Phys. Rev. Lett. **73**, 3183 (1994).

9. V. G. Arkhipkin and I. V. Timofeev, Phys. Rev. A **64**, 053811 (2001).

10. V. G. Arkhipkin and I. V. Timofeev, Pis'ma Zh. Éksp. Teor. Fiz. **76**, 74 (2002).

11. A. V. Sokolov and S. E. Harris, J. Opt. B: Quantum Semiclass. Opt. **5**, R1 (2003).

12. H. Kawashima, M. M. Wefers, and K. A. Nelson, Annu. Rev. Phys. Chem. **46**, 627 (1995).

13. N. V. Vitanov, M. Fleischhauer, B. W. Shore, *et al.*, Adv. At., Mol., Opt. Phys. **46**, 55 (2001).

14. E. Arimondo, Progress Opt. **35**, 257 (1996).

Translated by G. Merzon

====== **PHYSICS** ======

Stochastic Simulation of the Fluctuation Stage in the Formation of Thin Films

A. L. Bondareva* and G. I. Zmievskaya**

Presented by Academician Yu.A. Ryzhov September 22, 2004

The creation of coatings with given properties, which are important in the areas of microelectronics and the nanomodification of surfaces, depends on the initial distribution of the adsorbing layer of particles deposited on the surface. The nucleation of thin-film islands is simulated in a numerical stochastic experiment. Adsorbed-material islands assume the properties of coating due to a heterogeneous phase transition at the fluctuation stage that lasts no longer than 10^{-4} s; this phase transition is a strongly nonequilibrium process of the formation of clusters of new-phase nuclei. The rate of this process, as well as the homogeneity of the coating that arises, is governed by the temperature of the substrate and the plasma (or gas) flux fluence on the surface, as well as by certain crystal-lattice properties, such as its degree of anisotropy and elastic properties, the density of defects responsible for porosity, the presence of dislocations, and the potential of the interface between the solid substrate and plasma.

The formation of coating islands on the surface should be simulated as a plasma-like medium, taking into account the fluctuation and correlation properties of the phase transition. Computer experiments, which often cannot be carried out in laboratory, make it possible to obtain a complete qualitative pattern of the processes under consideration, to study nonlinear processes over a wide region of physical parameters, where approximation analytical theories are inapplicable, and to clarify the limits of applicability and efficiency of approximate theoretical approaches [1].

Kinetic equations describing a nonequilibrium stage in the formation of nuclei [2] upon homogeneous condensation are known in theoretical physics [3] and mechanics [4]. A numerical model based on Ito–Stratonovich stochastic differential equations with nonlinear functional coefficients [5] has been developed in order to study fluctuation instability of the phase transition in water vapors [6]; this model was applied both to calculate the formation kinetics for charged liquid droplets of a dusty-plasma metal near an electrode [7] and to simulate the nucleation of vacancy-gas defects (blisters) in the crystal lattice of the metal [8]. New algorithms and methods for solving stochastic differential equations with constant coefficients [9] were modified in [5–8, 10] to solve problems involving stochastic differential equations with functional coefficients. The formation of defect layers perpendicular to the ion flux in a lattice, retardation of the formation of defects upon the appearance of gas pores in the lattice, etc., which were discovered in the laboratory experiment, have been corroborated in computer experiments [8, 10] in which the nonequilibrium distributions of blisters over their size and position in the crystal lattice [8] were calculated and stresses in the crystal lattice and flicker-noise spectra were analyzed. The nonlinear dependence of the mean size of a blister on lattice temperature was found [10]. The process of the nonequilibrium formation of thin film islands on the surface can be simulated using a stochastic model of the heterogeneous formation of clusters of coating-material nuclei (islands) and their Brownian motion on the surface. Ion stimulation involved in the formation of thin films [11] on the surface was analyzed in the framework of equilibrium models with the object of estimating film-growth rate. Using stochastic simulation, we analyze nonequilibrium processes in the formation of thin-film nuclei on the surface and study the role of linear dislocation on the surface, starting with Leontovich equations [13].

KINETIC AND STOCHASTIC EQUATIONS OF THE MODEL

Nucleation of the islands of material deposited on the surface is simulated by a superposition of two Wiener random processes: the fluctuation-induced formation of island nuclei at surface points (x, y) and the Brownian motion of islands (whose sizes are determined at the preceding step) over the surface. The initial state of the model is specified by the coordinates of adatoms randomly located on the plane according to the temperature, lattice geometry, and the binding energy

Keldysh Institute of Applied Mathematics,
Russian Academy of Sciences, Miusskaya pl. 4,
Moscow, 125047 Russia
* e-mail: bal@spp.keldysh.ru, bal@infopro.msk.ru
** e-mail: zmi@keldysh.ru

of an adatom with the lattice. The plasma flux with vapor particles and metal droplets is assumed to be unchanged upon calculation, which provides for the openness of the simulated system. The set of collisions between vapor particles and an island on the surface (which collisions attach particles to the island, evaporate and displace them over the surface, etc., without affecting chemical transformations) forms a stochastic process $\{g(t), t > 0\}$ in the phase space **G** of the island sizes. The energy of the nucleus formation (Gibbs potential) can be represented by a nonlinear model, where, in addition to the previously included factors [5–8], the following two factors are taken into account: possible breakage of the elastic bonds of the lattice upon contact between the cluster and the surface, and decrease in the potential on the dislocation line specified by the equation $y = x$. Thus, at the step Δt_1, solving the Ito stochastic differential equation, from the trajectories of the random process $g(t)$, we discover the evolution of the diffusion random process, which determines the size of the new-phase islands. At the step Δt_2, we simulate stochastic processes $x(t)$ and $y(t)$, which specify the position of Brownian particles (new-phase islands of the coating material). The hopping displacements of adatoms and clusters formed from them are simulated by random Wiener processes realized at the step Δt_2. The motion of the Brownian particles is induced by the long-range potentials of their interaction (through acoustic phonons of the lattice and taking into account the Friedel oscillations of the lattice-electron density [12]), the model nonlinear potential of the lattice surface, and the potential on the dislocation line. At the boundaries of the calculation region, which includes 400×400 lattice parameters, the motion of islands is simulated using the periodic boundary conditions, disjointness condition for islands, and the criterion of joining islands on the plane, which slightly differs from the inelastic-collision condition that stepwise changes the size of a nucleus. Moreover, the formation of a monolayer is considered.

The evolution of the coating area is described by the kinetic distribution functions $f(g, x, y, t)$ of islands over their areas g and the positions of the centers of masses of islands on the surface of the given type of crystal lattice:. These distribution functions are the transition probability densities of the random process that is described above and realized in the computer experiment. The discrete stochastic model [5] attributes the enumerable measures from the computer experiment to the probable average quantities of the kinetic distribution functions. The Kolmogorov–Feller [2, 5, 6] and Einstein–Smoluchowski [8, 10] equations, which describe the island-formation model, include nonequilibrium distribution functions $f(g, x, y, t)$. A comparison of the characteristic times Δt_1 and Δt_2 makes it possible to solve the problem on the basis of the splitting that occurs in physical processes. Note that the kinetic equations are written using Fokker–Planck linear operators

and nonlinear coefficients depending on distribution functions, i.e., functional coefficients, and that the equations that must be solved are quasi-linear. They are solved using systems of Ito stochastic differential equations, which are statistically equivalent to the kinetic problem. Theorems of existence and uniqueness have been proved for these equations, and effective numerical methods, which are used in the stochastic-simulation method, were developed to solve these equations [9]. The kinetic equations of the model have the form

$$\frac{\partial f_r(g, t)}{\partial t} = \frac{\partial \left[D_g(g, t) \dfrac{\partial f_r(g, t)}{\partial g} \right]}{\partial g}$$

$$+ \frac{1}{kT} \frac{\partial \left[D_g(g, t) f_r(g, t) \dfrac{\partial \{\Delta \Phi(g, \mathbf{r}, t)\}}{\partial g} \right]}{\partial g} + S_\alpha(f_\alpha),$$

$$f_r(g, 0) = f_{0g}, \quad \left. \frac{df_r(g, t)}{dg} \right|_{g \leq 2} = 0,$$

$$f_r(g, t)|_{g < 2} = 0,$$

$$\frac{\partial f_g(\mathbf{r}, t)}{\partial t} = \frac{\partial \left[D_r(\mathbf{r}, t) \dfrac{\partial f_g(\mathbf{r}, t)}{\partial r} \right]}{\partial \mathbf{r}} - \frac{\partial \left[\dfrac{\mathbf{F}(\mathbf{r}, t)}{M_g \gamma} f_g(\mathbf{r}, t) \right]}{\partial \mathbf{r}},$$

$$f_g(\mathbf{r}, t)|_{t = 0} = f_{0r},$$

$$f_g(\mathbf{r}, t)|_{x = x_{\text{left}}} = f_g(\mathbf{r}, t)|_{x = x_{\text{right}}},$$

$$f_g(\mathbf{r}, t)|_{y = y_{\text{left}}} = f_g(\mathbf{r}, t)|_{y = y_{\text{right}}}.$$

Here, $S_\alpha(f_\alpha)$ is the vapor-source function, the vapor distribution function f_α is given as a Maxwellian distribution function at 2500 K, $f_r(g, t)$ is the size distribution function of islands, g is the number of atoms in a cluster, $D_g(g, t)$ is the diffusion coefficient in the size space, $\Delta \Phi(g, \mathbf{r}, t)$ is the thermodynamic potential of the formation of an island, M_g is its mass, $f_g(\mathbf{r}, t)$ is the distribution function of islands over the surface, $\mathbf{r}$ is the radius-vector of the cluster in the orthogonal coordinate system, $x_{\text{left}} = y_{\text{left}} = -200$, $x_{\text{right}} = y_{\text{right}} = 200$ (hereafter, all spatial coordinates are given in the lattice constant), and

$$F_x = -\frac{\partial U(x, y, z)}{\partial x},$$

where $U(x, y, z)$ is the potential of interaction between islands through the lattice phonons and Friedel oscillations of the electron density. The form of the interaction potential is similar to the potentials used in [8, 10, 12, 14].

We present the stochastic analogue of the kinetic equation for changing the cluster size:

$$\frac{dg}{dt} = -\frac{1}{kT}D_g(g,t)\frac{\partial\Delta\Phi(g,\mathbf{r},t)}{\partial g} - \frac{1}{2}\frac{\partial D_g(g,t)}{\partial g}$$
$$+ \sqrt{2D_g(g,t)}dW,$$

$$t_0 \le t \le T_k, \quad g(t_0) = g_0 \in [g_{\min}, g_{\max}], \quad g(t) > 2;$$

T_k is the duration of the fluctuation stage under consideration, g_0 is the initial size of the island, and dW is the increment of the Wiener random process. The correctness of the solution of the stochastic differential equation and the adequacy of the representation of the Wiener random process for the case in which the Stratonovich form is used for the stochastic differential equation was analyzed in detail in [5, 9]. The region of the instability of nucleus formation $\sim kT$ [6] is taken to specify the initial conditions. This corresponds to the island-size interval $[g_{\min}, g_{\max}]$, which are determined from the conditions

$$\left.\frac{\partial\Delta\Phi}{\partial g}\right|_{g_{cr}} = 0,$$

where g_{cr} is the critical size of the island,

$$|\Delta\Phi(g_{cr}) - \Delta\Phi(g_{\min})| = |\Delta\Phi(g_{cr}) - \Delta\Phi(g_{\max})| = kT;$$

and $D_g(g,t)$ and $\Delta\Phi(g,\mathbf{r},t)$ are functional coefficients of the form

$$\Delta\Phi(g,\mathbf{r},t)$$
$$= \begin{cases} -(a_\Phi - c)g + bg^{2/3} + \Delta\Phi_r, & \Delta\Phi(g,\mathbf{r},t) < \Delta_{break}; \\ -(a_\Phi - c)g + bg^{2/3} + \Delta\Phi_r - \Delta\Phi_{break}, \\ \Delta\Phi(g,\mathbf{r},t) > \Delta_{break}. \end{cases}$$
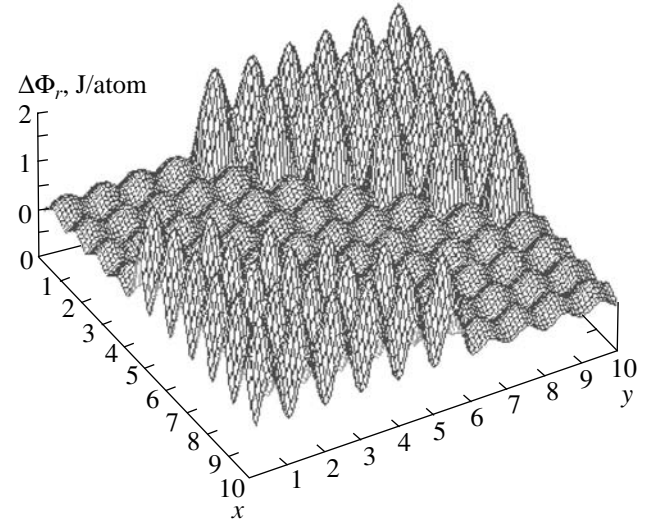
Here,

$$a_\Phi = \frac{\pi(2 - 3\cos\theta + \cos^3\theta)}{3V_{adat}}(\chi_\beta - \chi_\alpha),$$

where $\chi_\beta - \chi_\alpha$ is the difference between the chemical potentials of the phases; V_{adat} is the adatom volume; θ is the wetting angle between S and β phases; α phase is Ni vapors; β phase is a Ni liquid cluster on the tungsten S-phase surface (bcc lattice);

$$b = 2\pi(1 - \cos\theta)\sigma_{\alpha\beta}\left(1 - \frac{1}{3}\bar{g}^{-1/3}\right)$$
$$+ \pi\sin^2\theta(\sigma_{\beta S} - \sigma_{\alpha S}),$$

where $\sigma_{\alpha\beta}$, $\sigma_{\beta S}$, and $\sigma_{\alpha S}$ are the surface tensions at the cluster–vapor, cluster–solid, solid–vapor interfaces,

Fig. 1. Behavior of $\Delta\Phi_r$ near the dislocation. The coordinates x and y are given in the lattice parameters.

respectively; the correction $1 - \frac{1}{3}\bar{g}^{-1/3}$ arises because the cluster–vapor surface is not planar; c is the elastic reaction of the lattice to nucleus formation; Δ_{break} is the energy of one bond breaking on the surface; $\Delta\Phi_{break}$ is the energy necessary for a single bond to break on the surface, under the assumption that the development of the cluster is accompanied by breakage of several surface bonds; and $\Delta\Phi_r$ represents the substrate effect (Fig. 1). The last effect decreases with increases in the cluster size. If the cluster is located at the point (x, y), then

$$\Delta\Phi_r = \Psi(g,\mathbf{r})\left(2 - \cos\frac{2\pi x}{a_x} - \cos\frac{2\pi y}{a_y}\right),$$

where

$$\Psi \sim \frac{1}{\sqrt{g}}$$

is the functional coefficient of the potential, which takes into account the modification of the surface, and $a_x = a_y = a$ is the lattice constant. Near a dislocation, Ψ decreases by several times, which simulates the dislocation effect on the thermodynamic potential of the formation of a new-phase island. The diffusion coefficient in the cluster-size space is written in the form
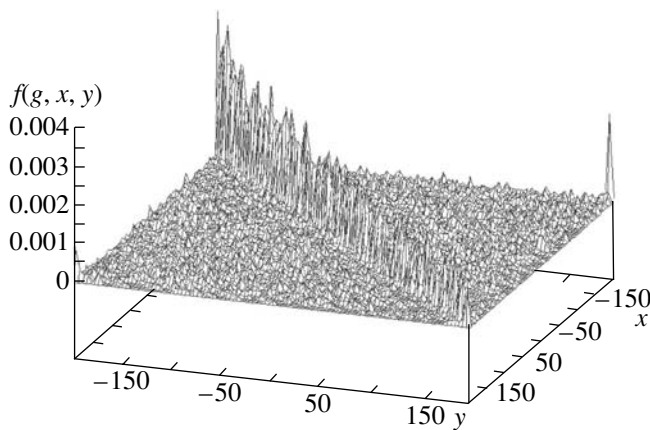
$$D_g(g,t) = D_{g0}g^{2/3}.$$

Taking into account the small sizes of the cluster during the fluctuation stage, we write the diffusion coefficient for the new-phase island over the surface in the form

$$D_x = \frac{D_{x0}}{\gamma M_g}(1 + \beta\Delta x^2).$$
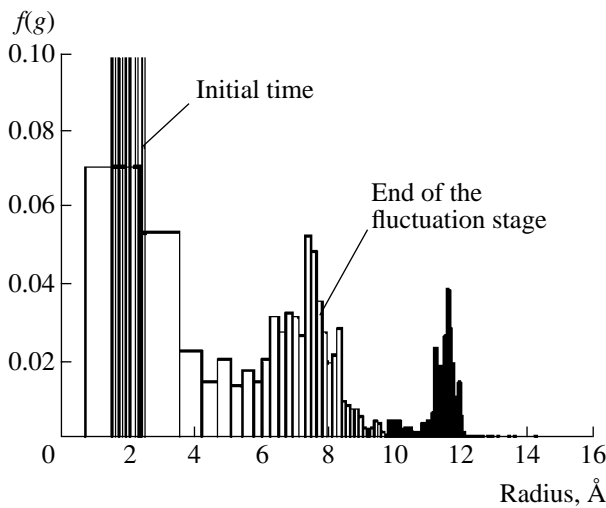
Fig. 2. Distribution function of islands over the radius. The distribution function is normalized to unity.

Fig. 3. Distribution function of islands over the surface in the presence of the linear dislocation at 10^{-4} s. The coordinates x and y are given in the tungsten lattice parameters. The distribution function is normalized to unity.

Here, D_{xy0} is the coefficient of the diffusion of the adatom over the surface, γ is the friction coefficient, and $0 \leq \beta \leq 1$. The characteristic growth time is given by the expression

$$\tau_g = \frac{a}{\alpha \pi r_{adat}^2 \bar{v} c_{adat}} \sim 10^{-8} \text{ s},$$

where α is the coefficient of the adhesion of the adatom to the cluster, r_{adat} is the adatom radius, $\bar{v}$ is the average velocity of the adatom motion over the substrate surface, c_{adat} is the number of adatoms per unit surface, and

$$\tau_{xy} = \frac{a^2}{D_{xy0}} \sim 10^{-7} \text{ s}.$$

RESULTS AND CONCLUSIONS

To solve the system of Ito–Stratonovich stochastic differential equations, we apply the stable numerical method of second-order accuracy [9], which makes it possible to analyze the mathematical expectation of the island size and its standard deviation. The numerical method of the stochastic analogue [5–8, 10] as applied to the study of the fluctuation stage of the phase transition on the surface expands these opportunities [9]: nonequilibrium distribution functions of islands over sizes and positions on the surface can be analyzed. The flicker-noise spectra of the system under simulation that change upon the appearance of a thin film on the lattice surface and stresses in it are calculated with the inclusion of distribution functions by the method described in [8, 10]. Liquid-nickel island nuclei are considered at 2500 K on the tungsten surface. The calculation involves 10^5 trajectories. The initial number of Brownian particle islands is equal to 10. They are uniformly distributed over a surface size of 1.96×10^{-10} cm^2, and the initial radius is 1.5 to 2.8 Å (in the instability region of the nucleus formation). The number of lattice sites is equal to 1.6×10^5, the single-element area is equal to 12.25 Å^2, and the (001) plane is considered.

Figure 2 shows histograms of distribution functions (averaged over the coordinates of the area used in the calculation) as functions of the island radius at $t = 0$ and at the end of the calculation. The initial sizes are taken in the range 1.5–2.8 Å. After 10^{-4} s, the form of the distribution function indicates that there are three most probable sizes of islands. The first size (~2 Å) is close to the critical size of the nucleus at 2500 K for a constant nickel-vapor flow on the surface. A radius of about 8 Å corresponds to most growing islands. Relatively large islands (~12 Å) are presented in the distribution due to the adjoining of small nuclei to larger nuclei upon motion.

Figure 3 shows the distribution function $f(g, x, y)$ at the end of the fluctuation stage on the surface in the presence of the linear dislocation. The number of islands near the dislocation differs by nearly an order of magnitude (by a factor of 8) from that on the entire surface involved in the calculation.

Figure 4 illustrates change in the coating area $S(t)$ with respect to the initial area $S(t = 0)$. The nucleus formation rate at the fluctuation stage of the phase transition possibly presents the effect of processes that are taken into account in the model. For a calculation time of 10^{-4} s, islands are formed with an area of $2.5 \times 10^{-3} S(t = 0)$, which is 70 times larger than the initial coating.

Thus, nonequilibrium distribution functions of islands over sizes and localization on the surface (Fig. 2) that are obtained numerically differ from log-normal distributions and present possible mechanisms of the formation of islands on the crystal lattice under
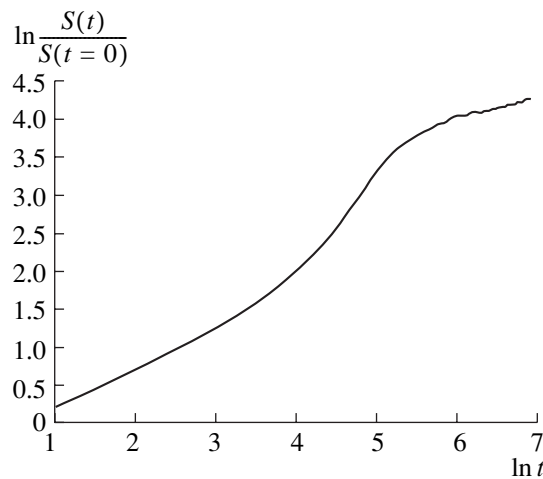
Fig. 4. Ratio of the coating-area logarithm at the time under consideration to the initial coating area vs. the time logarithm. Time is measured in the algorithm step ($\tau = \tau_{xy} \sim 10^{-7}$ s).

given model conditions (temperature, vapor density, interaction parameters, etc.). Three stages of the formation of coating during 10^{-4} s (Fig. 4) are revealed: from 0 to 10^{-5} s, from 10^{-5} to 2.5×10^{-5} s, and from 2.5×10^{-5} to 10^{-4} s. Consolidation of islands on the linear dislocation is observed (Fig. 2). The calculations show that stresses in the lattice under islands do not exceed values characteristic of the formation of vacancy-gas defects in the lattice upon blistering [10].

ACKNOWLEDGMENTS

REFERENCES

1. Yu. S. Sigov, *Computer Experiment: A Bridge Between the Past and Future of Plasma Physics* (Fizmatlit, Moscow, 2001) [in Russian].
2. Ya. B. Zel'dovich, Zh. Éksp. Teor. Fiz. **12**, 525 (1942).
3. E. M. Lifshitz and L. P. Pitaevskiĭ, *Course of Theoretical Physics*, Vol. 10: *Physical Kinetics* (Nauka, Moscow, 1979; Pergamon, Oxford, 1981).
4. V. N. Gorbunov, U. G. Pirumov, and Yu. A. Ryzhov, *Non-equilibrium Condensation in High-Speed Gas Flows* (Mashinostroenie, Moscow, 1984; Gordon and Breach, New York, 1989).
5. G. I. Zmievskaya, Fiz. Plazmy **23** (4), 45 (1997).
6. G. I. Zmievskaya and T. V. Zin'kovskaya, Dokl. Akad. Nauk SSSR **309** (2), 301 (1989) [Sov. Phys. Dokl. **34**, 951 (1989)].
7. G. I. Zmievskaya, T. V. Levchenko, and T. K. Soboleva, Teplofiz. Aéromekh. **9** (4), 241 (2002).
8. A. L. Bondareva and G. I. Zmievskaya, in *Mathematical Models of Nonlinear Excitations, Transfer, Dynamics, and Control in Condensed Systems and Other Media*, Ed. by L. Uvarova (Plenum, New York, 1998), pp. 241–250.
9. S. S. Artemiev and T. A. Averina, *Numerical Analysis of Systems of Ordinary and Stochastic Differential Equations* (VSP, Utrecht, 1997), p. 176.
10. A. L. Bondareva and G. I. Zmievskaya, Izv. Akad. Nauk, Ser. Fiz. **68**, 336 (2004).
11. M. B. Guseva, Soros. Obraz. Zh., No. 10, 106 (1998).
12. A. A. Berzin, A. I. Morozov, and A. S. Sigov, Fiz. Tverd. Tela **38** (5), 1349 (1996).
13. M. A. Leontovich, Zh. Éksp. Teor. Fiz. **3** (3/4), 18 (1935).
14. A. L. Bondareva and G. I. Zmievskaya, Izv. Akad. Nauk, Ser. Fiz. **66**, 994 (2002).

Translated by R. Tyapaev

PHYSICS

Effect of Relaxation-Time Distribution in the Dielectric Spectra of Semielectrics

N. V. Afanas'ev[1], L. V. Mukhaeva[1], A. A. Maksimov[1,2], T. G. Ermakova[2], and Academician M. G. Voronkov[2]

To develop a method for investigating materials of molecular electronics [1] it is necessary to specify the distinctive attributes of relaxation polarization that are associated with the local electrical conduction of macromolecules of the polymeric semiconductor, semielectrics [2]. To interpret the dependence of permittivity ε' and loss factor ε'' on frequency ν for polyacene quinones, we used the model of grain–interlayers [3]. We generalized this model in view of the wide conductivity distribution of macromolecules.

Previously [4], we found a peak ε''_{max} of loss factor at $\nu = \nu_{max}$ in the spectra of both a mixture of polyacene quinone powder, with paraffin insulating the grains, and pressed samples. This peak was quantitatively attributed to the interlayer polarization of presumably spherical three-dimensional conducting molecular domains [5]. However, the hypothesis proposed in [4] is insufficiently justified because the contribution of the competing mechanism of the interlayer polarization of grains [6] is not estimated, and the attributes distinguishing it from the polarization of macromolecules are not specified. In this work, we report on the principal possibility of observing separately the spectra corresponding to both mechanisms of polarization.

We investigate polyacene quinone prepared by the cyclopolycondensation [7] of pyromellitic dianhydride with pyrene in melt in the presence of zinc chloride. The polycondensation duration varied within the limits of 24 h to 5 min during the synthesis of linear semielectrics composed of conducting molecular chains (used as materials of molecular electronics), which was achieved by excluding the possibility of three-dimensional polycondensation at a reasonably early stage prior to the development of the chain-sewing process. The technique for preparing samples and dielectric measurements was previously described in [8]. Based

on results of experimental investigations, we chose a polymer prepared at a reaction duration of 10 h. The dc conductivity of this polymer is equal to $\sigma_0 = 1.5 \times 10^{-3}$ S/m.

Figures 1 and 2 show the circle diagram and the dispersion curves ε_1 and ε_2 [13] for the pressed sample. They indicate that the only dispersion region is observed within the investigated frequency range. The dependence of complex permittivity ε on angular frequency ω in this region is described by the generalized Debye equation [9]

$$\varepsilon(\omega) = \varepsilon'(\omega) - j\varepsilon''(\omega) = \varepsilon'_\infty + \frac{\Delta\varepsilon'}{1 + (j\omega\tau_{mp})^\alpha}. \quad (1)$$

Here, ε'_∞ and $\Delta\varepsilon'$ are, respectively, the high-frequency limit and increment of ε' in the dispersion region, τ_{mp} is the most probable value of relaxation time τ in the statistical distribution, and $0 \le \alpha \le 1$ is the parameter of this distribution. The α value close to 0.6 (Fig. 1), which is typical for the dispersion region within the rf range in spectra of polyacene quinones [8], can be explained by the wide conductivity distribution of macromolecules [10]. We assumed that such a distribution is a distinctive attribute of the interlayer polarization of three-dimensional conducting macromolecules. To test this assumption, a thought experiment was performed with the proposed model.

As is known, for the model [3] that is usually used in the dielectric spectroscopy of pressed samples of high-ohmic semiconductors, a small thickness h of insulating layers (air gaps) between grains is characteristic; i.e., the volume concentration v of the conducting phase is close to unity. As a result, the corresponding dispersion region is characterized by high values of $\Delta\varepsilon'$ and τ. At high frequencies ($\nu \gg \nu_{max}$), conductivity σ is independent of frequency, which corresponds to a unique relaxation time. Therefore, the dielectric spectrum is described by Eq. (1) for $\alpha = 1$.

As applied to semielectrics with a sufficiently large size of the grain that is composed of many macromolecules of various conductivities, it can be assumed that

---

[1] *Irkutsk State Technical University,*
  ul. Lermontova 83, Irkutsk, 664074 Russia

[2] *Favorskiĭ Institute of Chemistry, Siberian Division,*
  Russian Academy of Sciences,
  ul. Favorskogo 1, Irkutsk, 664033 Russia
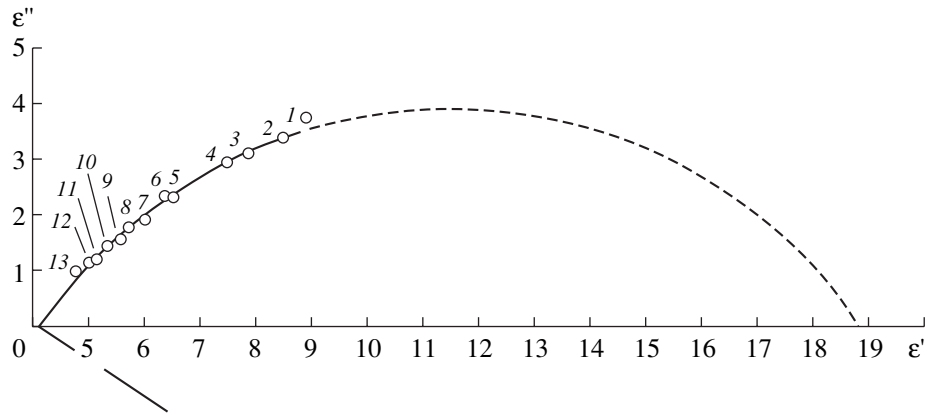
Fig. 1. Circle diagram for a pressed polyacene quinone sample for frequencies (*1*) l.6, (*2*) 2, (*3*) 2.5, (*4*) 3.16, (*5*) 4, (*6*) 5, (*7*) 6.3, (*8*) 8, (*9*) 10, (*10*) 12.6, (*11*) 16, (*12*) 20, and (*13*) 25 MHz. The parameter of the time-relaxation distribution is $\alpha = 0.62$; the thickness of the sample is 110 μm; the grain size is about 2 μm; steel electrodes are 2.5 mm in diameter; and temperature is 294 K.

all grains have the same conductivity σ_0. Assuming for the sake of simplicity that grains have the same size, as well as cubic shape and close face-to-face packing, one can describe the dielectric spectrum of such a structural model for $v \longrightarrow 1$ ($h \longrightarrow 0$) by the equation

$$\varepsilon(z) = \varepsilon'_{\infty} + \frac{\Delta\varepsilon'_1}{1 + jz_1} + \frac{\Delta\varepsilon'_2}{1 + (jz_2)^{\alpha}} - f(z_1)\frac{\Delta\varepsilon'_2}{1 + (jz_2)^{\alpha}}. \quad (2)$$

Here, $z = \dfrac{v}{v_{max}}$, $0 \leq f \leq 1$ is the factor of the action of the first dispersion region on the much smaller second region located in the higher frequency range ($v_{max2} \gg v_{max1}$).

The first region corresponds to the interlayer polarization of grains. As follows from Eq. (2), it is characterized by a unique relaxation time ($\alpha_1 = 1$). It is easy to explain this fact assuming for simplicity that the conductivity of layers is equal to zero. In this case, the condition of equilibrium of charges in a grain is the compensation of the applied electric field in its bulk. As a result, the contribution of the interlayer polarization of conducting macromolecules in the permittivity ε of the model is also equal to zero. In order to take this phenomenon into account in a frequency range of the order of v_{max1} and lower, it is necessary to set $f = 1$ in Eq. (2). For this reason, it is necessary to accept that the absence of relaxation-time distribution is an attribute of the interlayer polarization of grains of semielectrics.

For higher frequencies ($v \gg v_{max1}$), the conductivity σ_0 of grains is insufficiently high to compensate the external electric field in their bulk for a half-cycle of its variation, and the interlayer polarization of macromolecules appears. In this case, the action factor in Eq. (2) decreases with frequency, which leads to an increase in the contribution of macromolecules to the permittivity ε
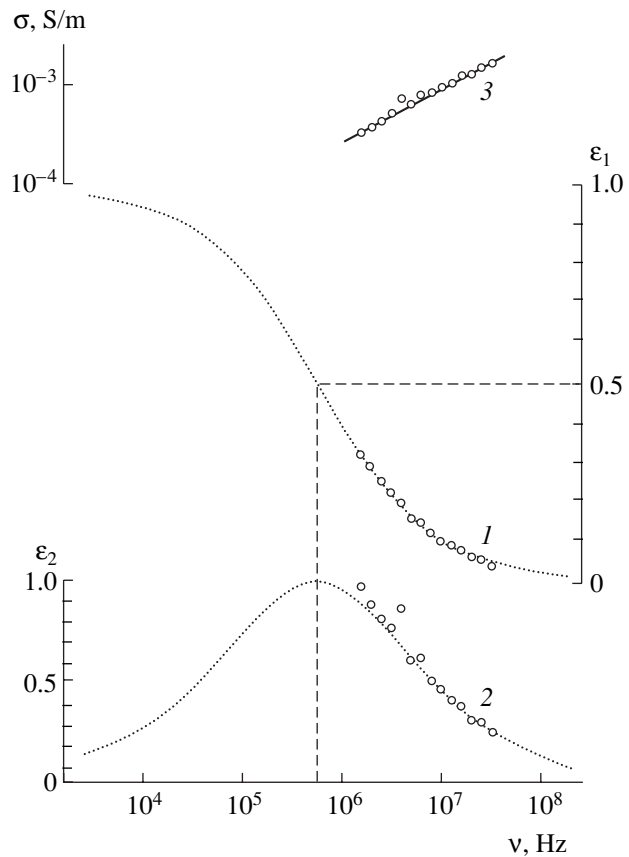
Fig. 2. Dispersion curves plotted for polyacene quinone using the data in Fig. 1. Hereafter, $\varepsilon_1 = \dfrac{\varepsilon' - \varepsilon'_{\infty}}{\Delta\varepsilon'}$ and $\varepsilon_2 = \dfrac{\varepsilon''}{\varepsilon''_{max}}$. Theoretical curves *1* and *2* for ε_1 and ε_2, respectively, are obtained with $\alpha = 0.6$. Experimental values for ε_1 are obtained with $\Delta\varepsilon' = 14.65$ and $\varepsilon'_{\infty} = 4.15$, and for ε_2, with $\varepsilon''_{max} = 3.88$. Curve *3* is the conductivity σ (without the contribution of σ_0).
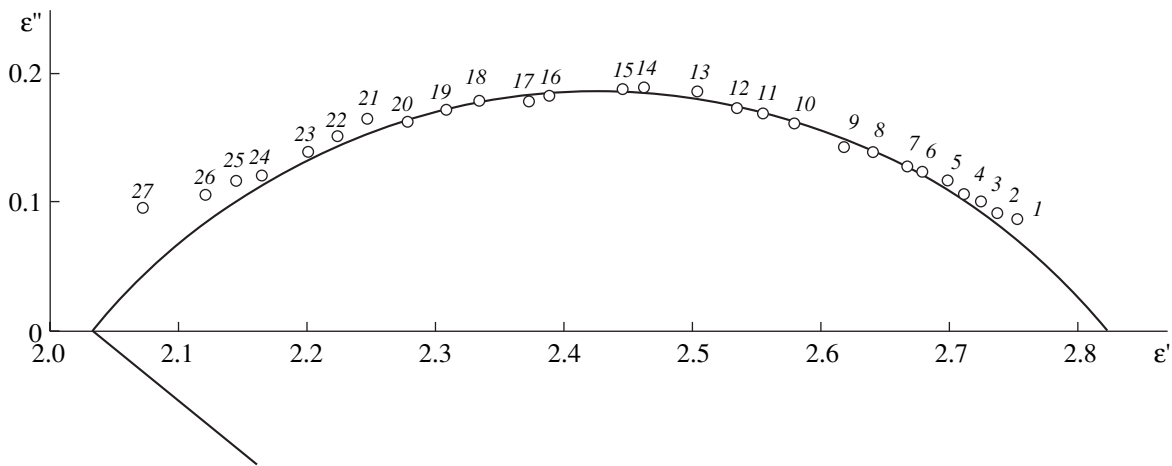
Fig. 3. Circle diagram for the mixture of polyacene quinone powder with paraffin for frequencies (*1*) 50.2, (*2*) 63.1, (*3*) 100, (*4*) 126, (*5*) 160, (*6*) 199, (*7*) 251, (*8*) 316, (*9*) 398, (*10*) 502, (*11*) 631, (*12*) 795 kHz, (*13*) 1, (*14*) 1.26, (*15*) 1.6, (*16*) 2, (*17*) 2.5, (*18*) 3.16, (*19*) 4, (*20*) 5, (*21*) 6.3, (*22*) 8, (*23*) 10, (*24*) 12.6, (*25*) 16, (*26*) 20, and (*27*) 25 MHz. The parameter of the time-relaxation distribution is $\alpha = 0.56$; the volume concentration of the polymer in the mixture is $v' = 0.1$; and temperature is 294 K.

of the model. However, the unperturbed part of the second dispersion region is observed only in the range of sufficiently high frequencies with $f = 0$. Since $\Delta\varepsilon_2' \ll \Delta\varepsilon_1$, the interlayer polarization of macromolecules is detected by the distortion of the circle diagram for the first dispersion region near its high-frequency boundary. The parameters of the second region may be determined by the method of circle diagrams. However, the possibility of their overlapping in the range of frequencies with $f > 0$ should in this case be taken into account. From the value of $\Delta\varepsilon_2'$, we calculate the volume concentration V of conducting macromolecules in a grain.

For $v > v_{max2}$, the conductivity of the model begins to rapidly increase with frequency owing to an increase in the active component of electric current in lower-resistance macromolecules. In this case, rather than as a single relaxation oscillator, the grain should be considered as a set of relaxation oscillators, or conducting macromolecules, which is characterized by the corresponding α value. The polarization of grains disappears and the polarization of macromolecules appears.

The considered model is speculative because face-to-edge packing predominates in pressed samples of polyacene quinones; the latter is due to considerable friction between grains during pressing. Therefore, the condition $v \longrightarrow 1$ is violated even in the pressed sample. If v of the model decreases, both dispersion regions decrease and are displaced towards higher frequencies until only one region attributed to the interlayer polarization of conducting macromolecules remains in the spectrum (Fig. 2). However, it is already impossible to calculate V from the value of $\Delta\varepsilon'$.

The limiting case $v \longrightarrow 0$ corresponds to the mixture of grains with paraffin. The circle diagram and dispersion curves for this case are shown in Figs. 3 and 4.

As is seen, the α value is nearly the same as for the pressed sample.

The model of grain–interlayers is unsuitable for purposes of quantitative interpretation of the spectrum for the mixture (Fig. 4). For this reason, we used the generalized Lorenz–Lorentz model [11]. The most probable value of the conductivity of macromolecules $\sigma_{mp} = 7.7 \times 10^{-4}$ S/m is determined by the formula [4]

$$\sigma_{mp} = 2\pi\varepsilon_0 v'_{max}\left\{\left[\frac{1}{(1-v')N} - 1\right]\varepsilon_p' + \varepsilon_\infty'\right\}. \quad (3)$$

Here, v'_{max} and $v' = 0.1$ are the values of v_{max} and volume concentration v, respectively, of the conducting phase for the mixture with paraffin; $\varepsilon_0 = 8.85 \times 10^{-12}$ F/m; $0 \leq N \leq 1$ is the depolarization factor of conducting macromolecules, which is equal to 1/3 for the spherical shape; $\varepsilon_p' = 2$ is the permittivity of paraffin; and $\varepsilon_\infty' = 4$.

The conductivity distribution function of macromolecules is expressed by the formula [11]

$$f(x) = \frac{1}{h}\frac{dn}{dx} = \frac{1}{2\pi}\frac{\sin(1-\alpha)\pi}{\cosh(1-\alpha)x - \cos(1-\alpha)\pi}. \quad (4)$$

Here, $x = \ln\dfrac{\sigma}{\sigma_{mp}}$, n is the number of macromolecules, and dn is their number in the interval from x to $x + dx$.

Because the experiment confirming the model for $v \longrightarrow 1$ is a thought experiment, the requirement that grains of polyacene quinone have identical conductivity is not strict. However, the condition $\sigma(v) > \sigma_0$ must be met for $v \geq v_{max}$. This condition is provided by the
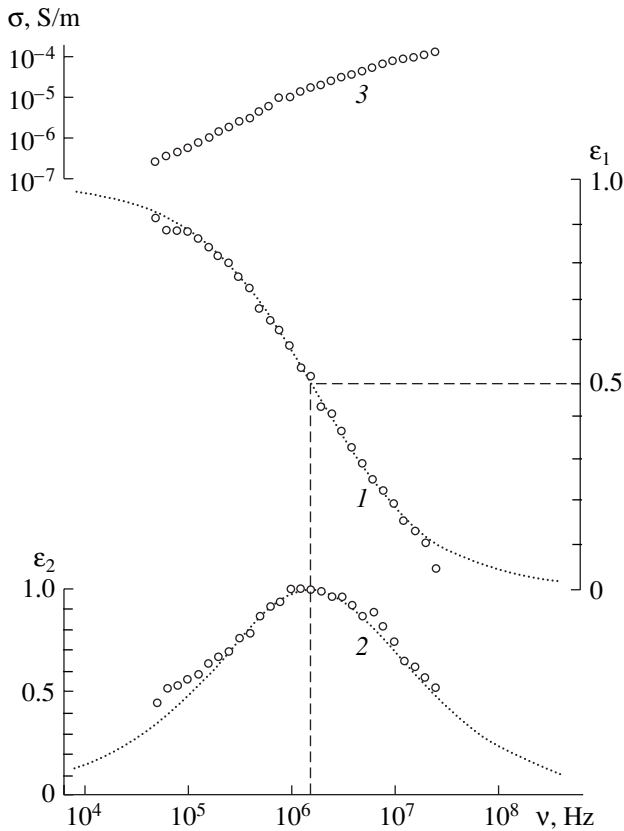
Fig. 4. Dispersion curves plotted for the mixture of poly-acene quinone powder with paraffin using the data in Fig. 3. Theoretical curves *1* and *2* for ε_1 and ε_2, respectively, are obtained with $\alpha = 0.6$. Experimental values for ε_1 are obtained with $\Delta\varepsilon' = 0.79$ and $\varepsilon'_\infty = 2.03$ and for ε_2, with $\varepsilon''_{max} = 0.19$. Curve *3* is the conductivity σ.

local nature of the conductivity of macromolecules in this case, i.e., by the fact that their insulation has the principal significance for semielectrics. Therefore, the investigation indicates that the observed relaxation-time distribution in spectra of polyacene quinones is a distinctive attribute of the new electron phenomenon

assumed in [12], and Eqs. (3) and (4) should now be considered to be proven in principle.

REFERENCES

1. V. I. Minkin, Zh. Org. Khim. **49** (6), 3 (2000).

2. N. V. Afanas'ev, L. V. Mukhaeva, M. G. Voronkov, and T. G. Ermakova, Dokl. Akad. Nauk **350** (1), 31 (1996) [Phys. Dokl. **41**, 381 (1996)].

3. C. G. Koops, Phys. Rev. **83** (1), 121 (1951).

4. N. V. Afanas'ev, L. V. Mukhaeva, M. G. Voronkov, and T. G. Ermakova, Dokl. Akad. Nauk **360** (5), 614 (1998) [Dokl. Phys. **43**, 330 (1998)].

5. N. V. Afanas'ev, L. V. Mukhaeva, L. Ya. Tsarik, *et al.*, Dokl. Akad. Nauk **367** (2), 179 (1999) [Dokl. Phys. **44**, 413 (1999)].

6. R. Rosen and H. A. Pohl, J. Polym. Sci. A1 **4**, 1135 (1966).

7. T. G. Ermakova, A. A. Maksimov, L. Ya. Tsarik, *et al.*, Vysokomol. Soedin. **44**, 551 (2002).

8. N. V. Afanas'ev, L. N. Omel'chenko, L. V. Mukhaeva, *et al.*, Dokl. Akad. Nauk SSSR **289** (3), 596 (1986) [Sov. Phys. Dokl. **31**, 572 (1986)].

9. H. Frolich, *Theory of Dielectrics: Dielectric Constant and Dielectric Loss*, 2nd ed. (Clarendon Press, Oxford, 1986; Inostrannaya Literatura, Moscow, 1960).

10. N. V. Afanas'ev, L. V. Mukhaeva, M. K. Voronkov, *et al.*, Dokl. Akad. Nauk SSSR **325** (1), 64 (1992) [Sov. Phys. Dokl. **37**, 356 (1992)].

11. A. V. Netushil, B. Ya. Zhukhovitskiĭ, V. N. Kudin, and E. P. Parini, *High-Frequency Heating of Dielectrics and Semiconductors* (Gostekhizdat, Moscow–Leningrad, 1959) [in Russian].

12. N. V. Afanas'ev, L. V. Mukhaeva, M. G. Voronkov, and T. G. Ermakova, Dokl. Akad. Nauk SSSR **323** (3), 452 (1992) [Sov. Phys. Dokl. **37**, 135 (1992)].

13. N. Afanas'ev, L. V. Mukhaeva, M. G. Voronkov, *et al.*, Dokl. Akad. Nauk SSSR **319** (4), 858 (1991) [Sov. Phys. Dokl. **36**, 508 (1991)].

Translated by V. Bukhanov

===== **PHYSICS** =====

Calculation of the Electromagnetic Fields of Dipole Sources in Layered Media

Corresponding Member of the RAS S. I. Smagin and V. N. Mazalov

Received September 27, 2004

Calculation of the electromagnetic fields of dipole sources in plane–parallel layered media is an important problem of mathematical physics. Moreover, it is impossible to apply integral equation methods to analyze fields in media with inclusions without a sufficiently accurate and efficient method for solving such problems [1–5]. Desired solutions are usually constructed by means of the integral transformation method. They are expressed in terms of Fourier–Bessel integrals of the solutions to boundary value problems for ordinary differential equations with the spectral parameter. Solutions to these equations are found by recurrence formulas [1, 2, 4].

To date, numerous works have been devoted to calculation of the aforementioned Fourier–Bessel integrals. The basic difficulties in the calculation of such integrals are associated with the necessity of numerical integration of rapidly oscillating functions. To overcome these difficulties, numerical filtration [6], asymptotic perturbation of the fundamental solution [7], change of integrals to series [8], etc., are used.

The method presented in this work is applicable to the calculation of electromagnetic fields in layered media whose parameters may vary over a wide range. It is based on the deformation of the integration contour of Fourier–Bessel integrals in the complex plane and has no restrictions associated with the integration of rapidly oscillating functions. This method is compared with other methods [6, 8].

FORMULATION OF THE PROBLEM

We consider the three-dimensional Euclidean space R^3, which is separated into $n - 1$ layers and in which the orthogonal coordinate system $oxyz$ is introduced. The planes $z = z_l$, $l = 1, 2, \ldots, n - 1$, $z_0 = \infty$, and $z_n = -\infty$ are the boundaries of these layers; and the conductivity, permittivity, and permeability are constant within each layer and are equal to σ_l, ε_l, and μ_l, respectively, where $l = 1, 2, \ldots, n - 1$. A point-like harmonic electric dipole

Computer Center, Far East Division,
Russian Academy of Sciences, Khabarovsk, Russia
e-mail: smagin@as.khb.ru, mazalov@as.khb.ru

is located at the point $M' = (x', y', z')$, where $z' = z_p$, $1 < p < n - 1$, $\sigma_p = \sigma_{p+1}$, $\varepsilon_p = \varepsilon_{p+1}$, $\mu_p = \mu_{p+1}$. In this case, the electric $\mathbf{E} = (E_x, E_y, E_z)$ and magnetic $\mathbf{H} = (H_x, H_y, H_z)$ fields generated by the dipole source at the point $M = (x, y, z) \in R^3$ satisfy the Maxwell equations [4]

$$
\begin{aligned}
\nabla \times \mathbf{H} &= -i\omega\varepsilon'\mathbf{E} + \mathbf{p}\delta(|M - M'|), \quad z \neq z_l, \\
\nabla \times \mathbf{E} &= i\omega\mu\mathbf{H}
\end{aligned}
\tag{1}
$$

matching conditions at $z = z_l$, $l = 1, 2, \ldots, n - 1$,

$$
[\mathbf{n} \times \mathbf{E}] = [\mathbf{n} \times \mathbf{H}] = 0
$$

and radiation conditions, which have the form [5]

$$
\begin{aligned}
\partial_R \mathbf{E} - ik\mathbf{E} &= o(R^{-1}), \quad \partial_R \mathbf{H} - ik\mathbf{H} = o(R^{-1}), \\
R &\longrightarrow \infty
\end{aligned}
$$

for constant σ, ε, and μ and will be formulated below for layered media. Here, $\varepsilon' = \varepsilon + \dfrac{i\sigma}{\omega}$ is the complex permittivity, ω is the angular frequency, $\mathbf{p}$ is the dipole moment, δ is the three-dimensional Dirac delta function, $[\cdot]$ is the function jump, $\partial_R = \dfrac{\partial}{\partial R}$, $R = |M|$, $k = \omega\sqrt{\varepsilon'\mu}$, and $\operatorname{Re} k \geq 0$.

The vector potential $\mathbf{A} = (A_x, A_y, A_z)$, which is related to the fields $\mathbf{E}$ and $\mathbf{H}$ as

$$
\mathbf{H} = \frac{1}{\mu}\nabla \times \mathbf{A}, \quad \mathbf{E} = i\omega\left[\mathbf{A} + \nabla\left(\frac{\mu}{k^2}\nabla\frac{1}{\mu}\mathbf{A}\right)\right]
\tag{2}
$$

can be represented in the form [4]

$$
\mathbf{A} = \mathbf{G}(M, M')\mathbf{p}.
\tag{3}
$$

Here, $\mathbf{G} = (g^{ij})$, $i, j = 1, 2, 3$, is the Green's electric

tensor, where

$$g^{11} = G_\mu, \quad g^{22} = g^{11}, \quad g^{33} = \mu(z)\frac{G_{\varepsilon'}}{\varepsilon'(z')}, \quad (4)$$

$$g^{31} = \partial_x \Phi, \quad g^{32} = \partial_y \Phi,$$
$$g^{12} = g^{13} = g^{21} = g^{23} = 0, \quad (5)$$

$$G_\eta(M, M') = \frac{1}{2\pi}\int_0^\infty U_\eta^0(z, z', \lambda)\lambda J_0(\lambda r)d\lambda, \quad (6)$$

$$\Phi(M, M') = \frac{1}{2\pi}\int_0^\infty \varphi(z, z', \lambda)\lambda J_0(\lambda r)d\lambda, \quad (7)$$

$$\varphi(z, z', \lambda) = \lambda^{-2}(U_{\varepsilon'}^1 - \mu^{-1}\partial_z U_\mu^0), \quad (8)$$

$r = \sqrt{(x-x')^2 + (y-y')^2}$, J_0 is the zeroth order Bessel function, and $\eta = \mu, \varepsilon'$.

The Green's magnetic tensor **G*** is obtained by changing μ, ε', G_μ, $G_{\varepsilon'}$, Φ, g, and φ to $-\varepsilon'$, $-\mu$, $G_{\varepsilon'}$, G_μ, Φ^*, g^*, and φ^*, respectively, in Eqs. (4)–(8), where

$$\varphi^*(z, z', \lambda) = \lambda^{-2}(U_\mu^1 - \varepsilon'^{-1}\partial_z U_{\varepsilon'}^0).$$

Unknown functions U_η^α, $\alpha = 0, 1$, $\eta = \mu, \varepsilon'$, which enter into Eqs. (4)–(8), satisfy the equations

$$\frac{d}{dz}\left(\frac{1}{\eta}\frac{dU_\eta^\alpha}{dz}\right) - \frac{\lambda^2 - k^2}{\eta}U_\eta^\alpha = 0, \quad z \neq z_l, \quad (9)$$

matching conditions at $z = z_l$, $l = 1, 2, \ldots, n-1$,

$$[U_\eta^\alpha] = -\alpha\delta_p^l, \quad \left[\eta^{-1}\frac{dU_\eta^\alpha}{dz}\right] = (\alpha-1)\delta_p^l, \quad (10)$$

where δ_p^l is the Kronecker delta, and the partial radiation conditions at infinity [9]

$$\lim_{|z|\to\infty} U_\eta^\alpha. \quad (11)$$

CHOICE OF THE INTEGRATION CONTOUR

The efficiency of the methods for calculating the fundamental solutions of system (2) is determined primarily by the quality of algorithms employed for the approximate integration of expressions (4)–(7). Great difficulties arise in the case of small $\frac{|z-z'|}{r}$ values, where integrals of rapidly oscillating functions must be calculated with high accuracy.

We present a method for calculating integrals (4)–(7) for all $\frac{|z-z'|}{r}$ values with the transfer of the integration path into the complex plane. We consider integral (6) as an example. After standard transformation, it is reduced to the form

$$G(M, M') = \frac{1}{4\pi}\int_{-\infty}^\infty U(z, z', \lambda)\lambda H_0^{(1)}(\lambda r)d\lambda, \quad (12)$$

where $H_0^{(1)}$ is the zeroth order Hankel function of the first kind and $U(z, z', -\lambda) = U(z, z', \lambda)$. The following theorems are valid [10].

Theorem 1. *Let the coefficients of the problem specified by Eqs. (9)–(11) be piecewise constant functions of z and at least one of the four conditions*

$$\pm q_l[|\lambda_l|^2 C_l^{\pm 1} + \text{Re}(\lambda_l^2)] \pm t_l\text{Im}(\lambda_l^2) > 0,$$

$$\pm t_l[|\lambda_l|^2 C_l^{\pm 1} + \text{Re}(\lambda_l^2)] \mp q_l\text{Im}(\lambda_l^2) > 0,$$

be valid for all $l = 1, 2, \ldots, n$, where $q_l = \text{Re}(\eta_l)$, $t_l = \text{Im}(\eta_l)$,

$$C_l = \frac{1-|\alpha_l|}{1+|\alpha_l|}, \quad \alpha_l = \frac{\sin[\text{Im}(\lambda_l d_l)]\text{Re}(\lambda_l)}{\sinh[\text{Re}(\lambda_l d_l)]\text{Im}(\lambda_l)},$$

$\lambda_l^2 = \lambda^2 - k_l^2$, $\text{Re}(\lambda_l) \geq 0$, $d_l = z_{l-1} - z_l$. *In this case, the solution of the problem specified by Eqs. (9)–(11) is an analytic function of λ.*

Theorem 2. *For $|\lambda| \to \infty$, the solution of the problem specified by Eqs. (9)–(11) has the asymptotic representation*

$$U(z, z', \lambda) = C_0\exp(-|\lambda||z-z'|)[|\lambda|^{-1} + O(|\lambda|^{-2})],$$

where C_0 is a constant independent of $|\lambda|$.

At regular points, $|U(z, z', \lambda)| < \infty$ and tends uniformly to zero no slower than $|\lambda|^{-1}$ for $|\lambda| \to \infty$ according to Theorem 2. The Hankel function has the asymptotic representation [9]

$$H_0^{(1)}(\xi) = \sqrt{\frac{2}{\pi\xi}}\exp\left[i\left(\xi - \frac{\pi}{4}\right)\right][1 + O(|\xi|^{-1})]. \quad (13)$$

The integrand in Eq. (12) is a multivalued function of λ. It has $2j$ first-order branch points, where j is the number of different values k_l^2, $l = 1, 2, \ldots, n-1$. These points are determined from the relations $\lambda = \pm k_l$. The

appropriate sheet of the Riemann surface can be obtained from the condition

$$\text{Re}(\lambda_l) > 0, \tag{14}$$

which is valid in the presence of the necessary cuts. The cut lines are determined from the relations

$$\text{Im}(\lambda_l^2) = 0, \quad \text{Re}(\lambda_l^2) \le 0. \tag{15}$$

Under condition (14), the function U is limited according to theorems 1 and 2. This condition is valid everywhere on the chosen sheet excluding cuts. Therefore, the integration path in Eq. (12) can be deformed such that the region bounded by a new contour and the straight line $\text{Im}(\lambda) = 0$ consists only of regular points. In this case, a negative real part appears in the exponential index of Eq. (13), which ensures a rapid decrease in the integrand.

Thus, numerical integration of rapidly oscillating functions is reduced to the much simpler integration of slowly varying expressions with the known decreasing exponential weight function. The path that is most convenient for calculations should be chosen from all possible paths. The contour may be chosen by different methods. For example, when calculating numerous integrals of the type specified by Eqs. (4)–(7) for different M and M' values (which is necessary when solving inverse and other problems), it is appropriate to use one common contour for which

$$\text{Im}(\lambda) = |\text{Re}(\lambda)|, \quad |\lambda| \longrightarrow \infty.$$

In this case, integrands decrease as $\exp[-|\lambda|(|z - z'| + r)]$ and oscillations are absent.

CALCULATION OF INTEGRALS

Since the function U in integrals (5)–(7) slowly varies beyond the segment $[0, b]$, where $b > \max\limits_{1 \le l \le n} [\text{Re}(k_l)$, for most models of the layered medium, we represent integral (6) as the sum of two integrals

$$G = G_1 + G_2, \quad G_i = \frac{1}{2\pi}\int\limits_0^\infty U_i \lambda J_0(\lambda r)d\lambda, \tag{16}$$

$$i = 1, 2,$$

where

$$U_1 = U - U_2, \quad U_2(\lambda) = \begin{cases} U(z, z', b), & \lambda \le b, \\ U(z, z', \lambda), & \lambda \ge b. \end{cases}$$

For the integral G_1 in Eq. (16), we divide the segment $[0, b]$ into $L + 1$ parts $0 \le \lambda_0 < \lambda_1 < \ldots < \lambda_L = b$.

Taking into account the evenness of function U_1, we replace it by its interpolation polynomial

$$U_1 \approx c_0^k + c_1^k \lambda^2 + c_2^k \lambda^4 \tag{17}$$

with the interpolation nodes λ_k, $\dfrac{\lambda_k + \lambda_{k+1}}{2}$, λ_{k+1} in each segment $[\lambda_k, \lambda_{k+1}]$. Substituting Eq. (17) into Eq. (16) and performing simple algebra, we obtain

$$G_1 \approx \sum_{k=0}^{L}\sum_{j=0}^{2}\frac{d_j^k I_{2j+1}(\nu_k)}{2\pi r^{2j+2}}, \quad I_p(t) = \int\limits_0^t \lambda^p J_0(\lambda)d\lambda, \tag{18}$$

where

$$\nu_k = \lambda_k r, \quad d_j^k = c_j^k - c_j^{k+1}, \quad c_j^{L+1} = 0.$$

Using the recurrence relations [11]

$$I_1(t) = tJ_1(t), \tag{19}$$
$$I_k(t) = t^k J_1(t) + (k-1)t^{k-1}J_0(t) - (k-1)^2 I_{k-2}(t)$$

in Eq. (18), we finally obtain

$$G_1 \approx \frac{1}{\pi}\sum_{k=1}^{L}\frac{\lambda_k}{r}\left\{\frac{\lambda_k}{r}J_0(\nu_k)[d_1^k + 2d_2^k(\nu_k^2 - 8)] \right.$$

$$\left. - 2J_1(\nu_k)[d_1^k + 4d_2^k(\nu_k^2 - 4)]\right\}. \tag{20}$$

This formula makes it possible to approximately calculate integrals (18) for various b values. If zeros λ_k of the Bessel functions are taken as nodes, formula (20) is considerably simplified and $J_0(\lambda_k)$ can be tabulated.

We represent the integral G_2 in Eq. (16) as the sum of two integrals with the integration ranges $(-\infty, 0)$ and $(0, \infty)$. Changing variables $\lambda = \lambda(\rho) = \sqrt{2}\rho S$ and $\lambda = \bar{\lambda}(\rho)$ in the second and first integrals, respectively, we obtain

$$G_2 = \frac{\sqrt{2}}{8\pi}\int\limits_0^\infty \{U_2[\lambda(\rho)]D(\rho) + U_2[\bar{\lambda}(\rho)]\bar{D}(\rho)\}d\rho, \tag{21}$$

where $S = \exp\left(-\dfrac{i\pi}{4}\right)$, $D(\rho) = \lambda(\rho)H_1^0[\lambda(\rho)r]$, and $\bar{\lambda}$

and $\overline{D}$ are the complex conjugate expressions for λ and D, respectively.

With such a change of variables, the parts of the plane that are bounded by the new contours and the straight line $\text{Im}\lambda = 0$ belong to the region of the analy-

Table

f	x	z'	[6]		[8]		This work	
			$\mathrm{Re}\,H_z$	$\mathrm{Im}\,H_z$	$\mathrm{Re}\,H_z$	$\mathrm{Im}\,H_z$	$\mathrm{Re}\,H_z$	$\mathrm{Im}\,H_z$
2.5	0.5	0	2.0581×10^{-1}	1.3041×10^{-1}	2.0581×10^{-1}	1.3041×10^{-1}	2.0581×10^{-1}	1.3041×10^{-1}
		0.1	0.0128×10^{-1}	1.3373×10^{-2}	0.0128×10^{-1}	1.3373×10^{-2}	0.0128×10^{-1}	1.3373×10^{-2}
	5	0	3.3458×10^{-6}	2.7673×10^{-5}	3.3458×10^{-6}	2.7673×10^{-5}	3.3458×10^{-6}	2.7673×10^{-5}
		0.1	-5.1648×10^{-5}	-3.4641×10^{-6}	-5.1646×10^{-5}	-3.4602×10^{-6}	-5.1648×10^{-5}	-3.4603×10^{-6}
10	0.5	0	4.0825×10^{-2}	1.1389×10^{-1}	4.0833×10^{-2}	1.1389×10^{-1}	4.0833×10^{-2}	1.1389×10^{-1}
		0.1	-2.8285×10^{-1}	-5.6839×10^{-2}	-2.8285×10^{-1}	-5.6840×10^{-2}	-2.8285×10^{-1}	-5.6839×10^{-2}
	5	0	-4.4513×10^{-8}	9.7293×10^{-6}	-6.2845×10^{-8}	9.7303×10^{-6}	-4.2895×10^{-8}	9.7301×10^{-6}
		0.1	2.1718×10^{-6}	-8.2423×10^{-7}	2.1712×10^{-6}	-1.2750×10^{-6}	2.1717×10^{-6}	-1.2748×10^{-6}
40	0.5	0	-1.4718×10^{-3}	2.3860×10^{-2}	-1.4810×10^{-3}	2.3855×10^{-2}	-1.4718×10^{-3}	2.3860×10^{-2}
		0.1	7.4067×10^{-3}	5.714×10^{-5}	7.4067×10^{-5}	5.7142×10^{-5}	7.4067×10^{-5}	5.7142×10^{-5}
	5	0	-0.4230×10^{-10}	2.4188×10^{-6}	-1.2780×10^{-8}	2.4140×10^{-6}	-0.0150×10^{-10}	2.4189×10^{-6}
		0.1	1.4559×10^{-9}	-2.1295×10^{-8}	1.4790×10^{-9}	4.1970×10^{-10}	1.4559×10^{-9}	4.1050×10^{-10}

ticity of the function U_2, and the asymptotic equality $|\mathrm{Im}\,\rho(\lambda)| = \mathrm{Re}\,\lambda(\rho)$ is valid for $\rho \longrightarrow \infty$ [1].

The integrand in expression (21) is limited for $\rho \longrightarrow \infty$. Therefore, quadrature formulas with exponential weights for the range $(0, \infty)$ are applicable to this expression [12].

NUMERICAL EXPERIMENTS

The above approach has been successfully tested for a wide class of models of layered media with arbitrary positions of sources and observation points. The accuracy of calculations of the components of electromagnetic field tensors (2) is determined by comparing the calculation results with similar results obtained by other methods in [6, 8]. In the example below, the calculation model is described, and results of one series of test calculations, which are performed using various methods, are analyzed.

Example. We consider a three-layered medium with the parameters $\varepsilon_l = \varepsilon_0$, $\mu_l = \mu_0$, $l = 1, 2, 3$ (ε_0 and μ_0 are the permittivity and permeability of free space, respectively), $\sigma_1 = 0$, $\sigma_2 = 1$ $(\Omega\,\mathrm{m})^{-1}$, $\sigma_3 = 0.01$ $(\Omega\,\mathrm{m})^{-1}$, $z_1 = 0$, and $z_2 = -500$. At points $M_{ks} = (x_k, 0, z_s)$ of this medium, the vertical component H_z is calculated for various oscillation frequencies ω_n; this vertical component belongs to the magnetic field generated by the harmonic electric dipole with moment $\mathbf{p} = (0, 1, 0)$, which

is placed at the point $M'_s = (0, 0, z_s)$. The table presents x_k (in meters), z_s (in meters), and $f_n = \dfrac{\omega_n}{2\pi}$ (in Hertz).

Note. The parameters of the model are chosen according to the applicability of the method for calculating integrals ($\mathrm{Re}(k_l^2) = 0$), which is described in [6].

According to Eqs. (5) and (7), the vertical component H_z of the magnetic field is given by the expression

$$H_z(M) = \frac{1}{\mu(z)} \frac{\partial G_\mu^0(M, M')}{\partial x}$$

$$= -\frac{x - x'}{2\pi r \mu(z)} \int_0^\infty \{ U_\mu^0[z, z', \lambda(\rho)]\lambda^3(\rho) \quad (22)$$

$$+ U_\mu^0[z, z', \bar{\lambda}(\rho)]\bar{\lambda}^3(\rho) \} H_1^{(1)}[\lambda(\rho)r]\rho^{-1} d\rho,$$

where $\lambda(\rho) = \rho \exp(i\varphi)$.

The table presents the H_z values that were obtained in [6, 8] and calculated by the algorithm described above.

Analysis shows that the results coincide for most initial data. For $z' > 0.1$, all methods yield correct results, which are presented in the table. However, for $z' < 0.01$, the H_z values obtained in [8] significantly differ from the values obtained by two other methods.
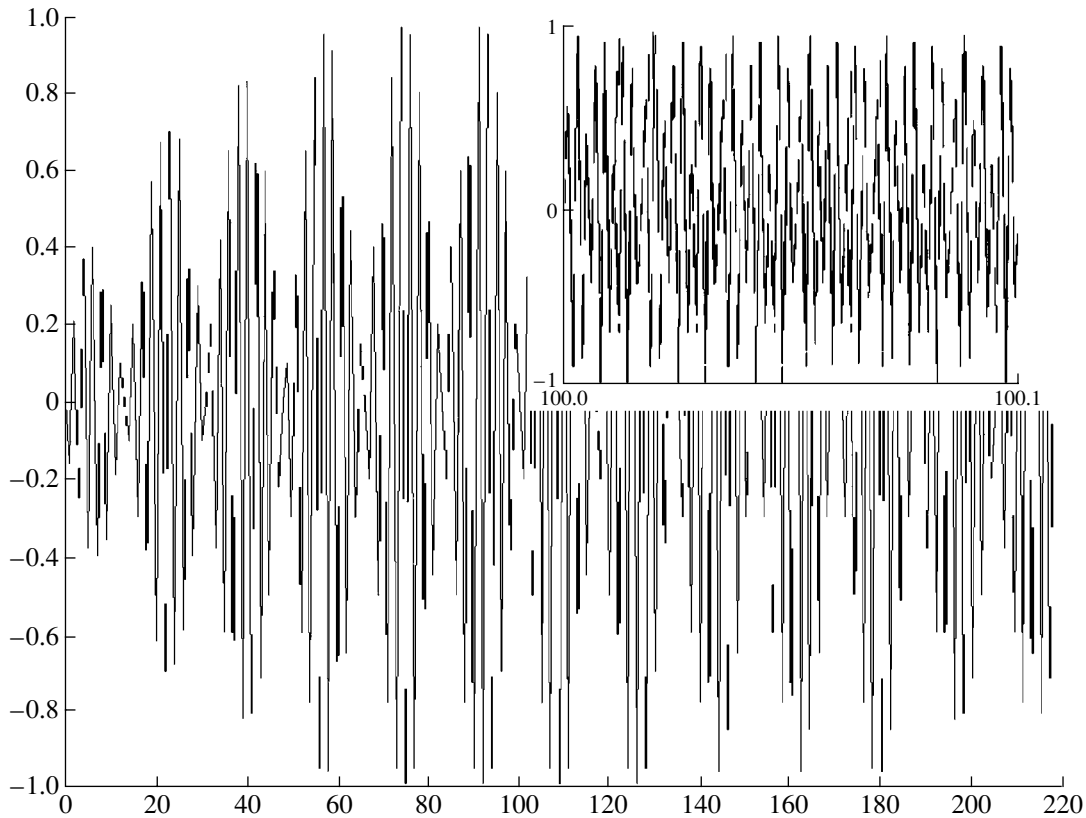
Fig. 1. Real part of the integrand of Eq. (20) and its fragment in the interval (100, 100.1) for $\varphi = 0$.

These differences arise because the integrand in the first integral in Eq. (22) oscillates rapidly and decreases slowly with increasing λ for "bad" positions of the source and observation point.

The real part of this function normalized to its maximum absolute value in the λ interval under consideration is shown in Fig. 1, where the abscissa axis shows λ values in a 1 : 1000 ratio for $z' = 0.005$. The other parameters correspond to the first variant of the initial data presented in the table. The contribution of the imaginary part is insignificant.

The plot itself is similar to its fragment for the (100, 100.1) interval, which is extended by a factor of 2000 along the horizontal. One cause of the latter phenomenon is that the discretization steps are insufficiently small in both cases for the accurate imaging of this rapidly oscillating function. One discretization step corresponds to approximately 300 changes of the sign of the integrand.

As was shown above, the transition to the complex plane and choice of the appropriate integration path enable one to remove oscillations and to ensure rapid decrease in the integrand with increasing λ. Figure 2 shows the normalized plots of the (solid line) real and (dash–dotted line) imaginary parts of the integrand in Eq. (20) for $\varphi = \dfrac{\pi}{4}$.

When calculating integrals (4)–(7), most computer time is spent on the calculation of expressions the overwhelming majority of which depend only on the model parameters and $|\lambda|$. Computer experiments with simultaneous calculation of numerous integrals (4)–(7) show that the body of the required calculations can be consid-
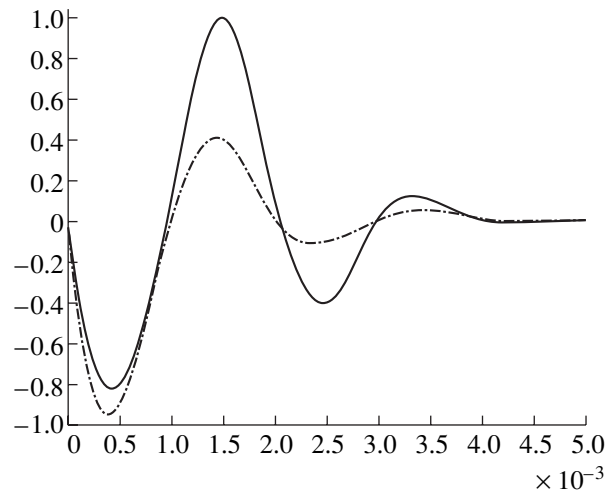

Fig. 2. (Solid line) Real and (dash–dotted line) imaginary parts of the integrand of Eq. (20) for $\varphi = \dfrac{\pi}{4}$.

erably reduced in this case. Computer time depends only slightly on the complexity of the model and is close to the time allotted to the simplest model consisting of two homogeneous half-spaces.

ACKNOWLEDGMENTS

REFERENCES

1. V. N. Mazalov, V. V. Peresvetov, and S. I. Smagin, *Modeling Electromagnetic Fields in Layered Media with Inclusions* (Dal'nauka, Vladivostok, 2000) [in Russian].
2. S. I. Smagin, Zh. Vychisl. Mat. Mat. Fiz. **29** (1), 1663 (1989).
3. S. I. Smagin, *Integral Equations in Diffraction Problems* (Dal'nauka, Vladivostok, 1995) [in Russian].
4. V. I. Dmitriev, Vychisl. Metody Programmir., No. 10, 55 (1968).
5. N. S. Koshlyakov, *Partial Differential Equations of Mathematical Physics* (Vysshaya Shkola, Moscow, 1970) [in Russian].
6. W. L. Anderson, Geophysics **44**, 1287 (1979).
7. V. I. Selin, Zh. Vychisl. Mat. Mat. Fiz. **40** (1), 91 (2000).
8. A. A. Slipchenko and V. A. Filatov, Geol. Geofiz., No. 5, 130 (1987).
9. L. A. Taborovskiĭ, *Application of the Integral-Equation Method in Geoelectricity* (Nauka, Moscow, 1975) [in Russian].
10. S. I. Smagin, Zh. Vychisl. Mat. Mat. Fiz. **26** (8), 1234 (1986).
11. I. S. Gradshteyn and I. M. Ryzhik, *Table of Integrals, Series, and Products* (Nauka, Moscow, 1971; Academic, New York, 1980).
12. V. I. Krylov, *Approximate Calculation of Integrals* (Macmillan, New York, 1962; Nauka, Moscow, 1967).
13. V. N. Dmitriev and G. V. Akkuratov, *Mathematical Simulation of Seismic Frequency Sounding* (Mosk. Gos. Univ., Moscow, 1985) [in Russian].

Translated by R. Tyapaev

========= **MECHANICS** =========

On the Theory of Longitudinal and Transverse Vibrations of Preliminary Stressed Beams and Rods

Yu. A. Dem'yanov

Presented by Academician E.I. Shemyakin October 18, 2004

By way of analogy with studies [1, 2], it is shown that the contributions of the longitudinal and transverse components of dynamic deformations to dynamic loading of the neutral (middle) surface in preliminary stressed beams and rods are of the same order of magnitude.

Taking this fact into consideration along with the hypothesis of the plane cross section, we derive an equation for longitudinal vibrations of the middle surface. In the elastic case, these vibrations are described by the linear inhomogeneous equation. The forced vibrations that arise in this case are determined by the transverse and bending vibrations. Based on analysis of the set of equations obtained, we can conclude that the forced vibrations occur at frequencies of the transverse and bending vibrations. Methods for the generalization of the results obtained are indicated.

1. The equations for changes in the momentum and angular momentum of a beam (rod) cross section have the form [3]

$$\rho \frac{\partial^2 x}{\partial t^2}$$
$$= \frac{\partial}{\partial s}(T\cos\theta) - \frac{\partial}{\partial s}(N\sin\theta) + q_\tau\cos\theta - q_n\sin\theta, \tag{1}$$

$$\rho \frac{\partial^2 y}{\partial t^2}$$
$$= \frac{\partial}{\partial s}(T\sin\theta) + \frac{\partial}{\partial s}(N\cos\theta) + q_\tau\sin\theta + q_n\cos\theta, \tag{2}$$

$$N = \rho \frac{J}{F}\frac{\partial^2\theta}{\partial t^2} - \frac{\partial M}{\partial s} - \mu, \quad M = EJ\frac{\partial\theta}{\partial s}, \tag{3}$$

Moscow State University of Forestry,
Pervaya Institutskaya ul. 1, Mytishchi,
Moscow oblast, 141005 Russia

where t is time; s is the Lagrangian coordinate that coincides with the Cartesian longitudinal coordinate, which is measured along the direction of the initially rectilinear stress-free beam; x and y are the longitudinal and transverse displacements of the middle surface, respectively; T, N and q_τ, q_n are the tangential and normal forces and the linear loads (linear densities of external forces), respectively; ρ is the beam-material density; θ is the inclination angle of the middle surface to the initial direction of the beam; F is the beam cross-section area; J is the moment of inertia of the cross-section area; E is the Young modulus; and μ is the linear density of the external moments. The cross-section area is assumed to be symmetric with respect to the middle surface. In the case of small deviations from the initial stress state, the deformation increment of the middle surface (by analogy with the deformation increment of a string [1, 2]) has the form

$$\Delta e = \frac{\partial \bar{x}}{\partial s} + \frac{1}{2(1 + e_0)}\left(\frac{\partial y}{\partial s}\right)^2.$$

Here, $\bar{x} = x - e_0(s - s_0)$, where s_0 is the fixation plane. Therefore, the contributions of the longitudinal and transverse components of the dynamic deformations to the dynamic loading are of the same order of magnitude. It is evident that

$$\cos\theta \sim \frac{1 + \dfrac{\partial x}{\partial s}}{1 + e} \sim \frac{1 + e_0 + \dfrac{\partial \bar{x}}{\partial s}}{1 + e_0 + \dfrac{\partial \bar{x}}{\partial s} + \dfrac{1}{2(1 + e_0)}\left(\dfrac{\partial y}{\partial s}\right)^2}$$
$$\sim 1 - \frac{1}{2(1 + e_0)}\left(\frac{\partial y}{\partial s}\right)^2,$$

$$\sin\theta \sim \theta \sim \frac{1}{1 + e_0}\frac{\partial y}{\partial s}, \quad T \sim E(e_0 + \Delta e).$$

Then, Eqs. (1)–(3) take the form

$$\rho\frac{\partial^2 \bar{x}}{\partial t^2} = E\frac{\partial^2 \bar{x}}{\partial s^2} + \Phi_1,$$

$$\Phi_1 = \frac{E}{2(1+e_0)^2}\frac{\partial}{\partial s}\left(\frac{\partial y}{\partial s}\right)^2 - \frac{1}{(1+e_0)^2}\frac{\partial}{\partial s}\left(N\frac{\partial y}{\partial s}\right)$$

$$+ q_\tau - \frac{q_n}{1+e_0}\frac{\partial y}{\partial s}; \qquad (4)$$

$$\rho\frac{\partial^2 y}{\partial t^2} = \frac{Ee_0}{1+e_0}\frac{\partial^2 y}{\partial s^2} + \frac{EJ}{1+e_0}\frac{\partial^4 y}{\partial s^4}$$

$$- \frac{\rho J}{F(1+e_0)^2}\frac{\partial^4 y}{\partial t^2 \partial s^2} + \frac{q_\tau}{1+e_0}\frac{\partial y}{\partial s} + q_n + \frac{\partial \mu}{\partial s}; \qquad (5)$$

$$N = \rho\frac{J}{F(1+e_0)}\frac{\partial^3 y}{\partial t^2 \partial s} - \frac{EJ}{1+e_0}\frac{\partial^3 y}{\partial s^3} - \mu. \qquad (6)$$

The solution of Eq. (5) makes it possible to find the spectrum of transverse vibrations $y = y(s, t)$. In the case that $T \sim Ee$, Eq. (4) turns out to be the linear inhomogeneous second-order equation in terms of $\bar{x} = \bar{x}(s, t)$. This implies the presence of both natural and forced vibrations that depend on the spectrum of transverse vibrations $y = y(s, t)$.

By way of analogy with [1], it is possible (if necessary) to find for the functions $y(s, t)$ and $\bar{x}(s, t)$ the following terms of asymptotic expansions into the series in a small parameter ε characterizing the increment of the total deformation:

$$\bar{x} = \varepsilon(X_1(s, t) + \varepsilon X_2(s, t) + \ldots),$$

$$y = \varepsilon^{1/2}(Y_1(s, t) + \varepsilon Y_2(s, t) + \ldots).$$

The form of equations for X_1 and Y_1 naturally coincides with Eqs. (4) and (5) (after passing to new functions in both of them).

2. For a rigidly fixed or pivoted beam (rod) and in the case that $s = 0$ and $s = l$, homogeneous equation (5) (at $q_n = q_\tau = \mu = 0$) can be solved by the method of separation of variables. To this end, this equation should be transformed to the dimensionless form

$$\frac{\partial^2 y}{\partial \bar{t}^2} = \frac{e_0}{1+e_0}\frac{\partial^2 y}{\partial \bar{s}^2} + \alpha\left(\frac{\partial^4 y}{\partial \bar{s}^4} - \frac{\partial^4 y}{\partial \bar{t}^2 \partial \bar{s}^2}\right), \qquad (7)$$

where

$$s = l\bar{s}, \quad t = \frac{l}{a_0}\bar{t}, \text{ and } \alpha = \frac{J}{(1+e_0)l^2 F}.$$

Below, bars standing over the variables are omitted.

We seek the particular solution in the form $y = T_k(t)S_k(s)$. Then,

$$T_k'' = -\omega_k^2 T_k,$$

$$S_k^{IV} + \left[\frac{e_0}{\alpha(1+e_0)} + \omega_k^2\right]S_k'' + \frac{\omega_k^2}{\alpha}S_k = 0. \qquad (8)$$

In what follows, we show that, starting from a certain value ω_{k0}, $\omega_k^2 > 0$. The particular solutions for $S_k(s)$ are $\exp(m_k s)$, where m_k satisfies the secular equation

$$m_k^4 + \left[\frac{e_0}{\alpha(1+e_0)} + \omega_k^2\right]m_k^2 + \frac{\omega_k^2}{\alpha} = 0,$$

or

$$n_k^2 + \left[\frac{e_0}{\alpha(1+e_0)} + \omega_k^2\right]n_k + \frac{\omega_k^2}{\alpha} = 0.$$

Hence, we arrive at

$$n_{k1} = -\frac{1}{2}\left[\frac{e_0}{\alpha(1+e_0)} + \omega_k^2\right]$$

$$+ \sqrt{\frac{1}{4}\left[\frac{e_0}{\alpha(1+e_0)} + \omega_k^2\right]^2 - \frac{\omega_k^2}{\alpha}},$$

$$n_{k2} = -\frac{1}{2}\left[\frac{e_0}{\alpha(1+e_0)} + \omega_k^2\right] \qquad (9)$$

$$- \sqrt{\frac{1}{4}\left[\frac{e_0}{\alpha(1+e_0)} + \omega_k^2\right]^2 - \frac{\omega_k^2}{\alpha}}.$$

From (9), it follows that, starting from ω_{k0}, which satisfies the condition

$$\frac{1}{2}\left[\frac{e_0}{\alpha(1+e_0)} + \omega_{k0}^2\right] \geq \frac{\omega_{k0}}{\sqrt{\alpha}},$$

the consequent values of $\omega_k > \omega_{k0}$ meet the condition $\omega_k^2 > 0$ and, correspondingly, $n_k < 0$. Hence,

$$m_{k1} = \sqrt{n_{k1}}, \quad m_{k3} = -\sqrt{n_{k1}}, \quad m_{k2} = \sqrt{n_{k2}},$$

$$\text{and } m_{k4} = -\sqrt{n_{k2}}.$$

Note that all values m_{k1} starting from ω_{k0} are purely imaginary.

It is possible to evaluate the asymptotic expressions for m_k in two cases of great practical importance:

(a) the case $\alpha \omega_k^2 \longrightarrow 0$, which corresponds to a thin rod (beam) and

(b) the case $\alpha \omega_k^2 \longrightarrow \infty$, which corresponds to the spectrum of high-frequency vibrations.

We have for case (a)

$$n_{k1} = -\frac{1 + e_0}{e_0} \omega_k^2 \left[1 + \frac{1 + e_0}{e_0} \alpha \omega_k^2 + O(\alpha^2 \omega_k^4) \right],$$

$$n_{k2} = -\frac{e_0}{(1 + e_0)\alpha} \omega_k^2 \left[1 - \frac{1 + e_0}{e_0} \alpha \omega_k^2 + O(\alpha^2 \omega_k^4) \right],$$
(10)

and for case (b)

$$n_{k1} = -\omega_k^2 + \frac{1}{\alpha} + O\left(\frac{1}{\alpha \omega_k^2}\right), \quad n_{k2} = -\frac{1}{\alpha} + O\left(\frac{1}{\alpha \omega_k^2}\right). \quad (11)$$

Thus, $S_k(s) = \sum_{i=1}^{4} A_i e^{m_{ki} s}$.

In the case when, for example, we address a rigidly fixed beam in the cross sections $s = 0$ and $s = 1$, the boundary conditions for $y(s, t)$ are

$$y(0, t) = y(1, t) = \frac{\partial y}{\partial s}(0, t) = \frac{\partial y}{\partial s}(1, t) = 0.$$

Hence, we arrive at the following conditions for $S_k(s)$:

$$S_k(0) = S_k(1) = S_k'(0) = S_k'(1) = 0,$$

or

$$\sum_{i=1}^{4} A_i = \sum_{i=1}^{4} A_i e^{m_{ki}}$$

$$= \sum_{i=1}^{4} A_i m_{ki} = \sum_{i=1}^{4} A_i m_{ki} e^{m_{ki}} = 0.$$
(12)

As is well known, $A_i \neq 0$ ensured that the fourth-order determinant composed of coefficients 1, $e^{m_{ki}}$, m_{ki}, and $m_{ki} e^{m_{ki}}$ of the set of Eqs. (10) is equal to zero. After simple but rather cumbersome calculations, we obtain

$$(m_{k4} - m_{k2})(m_{k2} - m_{k1}) e^{(m_{k3} + m_{k4})}$$

$$+ (m_{k3} - m_{k2})(m_{k4} - m_{k1}) e^{(m_{k2} + m_{k3})}$$

$$+ (m_{k1} - m_{k4})(m_{k2} - m_{k3}) e^{(m_{k1} + m_{k4})}$$

$$+ (m_{k2} - m_{k1})(m_{k4} - m_{k3}) e^{(m_{k1} + m_{k2})}$$

$$+ (m_{k2} - m_{k4})(m_{k3} - m_{k4}) e^{(m_2 + m_{k4})}$$

$$+ (m_{k1} - m_{k3})(m_{k4} - m_{k2}) e^{(m_{k1} - m_{k3})} = 0,$$

or, with allowance for

$$m_{k1} + m_{k3} = 0, \quad m_{k2} + m_{k4} = 0,$$

$$\text{and } m_{k1} m_{k2} = m_{k3} m_{k4},$$

we finally find

$$\frac{e^{ik^-} + e^{-ik^-} - 2}{(k^-)^2} = \frac{e^{ik^+} + e^{-ik^+} - 2}{(k^+)^2}, \quad ik^- = m_{k2} - m_{k1},$$
(13)

$$ik^+ = m_{k2} + m_{k1}.$$

In cases (a) and (b) and provided that $\omega_k > \omega_{k0}$, all the quantities k^+ and k^- are real and condition (13) takes the form

$$\frac{1 - \cos k^-}{(k^-)^2} = \frac{1 - \cos k^+}{(k^+)^2},$$
(14)

or

$$\frac{\sin(k^-/2)}{k^-/2} = \pm \frac{\sin(k^+/2)}{k^+/2}.$$
(15)

From condition (15) (with allowance for expressions for m_{k1} and m_{k2}), we find the spectrum of the frequencies $\omega_k = \beta + \gamma k \pi$, where k is an integer ($k \gg 1$).

3. It follows from the preceding sections that the solution $y(s, t)$ is given by the superposition of the terms $T_k(t) S_k(s)$. Here, the functions $T_k(t)$ and $S_k(s)$ are the sums of two and four trigonometric functions, respectively. Therefore, the derivative $\frac{\partial y}{\partial s}$, this derivative squared $\left(\frac{\partial y}{\partial s}\right)^2$, and the functions N and $N\frac{\partial y}{\partial s}$ are superpositions of trigonometric functions with a frequency equal to the sum of the frequencies of the individual components. The same conclusion is true for the function Φ_1 (in the case of a string at $N = 0$, which is shown in [2]). Thus, the forced longitudinal vibrations determined by the partial solutions of inhomogeneous Eq. (4) occur at frequencies equal to the sum of the ini-

tial frequencies of the transverse vibrations. In the case that the frequencies of natural and forced vibrations coincide, there appears (as in the case of string vibrations [2]) the phenomenon of resonance between these forms of vibrations. In the future, we intend to extend this conclusion to the case of vibrations of stressed plates and shells.

ACKNOWLEDGMENTS

REFERENCES

1. Yu. A. Dem'yanov, Dokl. Akad. Nauk **369** (4), 461 (1999) [Dokl. Math. **60**, 456 (1999)].

2. Yu. A. Dem'yanov, D. V. Dement'eva, and A. A. Malashin, Prikl. Mat. Mekh. **67**, 273 (2003).

3. V. A. Svetlitskiĭ, *Mechanics of Rods* (Vysshaya Shkola, Moscow, 1987), Vols. 1, 2 [in Russian].

4. A. E. H. Love, *A Treatise on the Mathematical Theory of Elasticity* (Dover, New York, 1944; Glav. Red. Obshchetekhn. Lit. i Nomografii, Moscow, 1953).

Translated by Yu. Vishnyakov

===== **MECHANICS** =====

On the Effect of a Porous Insert in the Supersonic Section of a Nozzle upon Change in Its Thrust

V. N. Zaĭkovskiĭ[1], **V. P. Kiselev**[1], **S. P. Kiselev**[1], **B. M. Melamed**[1],
Corresponding Member of the RAS M. I. Sokolovskiĭ[2], **A. I. Todoshchenko**[2],
G. V. Trubacheev[1], and **Corresponding Member of the RAS V. M. Fomin**[1]

A nozzle in which the thermal energy of gases is converted into the kinetic energy of a gas jet is a basic element of the rocket engine. If the pressure in the external medium (or in the engine combustion chamber) varies, the conventional nozzle will not be optimal throughout the entire pressure range: it operates either in the underexpansion or overexpansion mode. The nozzle would be ideal if its expansion degree followed the changes in the external (internal) pressure, preserving an equality between environmental pressure and internal pressure at the nozzle cross section; but it is very difficult to realize this mode.

There are various approaches to thrust-loss control in the case of overexpansion. For example, Semenov [1] proposed the use of air blow through an annular slot into the supercritical nozzle section operating in the overexpansion mode. However, this is only a single-step variation in the degree of the nozzle off-design.

The heat-resistant gas-permeable porous materials that are now available equalize, based on their gas permeability, the pressure inside the funnel with that in the environment at the nozzle section operating in the overexpansion mode, i.e., render the nozzle self-adjustable without any additional devices. Therefore, investigation of the effect of a porous insert on the nozzle thrust represents an urgent problem.

To experimentally study this effect, we used a differential pendulum setup including reference and working nozzles. The installation was freely suspended on a bearing unit (Fig. 1) and was connected to the fixed base only by an elastic element of the strain-gauge balance; there were no other rigid bonds. The key measuring principle used in this installation is the comparison of the jet thrusts of two nozzles (working and refer-

ence), oriented in mutually opposite directions. To determine the effect of the porous insert on changes in the thrust of the nozzle, we performed two experiments with the same prechamber pressure p_0. In the first experiment, the working nozzle with continuous walls was used, and, in the second, the porous insert was mounted in the supersonic section of the working nozzle (schematically shown by dashed lines in Fig. 2). As a result, the change in the thrust of the nozzle was determined from two experiments carried out with the identical prechamber pressure p_0. The experimental procedure was described in more detail in [2]. The supersonic section of the nozzle was formed by a cone with a half-opening angle of $\alpha = 8°$. The porous insert is the duralumin section $x_1 < x < x_2$ of the conic nozzle in which 1050 round holes approximately 1 mm in diameter with a total relative area of 18% were drilled. The radius of the minimum nozzle section is $r_* = 19.2$ mm; the length of the supersonic section is $x_{sr} = 147$ mm; and the coordinates of the porous section are $x_1 = 82$ mm and $x_2 = 130$ mm (Fig. 2).
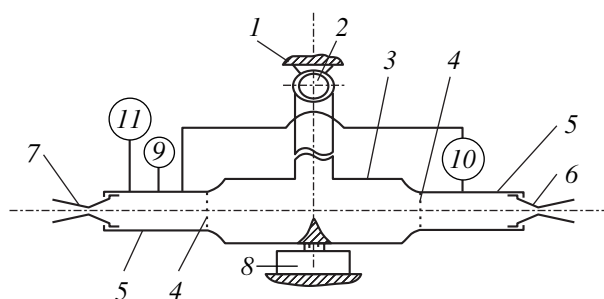
Fig. 1. Block diagram of the measuring system of the installation: (*1*) basic unit, (*2*) feeding pipeline, (*3*) receiver, (*4*) dividing nozzle arrays, (*5*) reference and working prechambers, (*6*) working nozzle under investigation, (*7*) reference nozzle, (*8*) strain-gauge balance, (*9*) deceleration-pressure (p_0) gauge in the reference prechamber, (*10*) gauge of deceleration-pressure difference Δp in the reference and investigated prechambers, and (*11*) thermocouple of deceleration temperature T in the reference prechamber.

---

[1] *Institute of Theoretical and Applied Mechanics,*
  Siberian Division, Russian Academy of Sciences,
  pr. Akademika Lavrent'eva 13, Novosibirsk, 630090 Russia
  e-mail: melamed@itam.nsc.ru

[2] *OAO NPO Iskra,*
  ul. Akademika Vedeneeva 28, Perm, 614038 Russia

As the working gas, we used compressed air at room temperature $T_0 = 300$ K and pressure p_0 varied from 10^6 to 4.5×10^6 Pa. Compressed air was fed through dividing arrays into the working and reference nozzles, where it was accelerated to a supersonic velocity.

The gas flow in the nozzle with the porous insert was mathematically simulated assuming that perturbations introduced by the porous section were small. Therefore, the solution was represented as $f = \tilde{f} + f'$. As $\tilde{f}$, we chose the steady gas flow in the nozzle considered in the quasi-one-dimensional approximation. For each nozzle cross section $S(x) = \pi r^2(x)$, we determined the velocity factor $\lambda(x)$ from the equation [3]

$$\frac{S_*}{S(x)} = \lambda \left\{ \frac{\gamma+1}{2} \left(1 - \frac{\gamma-1}{\gamma+1} \lambda^2 \right) \right\}^{\frac{1}{\gamma-1}} \qquad (1)$$

and then found the pressure $\tilde{p}(\lambda)$, density $\tilde{\rho}(\lambda)$, and temperatures $\tilde{T}(\lambda)$ from isentropic formulas. The equations for perturbations of the potential φ have the form [3]

$$(1 - M^2)\frac{\partial^2 \varphi'}{\partial x^2} + \frac{\partial^2 \varphi'}{\partial r^2} + \frac{1}{r}\frac{\partial \varphi'}{\partial r} = 0 \qquad (2)$$

and differ from the planar case by the term $\dfrac{1}{r}\dfrac{\partial \varphi'}{\partial r}$. In this case, $M \approx 3$, perturbations are concentrated near the nozzle wall and do not reach the nozzle axis (see Fig. 2). Therefore, when determining perturbations in Eq. (2), it is possible to neglect the third term $\dfrac{1}{r}\dfrac{\partial \varphi'}{\partial r}$. Then, Eq. (2) coincides with the corresponding equation for the planar case [3]

$$(1 - M^2)\frac{\partial^2 \varphi'}{\partial x^2} + \frac{\partial^2 \varphi'}{\partial r^2} = 0, \quad u' = \frac{\partial \varphi'}{\partial x}, \quad v' = \frac{\partial \varphi'}{\partial r},$$

$$p' = -\tilde{\rho}\tilde{u}u', \quad M = \frac{\tilde{u}}{\tilde{c}}, \quad \tilde{c} = \sqrt{\frac{\gamma \tilde{p}}{\tilde{\rho}}}. \qquad (3)$$

The solution of Eqs. (3) is known [3] and is given by the formulas

$$v' \pm \sqrt{M^2 - 1}\, u' = A_{1,2}, \quad \sin\beta = \pm\frac{1}{M}, \qquad (4)$$

where $A_{1,2}$ are the constants of two families of characteristics, which are determined by the boundary conditions on the wall. If the size of pores is sufficiently
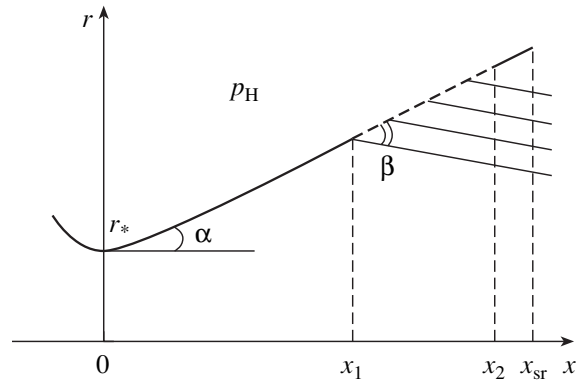
large, and the effect of viscosity is weak, the Nikol'skiĭ boundary condition [4] is valid,

$$u' = \frac{m_2}{m_1}\frac{v'}{\sqrt{M^2 - 1}}, \quad m_1 + m_2 = 1, \qquad (5)$$

where m_1 is the porosity determined by the ratio of the area of holes to the total area of the nozzle porous section. To determine the gas outflow velocity v', every pore was simulated by a micronozzle. From known formulas [3], we obtain

$$v' = \begin{cases} \dfrac{\xi m_1 c}{\sqrt{\gamma}} \sqrt{\dfrac{p - p_H}{p}}, & 0 < \dfrac{p - p_H}{p} < \dfrac{1}{2}, \\[4mm] \dfrac{\xi m_1 c}{\sqrt{2\gamma}}, & \dfrac{1}{2} < \dfrac{p - p_H}{p} < 1, \end{cases} \qquad (6)$$

where $p > p_H$, $p = \tilde{p} + p'$ is the gas pressure on the lateral surface of the nozzle, p_H is the external pressure, and ξ is the empirical factor. It should be noted that the second of Eqs. (6) takes into account the flow blockage in a pore for $p - p_H > \dfrac{p}{2}$. The formulas for gas inflow velocity in the nozzle are derived from Eqs. (6) by the replacement $p \rightleftarrows p_H$. The change in the thrust of the nozzle is caused by the change in pressure on the porous wall,

$$J_1' = 2\pi \int_{x_1}^{x_2} r p' \sin\alpha\, dx \qquad (7)$$

and by the acceleration (deceleration) of the gas upon its inflow (outflow) due to its interaction with the flow

r

p_H

r_* α

β

0   x_1 x_2 x_{sr} x

Fig. 2. Scheme of the nozzle with a porous insert.
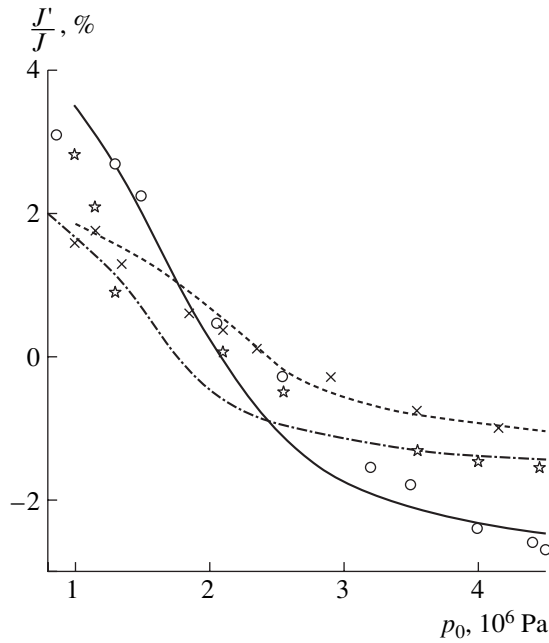
Fig. 3. Relative loss of the specific thrust momentum vs. the nozzle-prechamber pressure.
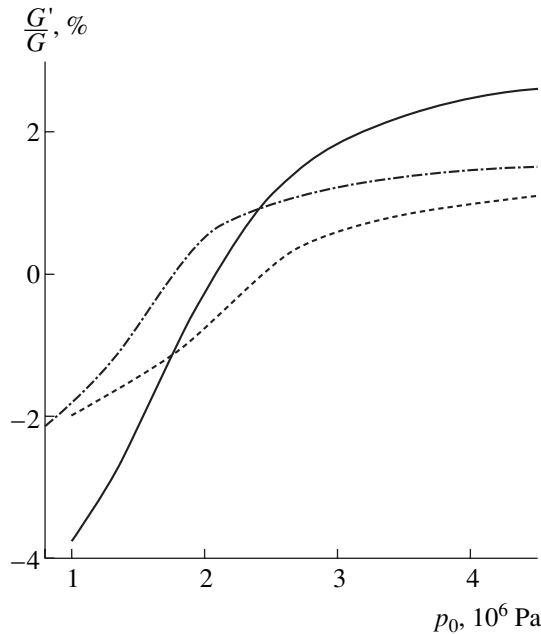
Fig. 4. Relative change in the gas flow rate through the porous section of the nozzle vs. the prechamber pressure.

and nozzle walls,

$$J'_2 = -2\pi \int_{x_1}^{x_2} r\tilde{\rho}\tilde{u}v'\,dx. \qquad (8)$$

The total change in the thrust is the sum of Eqs. (7) and (8), while the relative change in the thrust is found from

the formula

$$\frac{J'}{J} = \frac{J'_1 + J'_2}{J(x_{sr})}, \quad J(x_{sr}) = (\tilde{\rho}\tilde{u}^2 + \tilde{p})S. \qquad (9)$$

On the basis of the mathematical model represented by Eqs. (1)–(9), we performed the calculations under conditions of the experiment. The equation for the supersonic section of the nozzle is

$$r = r_*\left(1 + \frac{x}{r_*}\tan\alpha\right), \qquad (10)$$

where $r_* = 19.2$ mm, $\alpha = 8°$, and the porosity in the section $x_1 < x < x_2$ is equal to $m_1 = 0.18$. Figure 3 shows the relative momentum loss $\frac{J'}{J}$ as a function of the prechamber pressure p_0. Three cases were considered: (i) the entire porous section $x_1 < x < x_2$ is open; (ii) its front part $x_1 < x < x'_2$ is open; and (iii) its rear part $x'_2 < x < x_2$ is open, where $x'_2 = \frac{1}{2}(x_1 + x_2)$. For the case in which the entire porous section from $x_1 = 82$ mm to $x_2 = 130$ mm was open, the solid line is the calculation, and circles show the experimental data. For the case in which the front section 82 mm $< x <$ 106 mm of the porous insert was open, the dash–dotted line corresponds to the calculation, and the asterisks represent the experiment. For the case in which the rear section 106 mm $< x <$ 130 mm of the porous insert was open, the dashed line corresponds to the calculation, and the crosses show the experiment. It is seen that the calculation agrees well with the experiment.

Certain differences between the dash–dotted line and the asterisks (the open front section $x_1 = 82$ mm and $x'_2 = 106$ mm of the porous insert) arise only for $p_0 \approx$ 10 atm, likely because the flow separates at this pressure; therefore, the thrust gain also arises on the closed section for $x > x'_2$. This assumption is supported by the fact that the agreement between the calculation and experiment is good when the entire porous section is open. In this case, the blow results in increasing pressure over the entire section $x_1 < x < x_2$, as in the case of separation. As a result, the experimentally measured momentum gains $\frac{J'}{J}$ for $p_0 \approx 10^6$ Pa nearly coincide for the cases $x_1 < x < x'_2$ and $x_1 < x < x_2$. At high pressures $p_0 > 2 \times 10^6$ Pa, the momentum losses over the entire section $x_1 < x < x_2$ are the sum of losses on the front $x_1 < x < x'_2$ and rear $x'_2 < x < x_2$ porous sections. Figure 4

shows the relative flow-rate change $\dfrac{G'}{G}$ as a function of the prechamber pressure p_0. Here,

$$G' = 2\pi \int_{x_1}^{x_2} r\tilde{\rho}\, v'\, dx, \quad G = \tilde{\rho}\tilde{u}S.$$

The designations are the same as in Fig. 3. It is seen that the dependence of $\dfrac{G'}{G}$ on p_0 is similar (with the opposite sign) to the dependence of $\dfrac{J'}{J}$ on p_0. This similarity is associated with the estimates $J' \sim G'\tilde{u}$ and $J \sim G\tilde{u}$, whence $\dfrac{J'}{J} \sim \dfrac{G'}{G}$.

Similar investigations were performed for the insert fabricated from highly porous cellular carbon with a porosity of approximately 25%. The energy efficiency of this insert appeared to be close to that of the perforated duralumin insert considered above; this is because the change in the thrust and flow rate of the nozzle is determined primarily by porosity, the values of which were close to each other for these two inserts.

It follows from the above results that the effect of the introduction of a porous insert can reach 2–3% of the thrust of the nozzle operating with overexpansion, which creates an additional opportunity for controlling the nozzle thrust.

REFERENCES

1. V. V. Semenov, Tr. MAI (Élektron. Zh.), No. 1 (2000).
2. V. M. Melamed, V. N. Zaikovskii, A. I. Todoschenko, and G. V. Trubacheev, in *Proceedings of the 9th International Conference on the Methods of Aerophysical Research* (ITAM SB RAS, Novosibirsk, 2002), pp. 164–170.
3. G. L. Loĭtsyanskiĭ, *Mechanics of Liquids and Gases* (Nauka, Moscow, 1987; Begell House, New York, 1995).
4. G. L. Grozdovskiĭ, A. A. Nikol'skiĭ, G. P. Svishchev, and G. I. Taganov, *Supersonic Gas Flows in Perforated Boundaries* (Mashinostroenie, Moscow, 1967) [in Russian].

Translated by V. Bukhanov

=== **MECHANICS** ===

Families of Symmetric Periodic Motions of the Euler Problem

V. N. Tkhaĭ

Presented by Academician V.V. Rumyantsev October 6, 2004

FORMULATION OF THE PROBLEM

The motion of a heavy rigid body with a fixed point is described by the Euler–Poisson equations

$$A\dot{p} = (B - C)qr + P(z_0\gamma_2 - y_0\gamma_3),$$

$$B\dot{q} = (C - A)rp + P(x_0\gamma_3 - z_0\gamma_1), \quad (1)$$

$$C\dot{r} = (A - B)pq + P(y_0\gamma_1 - x_0\gamma_2),$$

$$\dot{\gamma}_1 = \gamma_2 r - \gamma_3 q,$$

$$\dot{\gamma}_2 = \gamma_3 p - \gamma_1 r,$$

$$\dot{\gamma}_3 = \gamma_1 q - \gamma_2 p,$$

where A, B, and C are the principal moments of inertia of the body; P is the body weight; x_0, y_0, and z_0 are the center-of-gravity coordinates; $\boldsymbol{\omega} = (p, q, r)$ is the angular velocity; and $\boldsymbol{\gamma} = (\gamma_1, \gamma_2, \gamma_3)$ is the unit vertical upward-directed vector. System (1) has the classical integrals

$$V_1 = Ap^2 + Bq^2 + Cr^2$$
$$+ 2P(x_0\gamma_1 + y_0\gamma_2 + z_0\gamma_3) = 2h(\text{const}),$$

$$V_2 = Ap\gamma_1 + Bq\gamma_2 + Cr\gamma_3 = \sigma(\text{const}),$$

$$V_3 = \gamma_1^2 + \gamma_2^2 + \gamma_3^2 = 1.$$

A distinctive feature of system (1) is that it is invariant under the transformation G: $(\boldsymbol{\omega}, \boldsymbol{\gamma}, t) \longrightarrow (-\boldsymbol{\omega}, \boldsymbol{\gamma}, -t)$. Therefore, system (1) belongs to the class of reversible mechanical systems with a fixed set $M = \{\boldsymbol{\omega}, \boldsymbol{\gamma}: \boldsymbol{\omega} = 0\}$ [1]. The integrals $V_{1,3}$ are symmetric about M, i.e.,

$$V_{1,3}(-p, -q, -r, \gamma_1, \gamma_2, \gamma_3) = V_{1,3}(p, q, r, \gamma_1, \gamma_2, \gamma_3).$$

If the center of gravity is located in the principal plane of the inertia ellipsoid ($y_0 = 0$), then system (1) is also invariant under the change

$$G_y: (p, q, r, \gamma_1, \gamma_2, \gamma_3, t) \longrightarrow (p, -q, r, \gamma_1, -\gamma_2, \gamma_3, -t),$$

that is, it contains the second fixed set

$$M_y = \{p, q, r, \gamma_1, \gamma_2, \gamma_3: q = 0, \gamma_2 = 0\}.$$

In this case, all classical integrals become symmetric:

$$V_j(p, -q, r, \gamma_1, -\gamma_2, \gamma_3) = V_j(p, q, r, \gamma_1, \gamma_2, \gamma_3).$$

The case of $y_0 = 0$ incorporates almost all known exact solutions of the Euler problem, with the exception of those for permanent rotations [2]. In particular, the solutions that are symmetric about the M_y set include the pendulum motions of Mlodzievskiĭ [3], the regular precessions of Grioli [4], etc. It turns out that Grioli solutions belong to the family of symmetric periodic motions (SPMs) [5].

In this work, we demonstrate that SPMs of the Euler problem in the case of $y_0 = 0$ typically form a two-parameter (h and σ) SPM family, which is continuable in the problem parameter. It is also established that a one-parameter (that of h) SPM family exists for a body whose center of gravity is located near the principal plane of the inertia ellipsoid. Finally, results from the study of SPM families for a reversible mechanical system are outlined.

SPM FAMILIES IN A REVERSIBLE MECHANICAL SYSTEM

A reversible mechanical system has the form [6]

$$\dot{u} = U(u, v), \quad \dot{v} = V(u, v),$$
$$u \in R^l, \quad v \in R^n (l \ge n),$$
$$U(u, -v) = -U(u, v), \quad (2)$$
$$V(u, -v) = V(u, v).$$

The set $M_* = \{u, v: v = 0\}$ is called the fixed set of system (2). The first integral $V(u, v) = \text{const}$ satisfying the condition

$$V(u, -v) = V(u, v) \quad (3)$$

is called symmetric.

A motion $u = u(t)$, $v = v(t)$ of system (2) that intersects the fixed set M_* at a certain time t_* is called symmetric. In this motion, $v(t_*) = 0$. The SPM intersects the set M_* at least twice and is specified by periodic

Institute of Control Sciences, Russian Academy of Sciences, Profsoyuznaya ul. 65, Moscow, 117806 Russia
e-mail: tkhai@ipu.rssi.ru

functions of time t, an even function $u = \varphi(t)$ and an odd function $v = \psi(t)$.

Similar definitions are introduced for system (2), periodic in vector v or in some components of vector v.

The equations in variations for the SPMs of system (2) have the form

$$\delta\dot{u} = A_-(t)\delta u + A_+(t)\delta v,$$
$$\delta\dot{v} = B_+(t)\delta u + B_-(t)\delta v, \qquad (4)$$
$$\delta u \in R^l, \quad \delta v \in R^n.$$

Hereafter, plus (minus) subscript refers to even (odd) matrix, vector, and scalar functions, and the periods of functions $A_\pm(t)$ and $B_\pm(t)$ are taken to be equal to 2π.

System (4) consists of $l - n$ simple Lyapunov exponents (LEs). The other LEs are $\pm\kappa$ pairs and are determined by the formulas [5]

$$\kappa = \frac{1}{2\pi}\operatorname{arccosh}\alpha, \quad \det(\delta v^+(2\pi) - \alpha I_n) = 0. \quad (5)$$

Here, the fundamental matrix of solutions of system (4) is written in the form

$$S(t) = \begin{vmatrix} \delta u^+(t) & \delta u^-(t) \\ \delta v^-(t) & \delta v^+(t) \end{vmatrix}, \quad S(0) = I_{l+n},$$

where I_j is the identity j matrix.

The number $k = n - \operatorname{rank} v^-(\pi)$ determines the number of 2π-periodic solutions of system (4) that are symmetric about the fixed set $M_1 = \{\delta u, \delta v : \delta v = 0\}$.

System (4) is reduced to a system with constant coefficients by the change

$$\xi_j = \alpha_{j1}^+\delta u_1 + \alpha_{j2}^+\delta u_2 + \ldots + \alpha_{jl}^+\delta u_l + \beta_{j1}^-\delta v_1$$
$$+ \beta_{j2}^-\delta v_2 + \ldots + \beta_{jl}^-\delta v_n, \quad j = 1, 2, \ldots, l,$$
$$\eta_k = \alpha_{k1}^-\delta u_1 + \alpha_{k2}^-\delta u_2 + \ldots + \alpha_{kl}^-\delta u_l + \beta_{k1}^+\delta v_1 \qquad (6)$$
$$+ \beta_{k2}^+\delta u_2 + \ldots + \beta_{kn}^+\delta v_n, \quad k = 1, 2, \ldots, n,$$

with the transition of $M_1 = \{\delta u, \delta v : \delta v = 0\}$ to a fixed set $\{\xi, \eta : \eta = 0\}$.

In accordance with the Poincaré theorem [7], the equations in variations (4) for a periodic solution of system (2) necessarily have one more LE in addition to the $l - n$ simple zeroth LEs. By virtue of the reversibility of system (4), there are two such zeroth LEs.

For the SPMs of system (2), Eq. (4) admits the periodic solution

$$\delta u = \dot{\varphi}(t), \quad \delta v = \dot{\psi}(t); \quad \dot{\varphi}(-t) = -\dot{\varphi}(t),$$
$$\dot{\psi}(-t) = \dot{\psi}(t). \qquad (7)$$

It is symmetric about the set $M_2 = \{\delta u, \delta v : \delta u = 0\}$. Transformations (6) transform the set M_2 to $\{\xi, \eta : \xi = 0\}$.

The necessary and sufficient conditions for the existence of SPMs are as follows:

$$v(u^0, 0, T) = 0, \qquad (8)$$

where u^0 is an initial point on M and T is the SPM half-period. This equation has the solution $u^0 = u^* = \varphi(0)$, $T = \pi$. Therefore, using the theorem on an implicit function makes it possible to derive the condition

$$\operatorname{rank}\left|\frac{\partial v(u^*, 0, \pi)}{\partial u^0}, \frac{\partial v(u^*, 0, \pi)}{\partial T}\right| = n \qquad (9)$$

of the existence of an $(l - n + 1)$-parameter family.

The partial derivatives in Eq. (9) satisfy the equations in variations (4). Therefore, condition (9) is fulfilled if $k = 0$ or 1 in the matrix $S(\pi)$.

Theorem 1. *Each SPM of the reversible mechanic system given by Eqs.* (2) *belongs to the* $(l - n + 1)$ *parameter family if the equations in variations* (4) *do not have zeroth LEs additional to* $(l - n + 2)$ *LEs.*

The reversible mechanical system given by Eqs. (2) may involve a parameter μ (in the general case, a vector) and admit an SPM for $\mu = 0$. Then, the fulfillment of condition (4) ensures that the SPM family is continuable in the parameter μ.

Theorem 2. *For the parameter-dependent reversible mechanical system given by Eqs.* (2), *each SPM family mentioned in Theorem 1 is continuable in the parameter.*

SPM FAMILIES FOR A HEAVY RIGID BODY WITH A SINGLE FIXED POINT AND THE CENTER OF MASS IN THE PRINCIPAL PLANE OF THE INERTIA ELLIPSOID

For $y_0 = 0$, Euler–Poisson equations (1) can be written in the form of the reversible system given by Eqs. (2) with $l = 4$, $n = 2$, and the vectors $u = (p, q, \gamma_1, \gamma_3)T$ and $v = (q, \gamma_2)^T$, where T means transposition.

Theorem 3. *For $y_0 = 0$, SPM of the Euler problem has two simple zeroth LEs and a pair of zeroth LEs forming a Jordan box, while the two remaining LEs are calculated by means of a construction of only one solution of the Cauchy problem.*

Using Theorem 1 makes it possible to generalize the conclusion [5, 8], which was first made for Grioli precessions, to any SPM.

Theorem 4. *For fixed A, B, C, x_0, and z_0, SPMs of the Euler problem with $y_0 = 0$ typically form a two-parameter (of h and σ) family.*

The two simple LEs are obviously related to the angular momentum integral and the geometric integral. These integrals give the parameter σ. The other parameter h is provided by the energy integral and the corresponding pair of zeroth LEs with the Jordan cell. In

the typical case, there is a pair of nonzeroth LEs. Theorem 2 leads to the following conclusion.

Theorem 5. *In the typical case, the SPM family of the Euler problem with* $y_0 = 0$ *is continuable in the parameter.*

TWO REMARKABLE SPMS OF THE EULER PROBLEM

Regular Grioli Precessions

In 1947, Grioli [4] discovered regular precessions of a body fixed at a point such that the following conditions are fulfilled:

$$x_0^2(B - C) = z_0^2(A - B),$$
$$y_0 = 0, \quad A > B > C. \tag{10}$$

Two remarkable features are characteristic of Grioli precessions. First, they occur for a dynamically asymmetric body that satisfies only conditions (10). Second, the body precesses about an axis inclined by a certain angle β to the vertical rather than about the vertical itself.

It is obvious from the explicit formulas for Grioli solutions [5] that the only possible mechanical motion under the fixation conditions given by Eqs. (10) is precession, which is an SPM. Nevertheless, it follows from Theorem 5 that this SPM belongs to a two-parameter family of h and σ and that this family is continuable in the case that the first of conditions (10) are fulfilled only approximately.

Pendulum Motions of Mlodzievskiĭ

These motions are realized in the problem with no additional constraints on the moments of inertia or the fixation point and include SPMs in the form of both oscillations and rotations:

$$B\dot{q} = P(x_0\gamma_3 - z_0\gamma_1), \quad \dot{\gamma}_1 = -q\gamma_3,$$
$$\dot{\gamma}_3 = q\gamma_1, \tag{11}$$
$$p = r = 0, \quad \gamma_2 = 0.$$

The SPM family given by Eqs. (11) is dependent on a sole parameter: the energy integral h. Lyapunov exponents for solution (11) were calculated in [9]: the typical case is realized. Therefore (cf. Theorem 4), the one-parameter Mlodzievskiĭ family belongs to a two-parameter SPM family incorporating not only plane but also near-plane motions.

It is remarkable that the pendulum oscillations are symmetric simultaneously about two fixed sets, M and M_y, while the rotations are symmetric only about the M_y set. The oscillation symmetry about M makes it possible to apply Theorem 2 to the general case ($y_0 \neq 0$) of the Euler problem with the following result.

Theorem 6. *For the Euler problem in which the center of gravity is located near the principal plane of the inertia ellipsoid, a one-parameter (of h) family of near-plane SPM oscillations always exists.*

REFERENCES

1. V. N. Tkhaĭ, Prikl. Mat. Mekh. **55**, 578 (1991).
2. G. V. Gorr, L. A. Kudryashova, and L. A. Stepanova, *Classical Problems of Rigid Body Dynamics. Development and Current Status* (Naukova Dumka, Kiev, 1978) [in Russian].
3. B. K. Mlodzievskiĭ, Tr. Otd. Fiz. Nauk Ob. Lyubit. Estestozn., Antropol., Étnogr. **7** (1), 46 (1894).
4. G. Grioli, Ann. Mat. Pura Appl. Ser. 4 **26** (3/4), 271 (1947).
5. V. N. Tkhaĭ, Prikl. Mat. Mekh. **64**, 848 (2000).
6. V. N. Tkhaĭ, in *Nonlinear Mechanics* (Fizmatlit, Moscow, 2001), pp. 131–146 [in Russian].
7. H. Poincaré, *New Methods of Celestial Mechanics* (NASA, Washington, D.C., 1967; Nauka, Moscow, 1971).
8. V. N. Tkhaĭ, in *Problems of the Study of Motion Stability and Stabilization* (Vychisl. Tsentr RAN, Moscow, 2000), Part 1, pp. 60–67 [in Russian].
9. V. N. Tkhaĭ and A. L. Shvygin, in *Problems of the Study of Motion Stability and Stabilization* (Vychisl. Tsentr RAN, Moscow, 2000), Part 2, pp. 149–160 [in Russian].

Translated by M. Lebedev

====== **MECHANICS** ======

Structure of a Diffusion-Induced Flow Near a Sphere in a Continuously Stratified Fluid

V. G. Baydulov[1]*, P. V. Matyushin[2], and Yu. D. Chashechkin[1]**

Presented by Academician D.M. Klimov December 1, 2004

Studies of flows induced by diffusion on topography are stimulated by the search for mechanisms of the formation of intense slope winds in the stable stratified atmosphere [1] and flows in the ocean [2, 3]. The analytical solution describing a single-scale steady flow induced by diffusion on an infinite inclined plane has singularities for small slopes [4]. In the exact solution of the problem of flow formation that is induced by diffusion on the infinite inclined plane, the fields of velocity and density are characterized by different scales [5]. The asymptotic solutions of the problem of the formation of two-dimensional diffusion-induced flows on the plane [6], in the channel [7], and in the wedge cavity [8] in the short-time approximation agree with each other and with the solution presented in [5]. However, in the long-time approximation, they do not transform to the steady solution [4] or asymptotic solution [6].

Analysis of flows near three-dimensional obstacles, and particularly near separated lines and points (equator, poles, sharp edges, and brows) is of interest for real applications. The aim of this work is to find asymptotic and numerical solutions of the problem of diffusion-induced flow formation on a three-dimensional obstacle of perfect shape, namely, on an immovable sphere placed in a continuously stratified fluid. It has been shown that the interruption of a molecular flux forms not only the flow on the obstacle surface but also the far field of short transient internal waves.

The standard system of the equations of motion for a linearly stratified incompressible fluid, whose undisturbed density distribution $\rho_0(z)$ is specified by the

salinity profile $S_0(z)$ as $\rho_0\left(1 - \dfrac{z}{\Lambda}\right)$, where z is the vertical coordinate directed upward and Λ is the buoyancy scale, which is related to the buoyancy frequency and period $N = \dfrac{2\pi}{T_b} = \sqrt{\dfrac{g}{\Lambda}}$, consists of the equation of state, the Navier–Stokes equation in the Boussinesq approximation, the continuity equation, and the transport equation for the stratified component (salt or heat):

$$\rho = \rho_0\left(1 - \frac{z}{\Lambda} + S\right),$$

$$\frac{\partial \mathbf{v}}{\partial t} + (\mathbf{v} \cdot \nabla)\mathbf{v} = -\frac{1}{\rho_0}\nabla P + \nu\Delta\mathbf{v} + S\mathbf{g}, \qquad (1)$$

$$\mathrm{div}\,\mathbf{v} = 0,$$

$$\frac{\partial S}{\partial t} + (\mathbf{v} \cdot \nabla)S = \kappa\Delta S + \frac{v_z}{\Lambda}.$$

Here, $\mathbf{g}$ is the gravitational acceleration; S is the salinity perturbation including the salt contraction coefficient; $\mathbf{v} = (v_x, v_y, v_z)$ is the induced velocity; P is the pressure minus the hydrostatic pressure; ν and κ are the kinematic viscosity coefficient and salt diffusion coefficient, respectively; t is time; ∇ is the Hamiltonian operator; and Δ is the Laplacian.

At the initial time $t = 0$, a sphere of diameter d is placed in the fluid without the introduction of mechanical perturbations. The sphere has a solid surface impermeable to salt. The no-slip conditions for velocity and the impermeability condition for salinity are valid on this surface. The initial and boundary conditions have the form

$$\mathbf{v}, S|_{t=0} = 0, \qquad (2)$$

$$\mathbf{v}|_\Sigma = 0, \quad \left.\frac{\partial S}{\partial \mathbf{n}}\right|_\Sigma = \frac{1}{\Lambda}\frac{\partial z}{\partial \mathbf{n}}, \qquad (3)$$

where $\mathbf{n}$ is the outward normal to the sphere surface Σ. All perturbations vanish at infinity:

$$\mathbf{v}, S|_\infty \longrightarrow 0. \qquad (4)$$

[1] *Institute for Problems in Mechanics, Russian Academy of Sciences, pr. Vernadskogo 101, Moscow, 117526 Russia*
  * *e-mail: bayd@ipmnet.ru*
** *e-mail: chakin@ipmnet.ru*

[2] *Institute for Computer Aided Design, Russian Academy of Sciences, Vtoraya Brestskaya ul. 19/18, Moscow, 123056 Russia e-mail: pmatyushin@mail.ru*

The analytical solution of the problem of the formation of three-dimensional flows is constructed using perturbation-theory methods. The inverse buoyancy frequency $t_N = \dfrac{1}{N}$, the viscous boundary-layer thickness $\delta_N = \sqrt{\dfrac{\nu}{N}}$ [5], their ratio $U_N = \dfrac{\delta_N}{t_N}$, $S_N = \dfrac{\delta_N}{\Lambda}$, and $\omega_N = N$ are the natural scales for time, length, velocity, salinity, and the dynamic component of vorticity ($\boldsymbol{\omega} = \mathrm{curl}\,\mathbf{v}$), respectively.

The initial stage of flow formation is characterized by a small parameter τ with the normalization $t = \tau^2 t'$, $r = \tau r'$. Solutions of system (1) are sought in the form of the expansions

$$S + \sum \tau^n S_n, \quad \mathbf{v} = \sum \tau^n \mathbf{v}_n, \quad \boldsymbol{\omega} = \sum \tau^n \boldsymbol{\omega}_n, \quad (5)$$

where the first nonzero terms are retained. Calculations are performed in the spherical coordinate system, $x = r\sin\vartheta\cos\varphi$, $y = r\sin\vartheta\sin\varphi$, $z = r\cos\vartheta$, whose center is at the geometric center of the body. Owing to the symmetry of boundary conditions, the solution is independent of the azimuth angle φ and is written in the form

$$S = S(r, \vartheta, t), \quad \mathbf{v} = U(r, \vartheta, t)\mathbf{e}_\vartheta + V(r, \vartheta, t)\mathbf{e}_r,$$

$$\boldsymbol{\omega} = \omega(r, \vartheta, t)\mathbf{e}_\varphi.$$

The stream function in the spherical coordinate system has the form

$$V = \frac{1}{r^2\sin\vartheta}\frac{\partial\psi}{\partial\vartheta}, \quad U = -\frac{1}{r\sin\vartheta}\frac{\partial\psi}{\partial r},$$

$$\psi = r^2 V(r, t)\sin\vartheta\sin 2\vartheta.$$

After the substitution of expansions (5) into system (1) and the separation of perturbation-theory orders, the first-approximation equations are solved using Laplace transforms. The solutions of the problem for transforms are expressed in terms of the modified Bessel functions of a fraction argument. Asymptotic values corresponding to the short-time approximation are calculated, and then the inverse transforms are performed in the configuration space. The resulting solutions are represented in the dimensionless form

$$S_1 = -2\varepsilon\sqrt{t}\frac{R}{r}i\,\mathrm{erfc}\left(\frac{r-R}{2\varepsilon\sqrt{t}}\right)\cos\vartheta,$$

$$U_1 = -4\frac{(\varepsilon\sqrt{t})^3}{1-\varepsilon^2}\frac{R}{r}\left[i^3\mathrm{erfc}\left(\frac{r-R}{2\sqrt{t}}\right) - i^3\mathrm{erfc}\left(\frac{r-R}{2\varepsilon\sqrt{t}}\right)\right]\sin 2\vartheta,$$

$$V_1 = -\frac{8}{R}\frac{\varepsilon^3 t^2}{1-\varepsilon^2}\left\{\left(\frac{R}{r}\right)^2\left[i^4\mathrm{erfc}\left(\frac{r-R}{2\sqrt{t}}\right)\right.\right. \quad (6)$$

$$\left.\left. -\varepsilon\cdot i^4\mathrm{erfc}\left(\frac{r-R}{2\varepsilon\sqrt{t}}\right)\right] - \alpha\left(\frac{R}{t}\right)^4\right\}(1 + 3\cos 2\vartheta),$$

$$\omega_1 = 2\frac{\varepsilon^2 t}{1-\varepsilon^2}\frac{R}{r}\left\{\varepsilon\cdot i^2\mathrm{erfc}\left(\frac{r-R}{2\sqrt{t}}\right) - i^2\mathrm{erfc}\left(\frac{r-R}{2\varepsilon\sqrt{t}}\right)\right\}\sin 2\vartheta,$$

where $\varepsilon^2 = \mathrm{Sc}^{-1} = \dfrac{\kappa}{\nu}$, $R = \dfrac{d}{2\delta_N}$, and $\alpha = \dfrac{1}{32}(1 - \varepsilon)$.

The arising flow is characterized by different spatial variation scales for the field of velocity (thickness δ_N), salinity, and vorticity (thickness $\varepsilon\delta_N$). The angular distribution of flows is described by Legendre polynomials. The outer flow is directed to the sphere in the equatorial plane, moves toward the poles along meridians, is accumulated on the poles, and then flows as an axisymmetric plume. Solution (6) is analytic with respect to all physical parameters and is local-uniformly transformed to the solution of two-dimensional (cylinder) and one-dimensional (inclined plane) problems in the limit $R \longrightarrow \infty$ and for the appropriate choice of the coordinate system of tangent planes.

The further development of the flow is analyzed numerically. To make equations dimensionless, we take the sphere diameter as the length scale and specify the characteristic velocity U_N. In this case, the traditional numbers such as Reynolds number $\mathrm{Re} = \dfrac{U_N d}{\nu}$, Froude number $\mathrm{Fr} = \dfrac{U_N}{Nd}$, Schmidt number $\mathrm{Sc} = \dfrac{\nu}{\kappa}$, and scale ratio $C = \dfrac{\Lambda}{d}$ appear in system (1). System (1) is solved using the SMIF-MERANZH method of splitting into physical factors with an explicit hybrid finite difference scheme to approximate the convective terms of the equations. This method ensures a second order approximation with respect to the spatial variables, minimum scheme viscosity and dispersion, and monotonicity [9, 10]. The Poisson equation for pressure is solved using the conjugate gradient method with diagonal preconditioning. To estimate scale factors and complete further comparisons with experiments, we take $d_1 = 2$ cm, $d_2 = 4$ cm, $\Lambda = 10$ m, $N = 0.991$ s^{-1}, and $U_N = 1$ mm/s.

The calculations were performed with a software package to accomplish a direct numerical simulation of spatial separation flows for a viscous incompressible linearly stratified fluid near the sphere. The calculations were performed on spherical grid $N \times M \times L$, where N, M, and L are the numbers of cells in the finite-difference grid in the directions of R, ϑ, and φ, respectively. Since the problem is axisymmetric about the vertical direction, the number of cells in the finite-difference grid in the azimuthal direction was taken to equal unity (i.e., $L = 1$). The outer boundary is located at a distance of eight diameters from the sphere. To resolve the velocity

(a)

(b)
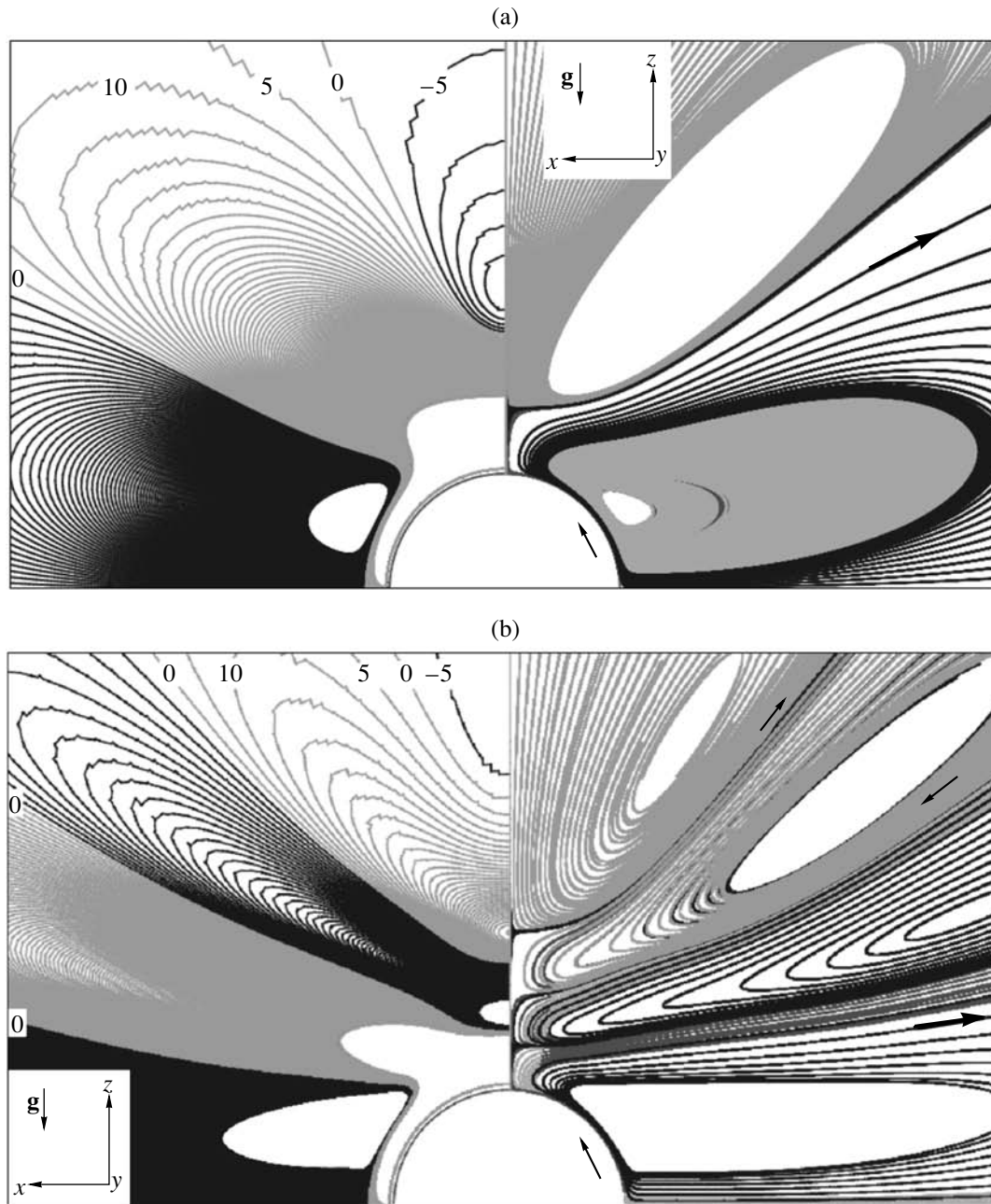
Fig. 1. Pattern of diffusion-induced flow formation on the small immovable sphere (diameter $d = 2$ cm) in a continuously stratified fluid with a buoyancy period of $T_b = 6.34$ s at $t = $ (a) T_b and (b) $2T_b$. The left and right panels show contours of perturbations of salinity ($S \times 10^{12}$) and streamlines, respectively. The $480 \times 480 \times 1$ grid was used in calculations, and $B = 200$.

boundary layer with a scale of $\delta = \sqrt{\dfrac{2}{\text{Re}}}$, the grid is con-centrated near the sphere surface so that B cells with sizes $\delta_1 = 0.316$ and $\delta_2 = 0.224$ can be placed in the boundary layer in the radial direction. The minimum size of the cell of the calculation grid is determined by the expression $h_{min} = \dfrac{\delta}{B}$. The calculations were per-formed for small ($d < L_v$) and large ($d > L_v$) diameters,

where $L_v = \dfrac{\sqrt[3]{g\nu}}{N}$ is the viscous wave scale, which is equal to 2.16 cm for $T_b = 6.34$ s.

Figure 1 shows the pattern of diffusion-induced flow near the small sphere in the phase of the cellular struc-ture formation for two times $t = T_b$ and $2T_b$. For com-pleteness of description, the distributions of the follow-ing two physical quantities are given: perturbations of salinity (in the left panels of the figure) and stream
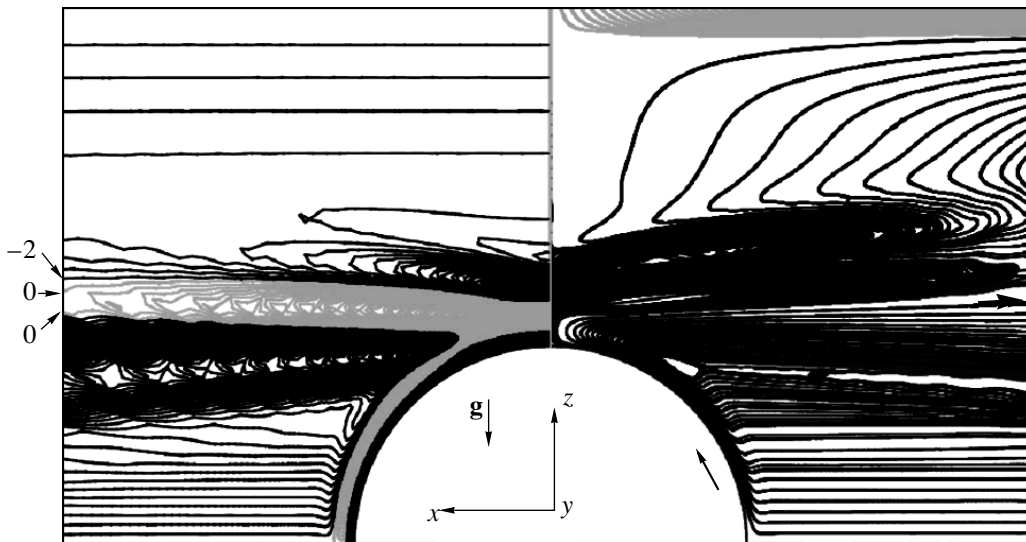
Fig. 2. Steady diffusion-induced flow near the small immovable sphere (diameter $d = 2$ cm, $T_b = 6.34$ s, $t = 1662T_b$). The left and right panels show contours of perturbations of salinity ($S \times 10^8$) and streamlines, respectively. The $160 \times 60 \times 1$ grid was used in calculations, and $B = 50$.

functions (in the right panels of the figure). Since the flow pattern is antisymmetric with respect to the horizontal equatorial plane and symmetric with respect to the vertical axis, the results are given only for the central cross-section and one quadrant. Two cells with opposite directions of vorticities are present in the streamline distributions in Fig. 1a. In addition to two formed cells, a grown cell is observed near the vertical axis in the pattern of salinity perturbations.

A base cell, whose size is determined by the sizes of the body, is located near the body surface. The direction of motion in this cell is fixed: the fluid flows in the equatorial plane, moves over the sphere surface toward the poles or sinks in the lower half-space, and then flows out. With time, the upper boundary of the cell plateaus, and velocity within the cell increases slowly.

The second cell with the opposite rotation direction is situated over the base cell, being separated by the zero streamline. At $t = T_b$, the second cell occupies the upper half of the quadrant. It is then flattened under the action of the newly formed cells.

The structure of the salinity perturbation field that is shown in the left panels of Fig. 1 is similar to the pattern of the streamlines. However, in addition to the two complete cells at $t = T_b$, it contains a third cell formed near the vertical axis. The separating cells of the zero-level line for perturbations of salinity and velocity are located at different levels and intersect the Oz axis at different distances from the body center: $z = 1.03$ and 2.21 cm for salinity and $z = 1.56$ cm for velocity. This difference in the position of zero lines is characteristic of wave processes in stratified media.

With time, the number of cells increases noticeably and their shape changes. At $t = 2T_b$, four complete cells

are observed in the velocity field, and four and a half cells, in the salinity field (Fig. 1b). In this case, the outer boundary of the base cell far from the body is shifted to the equatorial plane, and its upper boundary is flattened. Circulation in each cell is conserved over time. Owing to an increase in the number of cells, their arrangement slowly changes with time. The amplitude of perturbations decreases as the number of cells increases.

The number of pairs of convective cells increases further in proportion to the number of buoyancy periods (six cells for three buoyancy periods, eight cells for four periods, etc.), and their vertical size decreases correspondingly. The first cells adjacent to the base cell are situated at a small angle to the horizon.

At long times, the sizes and arrangement of cells are stabilized, and only the base cell and two thin adjacent cells with a thickness of $\delta_{\rho, 1} = 2.2$ mm are separated both in the salinity field and streamline pattern (Fig. 2). At long times, the zero-level lines for salinity perturbations ($z = 1.09$, 1.23, and 1.42 cm) do not coincide with the zero streamlines ($z = 1.17$, 1.32, 1.50, and 2.59 cm). The indicated features testify to the dynamic pattern of perturbations induced by such a weak source as the sudden interruption of molecular diffusion on the surface of an introduced obstacle. As a whole, the character and dynamics of changes in the structure make it possible to classify secondary cells as transient internal waves [11], which arise due not only to mechanical perturbation factors but also to thermodynamic perturbation factors.

As the sphere diameter for $d > L_v$ increases, the height of the base cell increases, and it is adjoined only by two slightly larger secondary cells (with a height of $\delta_{\rho, 2} = 3.2$ mm, Fig. 3). The zero-level lines are located
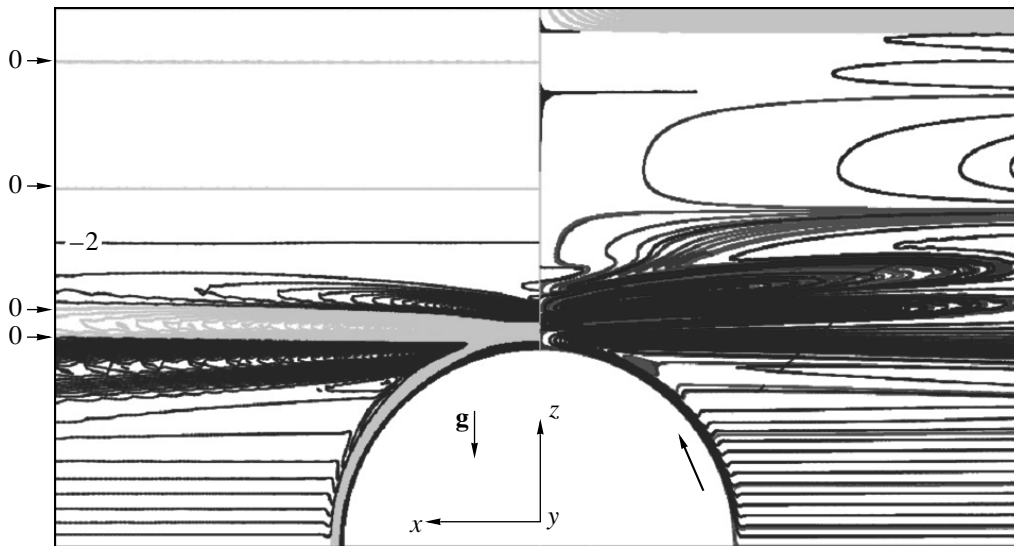
Fig. 3. Steady diffusion-induced flow near the large immovable sphere (diameter $d = 4$ cm, $T_b = 6.34$ s, $t = 1075 T_b$). The left and right panels show contours of perturbations of salinity ($S \times 10^8$) and streamlines, respectively. The $320 \times 120 \times 1$ grid was used in calculations, and $B = 100$.

at $z = 2.09$, 2.28, 2.48, and 2.58 cm for salinity perturbations and at $z = 2.19$, 2.38, 2.56, 2.67, 2.83, and 3.43 cm for velocity. Thus, changes in the size of the body slightly affect the height of secondary cells, which effect is determined by stratification and dissipative parameters of the medium. The patterns calculated for flows are stable under changes in the grid parameters.

Despite certain similarities, there are fundamental differences in the patterns of a cellular flow induced by diffusion near an immovable obstacle and multicomponent convection near a compact source [12]. Circulation in wave cells is sign alternating, and the scales of the regions of changes in velocity and salinity at boundaries are close to each other. All convective cells rotate in one direction, and high-gradient interfaces with different scales of changes in velocity and density are situated at their boundaries [12].

The pattern calculated for large times agrees with the results of shadow visualization of flows near immovable obstacles in laboratory experiments [13]. Fine structure of salinity and temperature fields are usually detected near mountain peaks in the atmosphere and ocean.

REFERENCES

1. J. Oerlemans and B. Grisogono, Tellus **54**, 440 (2002).
2. L. Thompson and G. C. Johnson, Deep-Sea Res. **46** (2), 193 (1996).
3. C. Garrett, Annu. Rev. Fluid Mech. **25**, 291 (1993).
4. L. Prandtl, *Führer Durch Die Strömungslehre* (Auflage, Braunschweig, 1942; Inostrannaya Literatura, Moscow, 1949).
5. A. V. Kistovich and Yu. D. Chashechkin, Dokl. Akad. Nauk SSSR **325** (4), 833 (1992).
6. P. F. Linden and J. E. Weber, J. Fluid Mech. **81**, 757 (1977).
7. V. G. Baĭdulov and Yu. D. Chashechkin, Izv. Akad. Nauk: Fiz. Atm. Okeana **32** (6), 818 (1996).
8. A. V. Kistovich and Yu. D. Chashechkin, Prikl. Mat. Mekh. **62**, 803 (1998).
9. O. M. Belotserkovskiĭ, V. A. Gushchin, and V. N. Kon'shin, Zh. Vychisl. Mat. Mat. Fiz. **27**, 594 (1987) [Comput. Math. Math. Phys. **27**, 594 (1987)].
10. V. A. Gushchin and P. V. Matyushin, Zh. Vychisl. Mat. Mat. Fiz. **37**, 1122 (1997) [Comput. Math. Math. Phys. **37**, 1086 (1997)].
11. Yu. D. Chashechkin and S. A. Makarov, Dokl. Akad. Nauk SSSR **276** (5), 1246 (1984).
12. V. S. Belyaev and Yu. D. Chashechkin, Izv. Akad. Nauk SSSR, Mekh. Zhidk. Gaza, No. 2, 27 (1989).
13. Yu. D. Chashechkin, J. Visualization **1** (4), 345 (1999).

Translated by R. Tyapaev

============================ **MECHANICS** ============================

Initial Stage of the Generation of Dam-Break Waves

V. I. Bukreev and A. V. Gusev

Presented by Academician O.F. Vasil'ev November 10, 2004

Self-similar solutions to the problem of dam break were analytically obtained in the first approximation of shallow-water theory. These solutions have certain analogues in one-dimensional gas dynamics. The case of a rectangular channel with a flat bed was first analyzed in [1]. Recently, analytical self-similar solutions were found using the same approach employed for the channel with an uneven bed [2–4]. For applied problems, numerical calculations based on the Saint-Venant equations were successfully used with actual river geometry, slope of the bed, and hydraulic resistance [5, 6]. Currently, numerical calculations for waves of various shapes under shallow-water conditions are performed using rather complicated mathematics involving the Euler and Navier–Stokes equations. Waves generated in the course of dam break are quite suitable for testing the results of such computations [7].

According to the classical theory, the self-similar conditions in the flow under discussion are established instantaneously. However, actual processes are characterized by a certain delay. Advanced modern mathematical techniques enable one to treat the problems with rather sophisticated initial and boundary conditions. In order to compare different approaches, it is useful to have experimental data on the initial stage of hydrodynamic processes following the fast opening of the sluice-gate, which forms the initial water level difference $\Delta H = H_1 - H_2$ in the rectangular flume with a smooth horizontal bed. Here, H_1 and H_2 are the initial depths in headwater and tailwater, respectively. These processes differ significantly for the cases of dry and irrigated beds in the tailwater [1, 8]. In this paper, we demonstrate a set of photos for both cases. One photo for the dry bed was presented in [8]. A series of video frames for the irrigated bed was shown in [9].

The experiments were performed in a rectangular flume 20 cm in width. The flat plexiglas gate 1 cm thick was removed upward using a lever. The law of motion of the gate was recorded with a slide-wire gauge. This law strongly agrees with the linear function. The time

interval Δt from the onset of gate motion until the time when its lower edge came out of the water was equal to 0.05 s. Hydrodynamic processes were studied using photo shooting and wave meters. Water in the headwater was colored by ink. Wave meters were used to determine the speed of the longitudinal displacement of characteristic points in the profile of the water wave.

Figure 1 shows video frames for the case of the dry bed in the tailwater ($H_2 = 0$) as obtained at various times beginning with the onset of gate motion. In Fig. 1a, the gate has not yet emerged from the water. The main part of the released water still forms a nearly vertical front. The free surface in the headwater is almost horizontal. Only weak ripples propagate along it. The outflow to the tailwater occurs only in a relatively thin near-bed layer. The high vertical front remains, slightly displacing toward the headwater, even for some time after the complete removal of the gate (Fig. 1b). Seemingly, the vertical front should break soon after that, but this was not the case (Figs. 1c and 1d).

It is well known [7–10] that the classical analytical solution [1] for the case of the dry bed poorly agrees with both experimental data and calculations based on more sophisticated mathematical models. According to the classical theory, the constant critical depth $h_* = 4H_1/9$ is instantaneously established in the channel cross-section, where the gate was located, and the free-surface profile corresponds to a monotonic downstream decrease in depth. The profile convexity is directed toward the bed. In the framework of this theory, the absolute value of wave propagation speed is equal to limiting speed $c_* = \sqrt{gH_1}$ of the propagation of infinitesimal perturbations in the headwater and to $2c_*$ in the tailwater. In the experiments under discussion, it was found by wave meters that depth h_* was established only after time interval $t_0 = 0.35$ s $\left(\text{in dimensionless units, after } \tau_0 = t_0 \sqrt{\dfrac{g}{H_1}} = 2.4\right)$. The measured speed of the propagation of perturbations exceeds c_* in the headwater and is lower than $2c_*$ in the tailwater [10].

Lavrent'ev Institute of Hydrodynamics, Siberian Division,
Russian Academy of Sciences,
pr. Akademika Lavrent'eva 15, Novosibirsk, 630090 Russia

Fig. 1. Profiles of the free surface in the case of the dry bed in the tailwater, $H_1 = 20.5$ cm, $H_2 = 0$, and $t =$ (a) 0.03, (b) 0.05, (c) 0.18, and (d) 0.46 s. The vertical dashed line is the initial position of the gate.

The video images presented in Fig. 1 demonstrate that deviations from the classical theory are most significant at the initial stage. In contrast to that theory, the measured free-surface profile is convex upstream of a certain point. There are several inflections downstream of this point. The most significant feature of the actual process is that a hydraulic jump with the roller is formed in the tailwater, whereas the theory predicts a
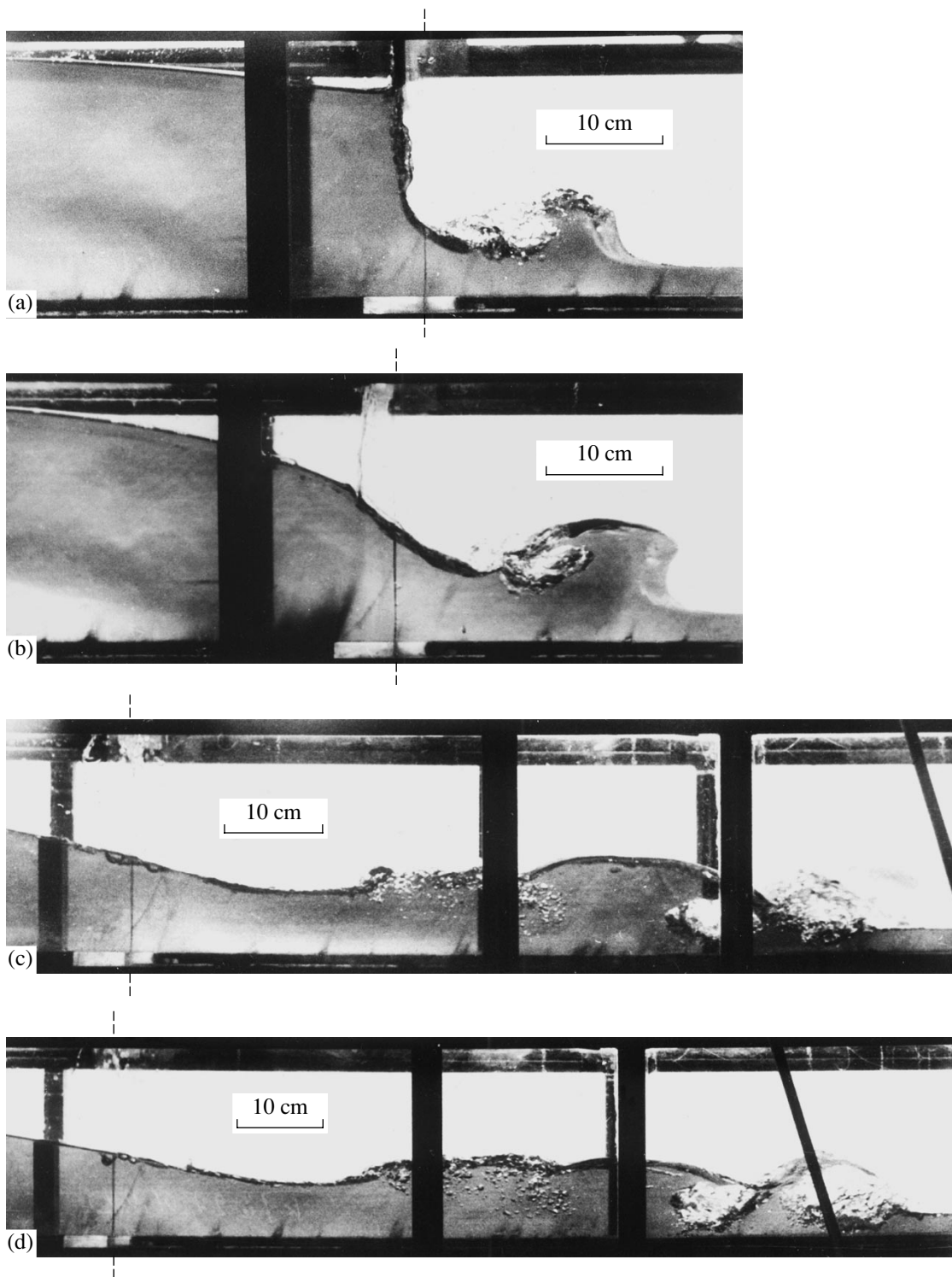
Fig. 2. Same as in Fig. 1 but for the irrigated bed in the tailwater, $H_1 = 20.5$ cm, $H_2 = 2$ cm, $t =$ (a) 0.08, (b) 0.20, (c) 0.40, and (d) 0.50 s.

monotonic vanishing of depth in this region. Note that a thin "tongue" ahead of the hydraulic jump was observed in the experiment [10]. Numerical simulations based on five theoretical models were reported in [7]. The results of these simulations significantly differ from each other. Qualitatively, the model that is based on the Navier–Stokes equations provides the best agreement with the actual experiment. Only this model reproduces the tongue ahead of the hydraulic jump.

The images for the initially irrigated tailwater are presented in Fig. 2. In this case, the classical theory [1] describes quite well the heights and propagation speeds of the hydraulic jumps in the tailwater after some initial stage [10]. According to the theory [1] and experiment [10], there exists a value ($H_{2*} \simeq 0.138H_1$) such that the processes in the tailwater at $H_2 \leq H_{2*}$ do not affect the waves in the headwater. The video images presented in Fig. 2 were obtained at $H_2 \leq H_{2*}$. Comparison of these images with the images shown in Fig. 1 demonstrates that the scenario described is also characteristic of the initial stage and that the processes in the headwater are identical both for the dry and irrigated beds. At the same time, the flow patterns in the tailwater differ significantly for these two cases.

The images in Fig. 2 demonstrate that a vertical jet is formed due to collision between moving and still water. When the jet returns to the main flow, the water continuity is broken and air-filled cavities are formed. At very small but nonzero H_2/H_1 values, the jet propagates in a horizontal direction [7]. When the H_2/H_1 ratio exceeds some critical value, undulations appear instead of the vertical jet. It is well known that the steady flow from under the partially opened gate is accompanied by so-called flow compression [11]. Similar compression is observed in Figs. 2c and 2d, and it lasts for a long time [10].

It is impossible to describe the jet and undulations using the first approximation of shallow-water theory. The basic equations of shallow-water theory were derived under the assumption of an irrotational flow. However, a significant vorticity is generated at the initial stage of a flow accompanying dam break. In particular, this property can explain the formation of the vertical front and other features of the initial stage. In an open system, vorticity may be conserved for an infinitely long time. In the system under study, it decays rather slowly as a consequence of friction at the channel bed and walls. Therefore, "memory" about the initial stage is retained for a long time.

The Navier–Stokes equations reproduce vorticity. However, these equations do not take into account the breakdown of water continuousness occurring in the roller of the hydraulic jump and during the decay of the vertical jet. To describe the real processes, it is appropriate to use mathematical models with free parameters whose variation in the course of calculations provides good agreement with experimental data.

REFERENCES

1. J. J. Stoker, *Water Waves: The Mathematical Theory with Applications* (Interscience, New York, 1957; Inostrannaya Literatura, Moscow, 1959).
2. A. A. Atavin and O. F. Vasil'ev, in *Proceedings of Symposium "Hydraulic and Hydrologic Aspects of the Reliability and Safety of Waterworks"* (VNIIG, St. Petersburg, 2002), p. 121 [in Russian].
3. V. V. Ostapenko, Prikl. Mekh. Tekh. Fiz. **44** (6), 107 (2003).
4. V. I. Bukreev, A. V. Gusev, and V. V. Ostapenko, Izv. Akad. Nauk, Ser. Mekh. Zhidk. Gaza, No. 6, 72 (2003).
5. A. A. Atavin, O. F. Vasil'ev, and A. P. Yanenko, *Hydrodynamic Processes in Navigation Structures* (Nauka, Novosibirsk, 1993) [in Russian].
6. O. F. Vasil'ev, Vodn. Resur. **26** (5), 600 (1999).
7. G. Colicchio, A. Colagrossi, M. Greco, and M. Landrini, Shiffstechnik **49** (3), 95 (2002).
8. R. F. Dressler, Int. Assoc. Sci. Hydrol. **3** (38), 319 (1954).
9. P. K. Stansby, A. Chegini, and T. C. D. Barnes, J. Fluid Mech. **374**, 407 (1998).
10. V. I. Bukreev, A. V. Gusev, A. A. Malysheva, and I. A. Malysheva, Izv. Akad. Nauk, Ser. Mekh. Zhidk. Gaza, No. 5, 143 (2004).
11. P. G. Kiselev, *Handbook for Hydraulic Calculations* (Gosénergoizdat, Moscow, 1957) [in Russian].

Translated by K. Kugel

========= **MECHANICS** =========

Acceleration Waves in Micropolar Elastic Media

V. A. Eremeyev

Presented by Academician V.A. Babeshko December 1, 2004

Received December 14, 2004

For nonlinearly elastic micropolar media, a condition of the existence of weak discontinuous solutions of equations of motion has been obtained. For these solutions, which constitute acceleration waves, the continuity of the second derivatives of displacement and microrotation fields is broken on certain singular surfaces. In the framework of the micropolar-medium model (Cosserat continuum), each particle has the degrees of freedom of an absolutely rigid body, their rotation interaction may be taken into account, and couple stresses exist in addition to standard stresses. The Cosserat model is used to describe granulated, powder-like, and loose media, as well as polycrystalline bodies, composites, and nanostructures. It is also applied to develop non-classical models of thin-walled constructions: bars, plates, and shells.

An analogue of the Fresnel–Hadamard–Duhem theorem on the existence of acoustic axes and real acoustic numbers has been proved. It has been shown that the condition of the existence of an acceleration wave is equivalent to the requirement of a strong ellipticity of equilibrium equations, as in the case of simple materials that are free of couple stresses.

BASIC RELATIONS

The equations of motion of the micropolar medium (Cosserat continuum), which present the balance of the momentum and angular momentum for an arbitrary body part, have the form [1–11]

$$\operatorname{div}\mathbf{T} + \rho\mathbf{f} = \rho\frac{d\mathbf{v}}{dt},$$

$$\operatorname{div}\mathbf{M} + (\mathbf{F}^T \cdot \mathbf{T})_\times + \rho\mathbf{m} = \rho\gamma\frac{d\boldsymbol{\omega}}{dt}. \tag{1}$$

Here, $\mathbf{T}$ and $\mathbf{M}$ are the Piola tensors of stresses and couple stresses, respectively; $\mathbf{F} = \operatorname{grad}\mathbf{R}$ is the strain gradient; div and grad are, respectively, the divergence and gradient operators in the Lagrangian coordinates; ρ is

_____

Faculty of Mechanics and Mathematics,
Rostov State University, ul. Zorge 5,
Rostov-on-Don, 344104 Russia
e-mail: eremeyev@math.rsu.ru

the medium density in the reference configuration; $\mathbf{f}$ and $\mathbf{m}$ are the mass force and mass moment, respectively; $\rho\gamma$ is the scalar measure of the rotation inertia of continuum particles; $\mathbf{v} = \dfrac{d\mathbf{R}}{dt}$ is the particle velocity; the radius-vector $\mathbf{R}(t)$ specifies the position of particles of the micropolar medium at time t; the orthogonal microrotation tensor $\mathbf{H}(t)$ determines its orientation; $\boldsymbol{\omega} = \left(\dfrac{d\mathbf{H}}{dt} \cdot \mathbf{H}^T\right)_\times$ is the angular velocity; and $\mathbf{T}_\times$ represents the vector invariant of the second-rank tensor $\mathbf{T}$ [12].

The constitutive equations of the micropolar elastic medium can be written in terms of the specific (per unit volume in the reference configuration) potential energy of deformation $W = W(\mathbf{E}, \mathbf{K})$ as [10]

$$\mathbf{T} = W_{,\mathbf{E}} \cdot \mathbf{H}, \quad \mathbf{M} = W_{,\mathbf{K}} \cdot \mathbf{H},$$

$$\mathbf{E} = \mathbf{F} \cdot \mathbf{H}^T, \quad \mathbf{K} \times \mathbf{I} = -(\operatorname{grad}\mathbf{H}) \cdot \mathbf{H}^T, \tag{2}$$

where $\mathbf{E}$ and $\mathbf{K}$ are the measures of the metric and bending deformations, respectively; $\mathbf{I}$ is the unit tensor; W is assumed to be twice continuously differentiable; and

$$W_{,\mathbf{E}} = \frac{\partial W}{\partial \mathbf{E}}, \; W_{,\mathbf{K}} = \frac{\partial W}{\partial \mathbf{K}}.$$

PROPAGATION OF WEAK DISCONTINUITIES (ACCELERATION WAVES)

We consider a medium motion that may be accompanied by a break in the continuity of kinematic and dynamic quantities on a certain smooth surface $S(t)$, which is called *singular*. We assume that the limiting values of these quantities exist on S and that they are generally different on the opposite sides of S. The jump of $\boldsymbol{\Psi}$ on S is denoted as

$$[\![\boldsymbol{\Psi}]\!] = \boldsymbol{\Psi}^+ - \boldsymbol{\Psi}^-.$$

The acceleration wave (weak-discontinuity wave or second-order singular surface) is a moving singular surface on which the second derivatives (with respect to the spatial coordinates and time) of the radius-vector $\mathbf{R}$ and microrotation tensor $\mathbf{H}$ are discontinuous, while the

quantities themselves and their first derivatives are continuous; i.e., the equalities

$$[\![\mathbf{F}]\!] = \mathbf{0}, \quad [\![\mathrm{grad}\mathbf{H}]\!] = \mathbf{0}, \quad [\![\mathbf{v}]\!] = \mathbf{0}, \quad [\![\boldsymbol{\omega}]\!] = \mathbf{0} \quad (3)$$

are valid on S. According to Eqs. (3), deformation measures $\mathbf{E}$ and $\mathbf{K}$ are continuous near S, and, in view of constitutive equations (2), jumps of the tensors $\mathbf{T}$ and $\mathbf{M}$ are absent.

The application of the Maxwell theorem [13] to continuous fields of velocities $\mathbf{v}$ and $\boldsymbol{\omega}$, stresses, and couple stresses $\mathbf{T}$ and $\mathbf{M}$ yields a system of equations that relate the jumps of their derivatives with respect to the spatial coordinates and time:

$$[\![\dot{\mathbf{v}}]\!] = -V\mathbf{a}, \quad [\![\mathrm{grad}\mathbf{v}]\!] = \mathbf{n} \otimes \mathbf{a}, \quad [\![\dot{\boldsymbol{\omega}}]\!] = -V\mathbf{b},$$

$$[\![\mathrm{grad}\boldsymbol{\omega}]\!] = \mathbf{n} \otimes \mathbf{b}, \quad (4)$$

$$V[\![\mathrm{div}\mathbf{T}]\!] = -\mathbf{n} \cdot [\![\dot{\mathbf{T}}]\!], \quad V[\![\mathrm{div}\mathbf{M}]\!] = -\mathbf{n} \cdot [\![\dot{\mathbf{M}}]\!].$$

Here, $\mathbf{a}$ and $\mathbf{b}$ are the vector amplitudes for the jumps of the linear and angular accelerations, $\mathbf{n}$ is the unit normal vector to S, and V is the velocity of the surface S in the direction $\mathbf{n}$ [13]. If mass forces and moments are continuous, the relations

$$[\![\mathrm{div}\mathbf{T}]\!] = \rho[\![\dot{\mathbf{v}}]\!], \quad [\![\mathrm{div}\mathbf{M}]\!] = \rho\gamma[\![\dot{\boldsymbol{\omega}}]\!]$$

follow from the equations of motion (1). Differentiating constitutive equations (2) and using Eqs. (4), we express these relations only in terms of the vector amplitudes $\mathbf{a}$ and $\mathbf{b}$:

$$\mathbf{n} \cdot W_{,\mathbf{EE}} \cdots (\mathbf{H} \cdot \mathbf{a} \otimes \mathbf{n}) + \mathbf{n} \cdot W_{,\mathbf{EK}} \cdots (\mathbf{H} \cdot \mathbf{b} \otimes \mathbf{n})$$
$$= \rho V^2 \mathbf{a} \cdot \mathbf{H}^T,$$

$$\mathbf{n} \cdot W_{,\mathbf{KE}} \cdots (\mathbf{H} \cdot \mathbf{a} \otimes \mathbf{n}) + \mathbf{n} \cdot W_{,\mathbf{KK}} \cdots (\mathbf{H} \cdot \mathbf{b} \otimes \mathbf{n})$$
$$= \rho\gamma V^2 \mathbf{b} \cdot \mathbf{H}^T.$$

These relations can be written in a more compact form using the matrix notation

$$\mathbb{A}(\mathbf{n}) \cdot \boldsymbol{\xi} = \rho V^2 \mathbb{B} \cdot \boldsymbol{\xi}, \quad (5)$$

where $\boldsymbol{\xi} = (\mathbf{a}', \mathbf{b}') \in \mathbb{R}^6$, $\mathbf{a}' = \mathbf{a} \cdot \mathbf{H}^T$, $\mathbf{b}' = \mathbf{b} \cdot \mathbf{H}^T$, $\mathbb{A}$ and $\mathbb{B}$ are the matrices with tensor elements

$$\mathbb{A}(\mathbf{n}) \equiv \begin{bmatrix} W_{,\mathbf{EE}}\{\mathbf{n}\} & W_{,\mathbf{EK}}\{\mathbf{n}\} \\ W_{,\mathbf{KE}}\{\mathbf{n}\} & W_{,\mathbf{KK}}\{\mathbf{n}\} \end{bmatrix}, \quad \mathbb{B} \equiv \rho V^2 \begin{bmatrix} \mathbf{I} & \mathbf{0} \\ \mathbf{0} & \gamma\mathbf{I} \end{bmatrix}$$

and the notation $\mathbf{G}\{\mathbf{n}\} \equiv G_{klmn}n_k n_m \mathbf{i}_l \otimes \mathbf{i}_n$ is introduced for any fourth-rank tensor $\mathbf{G}$ and any vector $\mathbf{n}$ that are represented in terms of their decompositions in the arbitrary Cartesian basis $\mathbf{i}_k$, $k = 1, 2, 3$.

Thus, the problem of acceleration wave propagation in the micropolar medium has been reduced to the spectral problem given by Eq. (5). Owing to the existence of the potential-energy function W, $\mathbb{A}(\mathbf{n})$ is symmetric. This property enables one to formulate an analogue of

the Fresnel–Hadamard–Duhem theorem for micropolar media.

Theorem 1. *The squares of the velocities of second-order singular surfaces (acceleration waves) in the micropolar elastic medium are real for arbitrary propagation directions specified by the vector* $\mathbf{n}$.

The positive definiteness of $\mathbb{A}(\mathbf{n})$, which is both necessary and sufficient for the wave velocity V to be real, i.e., the inequality

$$\boldsymbol{\xi} \cdot \mathbb{A}(\mathbf{n}) \cdot \boldsymbol{\xi} > 0,$$
$$\forall \mathbf{n} \in \mathbb{R}^3, \quad \mathbf{n} \neq \mathbf{0}, \quad \forall \boldsymbol{\xi} \in \mathbb{R}^6, \quad \boldsymbol{\xi} \neq \mathbf{0}, \quad (6)$$

is an additional constraint imposed on constitutive relationships (2).

Following [7], one can prove Theorem 2.

Theorem 2. *Condition* (6) *for the existence of the acceleration wave in the micropolar elastic medium is equivalent the condition of strong ellipticity of the equilibrium equation.*

Weak inequality (6) is an analogue of the Hadamard inequality from the spatial theory of elasticity [12, 13]. As in the case of simple materials, a break in inequality (6) means the possibility of existing nonsmooth solutions of the equilibrium equations.

As an example, we consider the equation of state of a physically linear micropolar medium [7]

$$W = W_1(\mathbf{E}) + W_2(\mathbf{K}). \quad (7)$$

Here,

$$W_1(\mathbf{E}) = \alpha_1 \mathrm{tr}((\mathbf{E} - \mathbf{I}) \cdot (\mathbf{E} - \mathbf{I})^T)$$
$$+ \alpha_2 \mathrm{tr}((\mathbf{E} - \mathbf{I})^2) + \alpha_3 \mathrm{tr}^2(\mathbf{E} - \mathbf{I}),$$

$$W_2(\mathbf{K}) = \beta_1 \mathrm{tr}(\mathbf{K} \cdot \mathbf{K}^T) + \beta_2 \mathrm{tr}(\mathbf{K}^2) + \beta_3 \mathrm{tr}^2(\mathbf{K}),$$

where α_k and β_k, $k = 1, 2, 3$, are constants. In this case, inequality (6) is equivalent to the inequalities [7]

$$\alpha_1 > 0, \quad \alpha_1 + \alpha_2 + \alpha_3 > 0, \quad \beta_1 > 0, \quad \beta_1 + \beta_2 + \beta_3 > 0.$$

Under these conditions, the solutions of Eq. (5) are given by the expressions

$$V_{1,2} = \sqrt{\frac{\alpha_1}{\rho}}, \quad \boldsymbol{\xi}_{1,2} = (\mathbf{e}_{1,2}, \mathbf{0}),$$

$$V_3 = \sqrt{\frac{\alpha_1 + \alpha_2 + \alpha_3}{\rho}}, \quad \boldsymbol{\xi}_3 = (\mathbf{0}, \mathbf{n}), \quad (8)$$

$$V_{4,5} = \sqrt{\frac{\beta_1}{\gamma\rho}}, \quad \boldsymbol{\xi}_{4,5} = (\mathbf{e}_{4,5}, \mathbf{0}),$$

$$V_6 = \sqrt{\frac{\beta_1 + \beta_2 + \beta_3}{\gamma\rho}}, \quad \boldsymbol{\xi}_6 = (\mathbf{0}, \mathbf{n}), \quad (9)$$

where $\mathbf{e}_1$, $\mathbf{e}_2$, $\mathbf{e}_4$, and $\mathbf{e}_5$ are arbitrary unit vectors lying in the plane tangent to S ($\mathbf{e}_1 \cdot \mathbf{e}_2 = \mathbf{e}_1 \cdot \mathbf{n} = \mathbf{e}_2 \cdot \mathbf{n} = 0$,

$\mathbf{e}_4 \cdot \mathbf{e}_5 = \mathbf{e}_4 \cdot \mathbf{n} = \mathbf{e}_5 \cdot \mathbf{n} = 0$). Solutions (8) describe the transverse and longitudinal acceleration waves, and solutions (9), the transverse and longitudinal microrotation acceleration waves. The velocities obtained for the acceleration waves given by Eqs. (8) and (9) coincide with the limiting phase velocities of plane harmonic waves propagating in the linearly elastic micropolar medium [2, 9] when the wave frequency tends to infinity.

ACKNOWLEDGMENTS

REFERENCES

1. É. L. Aéro and E. V. Kuvshinskiĭ, Fiz. Tverd. Tela **2** (7), 1399 (1960).
2. V. A. Pal'mov, Prikl. Mat. Mekh. **28**, 401 (1964).
3. W. T. Koiter, Proc. K. Ned. Akad. Wet., Ser. B: Phys. Sci., No. 1, 17 (1964).
4. R. A. Toupin, Arch. Ration. Mech. Anal. **17** (2), 85 (1964).
5. P. A. Zhilin, Tr. Leningr. Politekhn. Inst., No. 386, 29 (1982).
6. L. I. Shkutin, *Mechanics of Deformations of Flexible Bodies* (Nauka, Novosibirsk, 1988) [in Russian].
7. V. A. Eremeev and L. M. Zubov, Izv. Akad. Nauk: Mekh. Tverd. Tela, No. 3, 181 (1994).
8. V. A. Eremeev and L. M. Zubov, Prikl. Mat. Mekh. **63**, 801 (1999).
9. W. Nowacki, *Theory of Asymmetric Elasticity* (Pergamon, Oxford, 1986).
10. L. M. Zubov, *Nonlinear Theory of Dislocations and Disclinations in Elastic Bodies* (Springer, Berlin, 1997).
11. A. C. Eringen, *Microcontinuum Field Theories. I. Foundations and Solids* (Springer, Berlin, 1999).
12. A. I. Lur'e, *Nonlinear Theory of Elasticity* (Nauka, Moscow, 1980) [in Russian].
13. C. Truesdell, *First Course in Rational Continuum Mechanics* (John Hopkins Univ., Baltimore, 1972; Mir, Moscow, 1975).

Translated by R. Tyapaev

========================= **MECHANICS** =========================

Stationary Motion of a Homogeneous Meteor Ring in a Central Gravitational Field

G. V. Kasatkin

Presented by Academician V.V. Rumyantsev September 17, 2004

Received November 23, 2004

This paper continues the investigation of planet rings in the context of mechanical systems, which began with classical studies [1–3], and deals with the problem of the stationary motion of a meteor ring.

MECHANICAL MODEL OF A METEOR RING

Let the ring be a geometric body obtained as a result of the rotation of a closed plane domain S_r homeomorphic to a circle circumscribed about a Z axis lying in the plane of the domain S_r and nonintersecting this domain. In this case, a fixed point O inside S_r circumscribes the circumference of radius R with the center at a point P in the Z axis. We call this circumference the middle line of the ring, Furthermore, point P, the plane of the middle line, and domain S_r, we call, respectively, the center, the equatorial plane, and the cross section of the ring. We consider the ring to be thin and assume the diameter d of its cross section to be much smaller than the radius

R, i.e., $\dfrac{d}{R} = \varepsilon \ll 1$.

We now assume that the ring is formed by a set of small-mass particles that interact only gravitationally. In addition, the attraction force of the point mass M situated at the ring center acts on each particle of the ring. We also assume that the particles densely fill the ring body so that we can consider it to be a continuum with density Δ.

We associate the inertial coordinate system $PXYZ$ (the PZ axis was defined above, and the PXY plane coincides with the ring equatorial plane) and Cartesian coordinate system $Oxyz$ with the Ox, Oy, and Oz axes directed along the $\overline{PO}$ vector, along the tangent to the middle line, and in parallel to the PZ axis, respectively. The position of the $Oxyz$ coordinate system with respect to the $PXYZ$ coordinate system is determined by the angle φ between the PX axis and the vector $\overline{PO}$.

Tula State University, Tula, 300000 Russia
e-mail: eukas@pochta.ru

The dimensionless variables $\xi = \dfrac{x}{R}$, $\zeta = \dfrac{z}{R}$, and φ unambiguously determine the position of each particle Q of the ring with respect to the inertial coordinate system $PXYZ$. We also denote as S the transform of the cross section S_r in the $O\xi\zeta$ plane, μ and f being the mass of the particle Q and gravitational constant, respectively.

STATIONARY MOTION OF A HOMOGENEOUS RING IN THE ZERO APPROXIMATION

We now seek stationary motions of a homogeneous ($\Delta = \mathrm{const}$) ring for which the geometric shape of the ring is invariable, while the possibility of collisions between its particles is excluded.

The kinetic energy of an arbitrary chosen particle Q is

$$T = \frac{1}{2}\mu R^2 \{\dot{\xi}^2 + \dot{\zeta}^2 + (1+\xi)^2 \dot{\varphi}^2\}, \quad \dot{\xi} = \frac{d\xi}{dt}, \dots .$$

The force function U_P for attracting this particle by the central mass M is given by the formulas

$$U_P = \mu R^2 \omega_0^2 [(1+\xi)^2 + \zeta^2]^{-1/2}, \quad \omega_0^2 = \frac{fM}{R^3}.$$

The force function responsible for the gravitational attraction of particle Q by all other particles of the ring we call U. This function depends essentially on the ring shape. From the possible stationary motions of the ring, we seek those for which it stratifies into a set of tori embedded into each other and shrinking to the middle line. At the same time, the trajectories of particles are nonintersecting windings of the indicated tori referred to below as the stationary tori, whereas the ring itself is called the stationary ring.

By virtue of the constant density, the continuity equation for the medium can be presented in the form of the incompressibility equation

$$\operatorname{div}\mathbf{v} = 0, \tag{1}$$

where $\mathbf{v} = \mathbf{v}(\xi, \zeta, \varphi)$ is the vector field of the stationary ring.

We now consider the Lagrangian

$$\tilde{L} = \tilde{T} + \tilde{U}_P + \tilde{U},$$

$$\tilde{T} = \frac{T}{\mu R^2}, \quad \tilde{U}_P = \frac{U_P}{\mu R^2}, \quad \tilde{U} = \frac{U}{\mu R^2}.$$

In the framework of a conservative mechanical system with the Lagrangian $\tilde{L}$, the equations of motion of a particle Q are invariant with respect to the ring rotation about the PZ axis. Hence, the φ coordinate is cyclic. It is in correspondence with the first integral

$$\frac{\partial \tilde{L}}{\partial \dot{\varphi}} = (1 + \xi)^2 \dot{\varphi} = \sigma, \quad \sigma = \text{const.} \qquad (2)$$

Excluding the φ coordinate according to the Routh method, we arrive at the Lagrangian

$$L_R(\xi, \zeta, \dot{\xi}, \dot{\zeta}) = \frac{\dot{\xi}^2 + \dot{\zeta}^2}{2} - \frac{\sigma^2}{2(1 + \xi)^2} + \tilde{U}_P + \tilde{U}.$$

It determines the motion of the particle Q in the $O\xi\zeta$ plane associated with the given particle. Let l_c be lines along which stationary tori intersect the cross section S. Then, the lines l_c must be invariant manifolds of the equations of motion, which are determined by the Lagrangian L_R. Thus, the problem is reduced to finding the shape of the cross section S and the potential U of the internal gravitational field of the ring for which the indicated conservative mechanical system admits the invariant set of the lines l_c stratifying the cross section S. In our investigation, we take as a reference object a ring of the elliptic cross section $S = S_{\alpha\beta}$ with semiaxes α, $\beta \sim \varepsilon$, $\lambda = \dfrac{\beta}{\alpha} \sim 1$ and with symmetry axes Ou, Ow having angle γ with axes $O\xi$, $O\zeta$. Using the transformation

$$\xi = u\cos\gamma - w\sin\gamma, \quad \zeta = u\sin\gamma + w\cos\gamma,$$

we pass to the Cartesian coordinates u, w related to symmetry axes of the cross section. We note that ξ, ζ, u, $w = O(\varepsilon)$. We here write out (without proof) the desired expression for the function $\tilde{U}$ in terms of the u, w coordinates:

$$\tilde{U} = \omega_0^2 \chi \left[\alpha\beta \left(1 - 2\ln\frac{\alpha + \beta}{16} \right) \right.$$

$$\left. - 2\frac{\lambda u^2 + w^2}{1 + \lambda} + O(\varepsilon^3 \ln\varepsilon) \right],$$

where $\chi = \pi f \Delta \omega_0^{-2} > 0$. The parameter σ^2 entering into the Lagrangian depends on the initial conditions of

motion of the point Q and on the geometric parameters α and λ of the ring. The explicit form of this dependence is unknown *a priori* and should be determined in the course of solving the problem. It is natural to suggest that

$$\sigma^2 = \omega_0^2 (\sigma_0 + \varepsilon\sigma_1 + \varepsilon^2\sigma_2 + \varepsilon^3\sigma_3 + \ldots).$$

Then, within an accuracy to terms on the order of ε^2 and ignoring inessential additive constants, we find

$$L_R = \frac{\dot{u}^2 + \dot{w}^2}{2} + \omega_0^2 \left[(-1 + \sigma_0 + \varepsilon\sigma_1)(u\cos\gamma - w\sin\gamma) \right.$$

$$+ \left(1 - \frac{3}{2}\sigma_0 \right)(u\cos\gamma - w\sin\gamma)^2$$

$$\left. - \frac{1}{2}(u\sin\gamma + w\cos\gamma)^2 - 2\chi\frac{\lambda u^2 + w^2}{1 + \lambda} \right].$$

The equations of motion corresponding to this Lagrangian must admit trajectories l_c stratifying the elliptic cross section $S_{\alpha\beta}$. By virtue of the linearity of the equations of motion, these trajectories can only be ellipses geometrically similar to the boundary ellipse. Then, the equations of motion must take the form [4]

$$\ddot{u} = -\omega^2 u, \quad \ddot{w} = -\omega^2 w,$$

which is possible only in the case that the equalities

$$\sigma_0 = 1, \quad \sigma_1 = 0, \quad \lambda = 1, \quad \omega^2 = \omega_0^2(1 + 2\chi)$$

are valid. Based on these equalities, we can conclude that the cross section $S_{\alpha\beta}$ is the circle of the radius α, and each part of the ring executes uniform motion along the circumference of the radius αc:

$$\xi = \alpha c \cos\psi_0, \quad \zeta = \alpha c \sin\psi_0, \quad \psi_0 = \omega t + \nu,$$
$$\nu = \text{const}, \quad c = \text{const}, \quad c \in [0, 1]. \qquad (3)$$

The law for the variation of the variable φ is found from integral (2):

$$\dot{\varphi} = \omega_0(1 - 2\xi + O(\alpha^2)) = \dot{\varphi}_0 + \alpha\dot{\varphi}_1 + O(\alpha^2),$$
$$\dot{\varphi}_0 = \omega_0, \quad \dot{\varphi}_1 = -2\omega_0 c \cos\psi_0. \qquad (4)$$

This law shows that small oscillations caused by periodic variations with time of the ξ coordinate are imposed on the uniform rise of the angle φ. It is evident that laws (3) and (4) of particle's motion are consistent with incompressibility equation (1).

The results obtained lead to the following interpretation of spatial motion of particles in the stationary ring. The particles move along nonintersecting spiral trajectories adjoining to each other and lying on stationary tori. These trajectories envelop the middle line of

the ring, this line, in itself, being one of the motion trajectories. The complete rotation of a particle about the middle line occurs for a time $\tau = \dfrac{2\pi}{\omega}$, and the complete rotation of a particle about the attracting ring center is realized for a time $\tau_0 = \dfrac{2\pi}{\omega_0}$. We note that $\omega_0 < \omega$, therefore, $\tau_0 > \tau$.

STATIONARY MOTIONS
OF THE HOMOGENEOUS RING
IN THE FIRST APPROXIMATION

It is evident that the search for stationary rings corresponding to more accurate expansions of the Lagrangian L_R over a small parameter ε should be performed for rings with an almost circular cross section. We determine one of the possible classes of these rings in the following manner. We replace the coordinates ξ, ζ by the polar coordinates r, ψ in accordance with formulas

$$\xi = \alpha r \cos\psi, \quad \zeta = \alpha r \sin\psi. \tag{5}$$

We also assume that the lines l_c are given by the relationships

$$r = c + \sum_{k=1}^{\infty} \alpha^k \sum_{n=1}^{\infty} c^n \left(\frac{1}{2} p_{kn,0} \right.$$
$$\left. + \sum_{m=1}^{\infty} p_{kn,m}\cos m\psi + q_{kn,m}\sin m\psi \right), \quad c \in [0,1]. \tag{6}$$

Here, the coefficients $p_{kn,m}$, $q_{kn,m}$ are constant quantities. These coefficients characterize the geometric shape of lines l_c and, in particular, the shape of the boundary line l_1 of cross section S. Formulas (5) and (6) determine the coordinate transformation ξ, $\zeta \longrightarrow c$, ψ. This transformation allows us to reduce the search for stationary ring motions to that for the coefficients $p_{kn,m}$, $q_{kn,m}$ such that the equations of motion admit the invariant manifold $c = $ const. In other words, the following set of equations with respect to the unknown function $\psi(t)$ must be compatible:

$$\left(\frac{\partial L}{\partial \dot{c}} \right)^{\cdot}_{c=\text{const}} = \left(\frac{\partial L}{\partial c} \right)_{c=\text{const}},$$
$$\left(\frac{\partial L}{\partial \dot{\psi}} \right)^{\cdot}_{c=\text{const}} = \left(\frac{\partial L}{\partial \psi} \right)_{c=\text{const}}, \tag{7}$$

where the function $L = \alpha^{-2} L_R$ is the new Lagrangian. Within an accuracy to terms on the order of ε, we have

for almost circular ring (6)

$$L = \frac{\dot{c}^2 + c^2\dot{\psi}^2 - c^2\omega^2}{2} + \alpha\omega_0^2 \left\{ \frac{c^3}{8}(9\cos\psi - \cos 3\psi) \right.$$

$$- cr_1 + \tilde{\sigma}_2 c\cos\psi + \dot{c}\dot{r}_1 + cr_1\dot{\psi}^2 + \chi\left[\frac{c^3}{4}\cos\psi \right.$$

$$- \sum_{n=1}^{\infty} c^{n+1} p_{1n,0}$$

$$\left. \left. + 2\sum_{m,n=1}^{\infty} \left(\frac{c^m}{m} - c^{n+1} \right)(p_{1n,m}\cos m\psi + q_{1n,m}\sin m\psi) \right] \right\},$$

where

$$\tilde{\sigma}_2 = \sigma_2 + \chi\left(1 + \ln\frac{\alpha}{8} \right),$$

$$r_1 = r_1(c,\psi) = \frac{1}{2}\sum_{n=1}^{\infty} c^n p_{1n,0}$$

$$+ \sum_{m,n=1}^{\infty} c^n (p_{1n,m}\cos m\psi + q_{1n,m}\sin m\psi).$$

With allowance for the assigned accuracy of the Lagrangian L, we should seek the solution to Eqs. (7) within the same accuracy. Assuming that $\psi = \psi_0 + \alpha\psi_1 + O(\alpha^2)$, $r_1 = r_1(c,\psi_0) = r_1^{\circ}$, where ψ_0 is the solution of the above-presented zero approximation, we can reach a conclusion on the compatibility of set (7) and find a solution of the form $\psi_1 = \psi_1(c,\psi_0) = \psi_1^{\circ}$. Condition (1) imposes an additional constraint on the functions r_1°, ψ_1°,

$$\frac{\partial}{\partial\psi_0}\left(\frac{\partial r_1^{\circ}}{\partial c} + \frac{1}{c}r_1^{\circ} + \frac{1}{\omega}\dot{\psi}_1^{\circ} + c\cos\psi_0 \right) = 0$$

and results in the following equation determining the lines l_c:

$$r = c + \alpha\left[\frac{1}{2}\sum_{n=1}^{\infty} c^n p_{1n,0} + c^2(C\cos\psi + p\cos 3\psi) \right]$$

$$+ O(\varepsilon^2), \quad \psi \in [0, 2\pi], \quad c \in [0,1],$$

where $p = \dfrac{3}{8(3+8\chi)}$, $C = -\dfrac{3+22\chi}{24(1+2\chi)}$, and

$\sum\limits_{n=1}^{\infty} p_{1n,0} = 0$ is the only requirement that governs arbitrary numbers $p_{1n,0}$.

Assuming $c = 1$, we obtain the equation for boundaries l_1 of the cross section S:

$$r = 1 + \alpha(C\cos\psi + p\cos 3\psi) + O(\varepsilon^2), \quad \psi \in [0, 2\pi].$$

It is worth noting that constants C and p have a quite definite mechanical and geometrical sense, respectively. The constant C fundamentally contributes to value ξ_S of the coordinate ξ of the center-of-mass of the cross section S. At the same time, constant p is associated with curvature $k(\psi)$ of the boundary line l_1 of the cross section S at points $\psi = 0$ and $\psi = \pi$:

$$\xi_S = \alpha^2 C + O(\varepsilon^3), \quad k(0) = 1 + 8\alpha p + O(\varepsilon^2),$$

$$k(\pi) = 1 - 8\alpha p + O(\varepsilon^2).$$

Since $k(\pi) < k(0)$, we can conclude that the curvature of the boundary line l_1 of the cross section S of the stationary ring at the point nearest to the attracting center is smaller than that at the opposite point of the cross-section boundary.

REFERENCES

1. P. S. Laplace, Celest. Mech. **2**, 494 (1966).
2. S. V. Kovalevskaya, *Scientific Papers* (Izd. Akad. Nauk SSSR, Moscow, 1948), pp. 139–152 [in Russian].
3. J. C. Maxwell, in *The Scientific Papers of J.C. Maxwell* (Hermann, Paris, 1927), Vol. 1, pp. 288–374.
4. V. I. Arnol'd, *Mathematical Methods of Classical Mechanics* (Nauka, Moscow, 1989) [in Russian].

Translated by G. Merzon

=== **MECHANICS** ===

Dynamic Model of a Porous Medium Saturated with a Viscous Liquid

S. V. Nesterov and L. D. Akulenko

Presented by Academician D.M. Klimov October 29, 2004

Received November 1, 2004

A dynamic model of a porous medium has been developed. It enables one to calculate inertial and dissipative characteristics of materials from their physical properties and the structural elements of the medium. These characteristics are used to determine the speed of sound and damping of sound in the medium. The existence of viscous–inertial dispersion of acoustic waves has been revealed. The low- and high-frequency ranges of inertial and dissipation properties have been separated, and the transition region has been found. Theoretical conclusions have been qualitatively corroborated by laboratory experiments for certain samples of rock formations.

1. Problems associated with the extraction of liquid and gas mineral products, and with the building of hydraulic structures, underground structures, mines, and transport systems (e.g., tunnels and subways), etc., stimulated the development of filtration theory. Investigations in this field of fluid mechanics were particularly intensive in 1930–1950. At present, the development of new technologies for superfine refinement of substances, the creation of reservoirs for condensed gases using nanocapillary materials, and a number of other engineering problems necessitate the further development of filtration theory.

The most significant achievements in this area to date are mainly associated with investigations into the static and quasi-static actions on the porous medium saturated with a liquid or a gas. The dynamic parameters of the porous medium, which has very complicated rheological characteristics, cannot be revealed when such actions occur. Periodic or pulsed actions on media make it possible to reveal and measure their inertial and dissipative properties. Theoretical and experimental investigations, as well as tests from nature on the propagation and absorption of sound in porous media, are of current interest. This field of continuum mechanics is important for engineering applications. In particular, an increas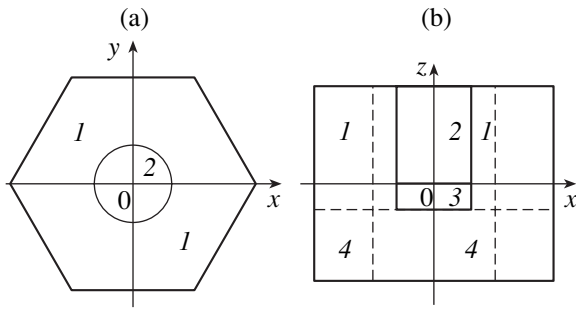e in velocity regimes in transport and machine engineering leads to a harmful increase in noise level. Thus, the creation of comfortable working environments for staff requires new soundproofing devices that are based on porous materials.

2. The first mathematical model of a porous medium consisting of a solid (skeleton) pierced by long narrow channels (pores) filled with a liquid was reported in [1]. However, it was highly idealized and ultimately incomplete, because it described only the character of the damping of an acoustic wave and did not explain other significant mechanical effects. More recently, several theoretical and semiempirical models were developed, but they also had considerable defects. They were not able to relate the frequency characteristics (inertial and dissipative), as well as the speed and damping of sound, to the structural elements measured for media and the physical properties of materials.

The model and theory proposed by Biot [2] appears to be the most universal and pretentious at present. However, the Biot theory has fundamental difficulties that are inherent in all overly general theories. It aims to explain all phenomena related to porous media. The corresponding mathematical models involve numerous unknown parameters, functions, and operators, which are introduced *ad hoc* from general phenomenological considerations. Because of these drawbacks, sufficiently reliable calculations of the inertial and dissipative properties of actual porous-medium samples saturated with a viscous liquid, as well as comparison with experimental results, are impossible.

In this work, we propose a simple rational model of a porous medium saturated with a viscous liquid. The inertial and dissipative properties of the porous medium are calculated on this basis. These properties are determined by the external-action frequency, the physical characteristics of materials, and the structural elements of the medium.

3. We treat a porous medium as a sequence of plane layers. Each layer has nonzero finite thickness and consists of a solid skeleton and pores. Pores are simulated by identical cylinders that are located symmetrically at the centers of regular hexahedrons, which form a cellular structure. The combination of hexagonal prism cells forms the porous-medium layer. A one-dimensional

Institute for Problems in Mechanics,
Russian Academy of Sciences,
pr. Vernadskogo 101-1, Moscow, 119526 Russia

Fig. 1. Geometric characteristics of a porous-medium cell: (a) cross (frontal) section and (b) longitudinal section.
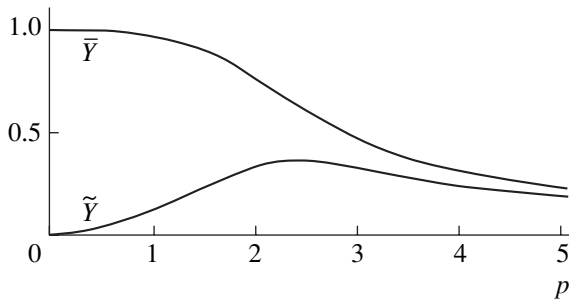
Fig. 2. Plots of the real $\bar{Y}$ and imaginary $\tilde{Y}$ parts of the function Y that determine the transition from low-frequency external actions to high-frequency external actions.

sequence of layers constitutes a volume model of the porous medium.

We consider that pores are partially filled with a viscous liquid. Figure 1 shows the (a) plan view and (b) side view of an individual cell. Each cell is divided into four regions. Regions *1* and *4* belong to the continuous solid skeleton, and region *2* (part of a pore) is filled with a liquid (liquid slug). Additional region *3* is a pore part filled with a low-elasticity gas. The volume of region *3* is assumed to be small compared to the pore volume. The geometrical sizes of the cell are as follows: the solid-base diameter is equal to $2a$, the pore diameter is equal to $2b$ ($b < a$), the pore height is equal to $h = h_1 + h_2$, where h_1 is the liquid slug height ($h_2 \ll h_1$), and the total height of the entire cell is equal to $H > h$.

Time-periodic pressure is applied perpendicularly to the surface of the layer formed by cells. The maximum size of the cell is assumed to be much less than the length of an acoustic wave generating time-periodic variation of pressure. It is necessary to determine the inertial and dissipative properties of the medium that are manifested upon this interaction.

4. The linearized Navier–Stokes equations that describe the motions of the liquid slug in the pore, as well as the equations of motion of skeleton part *1* including no-slip boundary conditions, are integrated in order to develop a mathematical model. For steady

periodic motions, an electromechanical analogue [3] is used with the inclusion of the motion of skeleton part *4*. As a result, a very lengthy expression can be derived for the cell-volume-averaged dynamic density ρ of the porous medium saturated with a viscous liquid.

The analysis of this expression shows that the dynamic density is a complex quantity. Both the real and imaginary parts depend on the external-action frequency ω. The frequency dependence $\rho(\omega)$ is determined by the complex quantity

$$\theta = \gamma b = \sqrt{i}\, p,$$

where

$$p = \left(\frac{\rho_2 \omega}{\mu}\right)^{1/2}, \quad \sqrt{i} = \frac{1+i}{\sqrt{2}}. \tag{1}$$

Here, i is the imaginary unit, ρ_2 is the density of the liquid, μ is the viscosity coefficient,

$$\rho(\omega) = \left(1 - \frac{h}{H}\right)\rho_1 + \frac{h}{H}\rho_{12}(\omega), \tag{2}$$

where

$$\rho_{12} = \rho_2 F(\omega).$$

The function ρ_{12} characterizes an addition caused by the interaction between the skeleton and liquid. The interaction coefficient F for a cylindrical pore is expressed in terms of the Bessel functions J_0 and J_1 of the complex argument θ:

$$F = \frac{L}{D}, \quad L = SA, \quad D = \rho_2(S_1 + S_2 Y)^2 + S_2 A(1 - Y),$$

$$A = \rho_1 S_1 + \rho_2 S_2 Y, \quad Y = \frac{2 J_1(\theta)}{\theta J_0(\theta)} \equiv \bar{Y}(p) + i\tilde{Y}(p). \tag{3}$$

The basic dynamic properties of the density ρ given by Eqs. (2) are determined by the behavior of the function $F(\omega)$ in terms of the dependence of the complex function Y given in Eqs. (3) on the frequency ω, i.e., on the real dimensionless argument p given in Eqs. (1). Note that p dependence disappears at $\rho_1 = \rho_2$. In this case, $F(\omega) \equiv 1$ and $\rho(\omega) \equiv \rho_2$. The real $\bar{Y}$ and imaginary $\tilde{Y}$ parts of the function Y are shown in Fig. 2. The regions $0 \le p \le 1$ and $p \gg 1$ correspond to low- and high-frequency actions, respectively. A pronounced transition occurs in the intermediate region. The region $0.5 \lesssim p \lesssim 5$ can conditionally be treated as the transition region.

Analysis of expression (2) taking into account the asymptotic formulas

$$Y = 1 + i\left(\frac{p}{2}\right)^2 + O(p^4), \quad p \ll 1,$$

$$Y = \frac{1+i}{\sqrt{2}\,p} + O(p^{-2}), \quad p \gg 1 \tag{4}$$

is of applied interest. Approximate expressions for the desired dynamic quantities will be presented below.

5. We introduce the structural elements of the medium, porosity η and opening ξ, as

$$\eta = \frac{V_{23}}{V}, \quad \xi = \frac{S_1}{S_1 + S_2}. \tag{5}$$

Here, $V_{23} = V_2 + V_3$ is the pore volume, V is the volume of the entire cell, S_1 is the area of the cross-section of region *1*, and S_2 is the area of the cross-section of the pore.

If $p \ll 1$, the viscous boundary layer in the liquid is much larger than the radius of the liquid slug. Therefore, the liquid slug moves almost together with the skeleton (solid shell). In this case of low frequencies, the dynamic density ρ_* is written in terms of the structural elements introduced by Eqs. (5) and approximately in p in the form

$$\rho \approx \rho_* = \rho_1(1-\eta) + \rho_2\eta$$
$$-\frac{i\omega b^2}{4\mu}(\rho_1 - \rho_2)^2\eta\xi(1-\xi). \tag{6}$$

It follows from Eq. (6) that an increase in viscosity μ reduces the imaginary part of ρ_* and, thus, reduces damping. In this case, the real part of the dynamic density coincides with the average density of the porous medium, which is determined by standard statistical weighting. We note that $\rho_* = \rho_1$ for $\rho_1 = \rho_2$, as was mentioned above.

If $p \gg 1$, the viscous boundary layer in the liquid is much smaller than the radius of the liquid slug. Therefore, liquid slugs move almost independently of the solid skeleton. In this case of high frequencies, the dynamic density ρ_* is approximately written in terms of the parameter $\dfrac{1}{p}$ in the form

$$\rho \approx \rho^* = \rho_1\left[1 + \eta\frac{\rho_2 - \rho_1}{\rho_2\xi + \rho_1(1-\xi)}\right] + \alpha + i\alpha,$$
$$\text{where} \quad \alpha = \frac{1}{b}\sqrt{\frac{2\mu\rho_2}{\omega}}\eta\frac{(\rho_2 - \rho_1)^2}{[\rho_2\xi + \rho_1(1-\xi)]^2}. \tag{7}$$

The term $O(p^{-1})$ can be neglected in the real part of ρ^* given by Eqs. (7). It follows from Eq. (7) that $\rho^* = \rho_2$ for $\rho_1 = \rho_2$.

6. Comparing Eq. (6) with Eq. (7), the structural elements η and ξ given by Eqs. (5) appear in the real and imaginary parts in different combinations. Note that the real part $\text{Re}\rho^*$ given by Eq. (7) cannot be determined by statistical weighting, but it can be determined by dynamic weighting, e.g., using the resonance method [4, 5].

The structure and dependence on the frequency ω of expressions (6) and (7) are similar to those obtained for a granulated medium saturated with a viscous liquid [5]. They include only the structural elements (η, ξ, b) and physical properties of materials (ρ_1, ρ_2, μ). Therefore, they can be used to explain certain effects observed upon the propagation of sound through the porous medium. According to Eqs. (6) and (7), $\text{Re}\rho_* > \text{Re}\rho^*$. According to estimates for natural dense porous media (marble, granite) saturated with water or oil, the difference between $\text{Re}\rho_* > \text{Re}\rho^*$ is no more than 1–3%. This difference may be much larger for loose rocks and can be found experimentally.

The above analysis completely disregards the elastic properties of the gas that fills region *3* of the pore. If gas elasticity is taken into account in the case of low viscosity, the "liquid slug–gas" system exhibits a resonance at a certain natural frequency Ω. This phenomenon considerably complicates the resulting expressions for the dynamic density. It is particularly important that damping can increase considerably due to the resonance ($\omega \approx \Omega$). Therefore, the above conclusions are also valid if the external-action frequency strongly differs from the natural frequency Ω.

7. The velocities $c(\omega)$ of the propagation of acoustic waves for low and high frequencies and the corresponding damping coefficients are calculated using formulas (6) and (7), respectively, by the standard method [3–5]. The velocity $c_*(\omega)$ of the low-frequency wave is lower than the velocity $c^*(\omega)$ of the high-frequency wave. The damping coefficient for the high-frequency region is also higher than that for the low-frequency region. The transition region from low- to high-frequency dynamic density is determined by the approximate inequalities

$$0.5 \lesssim p = b\sqrt{\frac{\rho_2\omega}{\mu}} \lesssim 3 - 5. \tag{8}$$

The transition from expression (6) to expression (7) occurs in the region given by inequalities (8). We could not reliably determine the difference between ρ_* and ρ^* in experiments utilizing thick rod marble samples, a setup for exciting vibrations, and the measuring instruments available to us. However, we observed a sharp increase in the damping of vibrations in a longitudinally vibrating marble rod saturated with the viscous liquid. The marble rod partially immersed in Vaseline was subjected to vibrational action at a frequency close to the natural frequency. Calculations showed that the case of high frequencies was realized.

8. The basic conclusions are as follows.

A substantial feature of the proposed model is the separation of an elementary cell consisting of a solid shell and a pore filled with a viscous liquid. The final formulas include only the physical parameters and structural elements of the medium. Therefore, it is pos-

sible that these expressions satisfactorily describe the dynamic properties of actual media; i.e., they very likely have application beyond the accepted ideal model.

Comparison of the dynamic characteristics of a porous medium (see above) and a granulated medium [5] saturated with a viscous liquid shows that their behaviors are similar upon periodic actions. Note that the inertial and dissipative properties of these media are manifested as a result of interaction between the viscous liquid and solid walls or solid particles, respectively. The thickness of the viscous boundary layer and the difference between the densities of the solid skeleton (particles) and liquid are the determining parameters.

ACKNOWLEDGMENTS

REFERENCES

1. I. B. Crandall, *Theory of Vibrating Systems and Sound* (D. van Naostrand, New York, 1927).

2. M. A. Biot, J. Acoust. Soc. Am. **34**, 1254 (1962).

3. E. Skudrzyk, *The Foundations of Acoustics: Basic Mathematics and Basic Acoustics* (Springer, New York, 1971; Mir, Moscow, 1976).

4. V. S. Nesterov, Akust. Zh. **5**, 337 (1959).

5. L. D. Akulenko and S. V. Nesterov, Izv. Akad. Nauk: Mekh. Tverd. Tela, No. 5, 145 (2002).

Translated by R. Tyapaev

===================== **MECHANICS** =====================

Microstructure Sources of Sound Backscattering in a Stratified Flow

V. E. Prokhorov

Presented by Academician D.M. Klimov November 15, 2004

Received November 16, 2004

Investigation of sound-scattering mechanisms is of key importance in the development of adequate algorithms for remote diagnostics of the ocean. According to modern concepts, the basic mechanism responsible for the generation of scattering inhomogeneities is assumed to be a turbulent microstructure with an intrinsic scale on the order of the sound wavelength λ. In this case, maximum scattering intensity is expressed in terms of the spectral fluctuation density of sound speed, which is taken at the doubled wavenumber $2k_0 = \dfrac{4\pi}{\lambda}$ of the incident sound wave [1–3]. Since natural stratified flows are known to be inhomogeneous in depth, such a regularity must be valid only at certain horizons in which there exists the developed turbulence. However, from the data of full-scale tests performed in ocean, it follows that the vertical cross-section profiles of scattering strongly correlate with the spectral density of temperature fluctuations in the entire range of probed depths [4, 5]. This implies that the mechanism underlying the formation of the sound-scattering microstructure may be of non-turbulent origin.

It is well known that in the case of oscillatory motion of a body at a frequency ω_i in a homogeneous viscous liquid, a dynamic (velocity-shear) layer with the characteristic size [6]

$$l_\nu = \left(\frac{\nu}{\omega_i}\right)^{1/2} \qquad (1)$$

appears in the near-wall region, where ν is the viscosity of the liquid.

In [7], it was shown that similar layers are formed also in the free space of a stratified liquid when internal waves play the role of a vibration source.

Institute for Problems in Mechanics,
Russian Academy of Sciences,
pr. Vernadskogo 101, Moscow, 119526 Russia
e-mail: prohorov@ipmnet.ru

If the characteristic value of ω_i in ocean is taken to be equal to the average value of the buoyancy frequency $N = 0.05$ s^{-1}, then, at $\nu = 0.01$ cm^2 s^{-1}, the scale of the viscous-layer thickness is about 1.5 cm, which is close to the average operating frequency of a ship's sonar [4, 5, 8]. A microstructure with such an internal scale must efficiently scatter sound waves. This was confirmed in part by laboratory experiments [9] in which scattering by vortex rings was investigated.

In the present study, we experimentally verify the mechanism of sound scattering by the above-mentioned microstructure inhomogeneities in various regimes covering laminar, turbulent, and vortex-type flows.

As a physical model, we consider two-dimensional flow behind a round cylinder. The cylinder is assumed to be moving along the horizontal x axis with a constant velocity in water characterized by vertical (i.e., along the z axis) salt stratification. The flow probing is realized along the vertical direction by acoustical pulses. At the same time, the flow pattern is visualized in a longitudinal vertical cross section by the optical schlieren method. In the standard configuration, the schlieren device is sensitive to the horizontal density gradient $\dfrac{d\rho}{dx}$ [10]. In each experiment, the flow regime is specified by either the velocity of cylinder motion or the cylinder diameter.

A microstructure with an internal scale of the type of (1) is identified by the spectral analysis of reflected signals (in the frequency region) and the schlieren image (in the plane). The data obtained at this stage of investigations are used as initial data to construct the predicted dependence (from the schlieren-pattern spectra) of the relative level of scattering as a function of flow regime (of the Reynolds number). Next, this dependence is compared with the actual experimental curve.

The average intensity I_s of backscattering at the input of the receiving antenna is expressed in terms of the three-dimensional fluctuation spectrum $\Phi_c(\mathbf{k}, x, y, z)$ of sound velocity c (the spectrum is taken at the doubled

wavenumber $2\mathbf{k}_0 = (2k_x, 2k_z)$ of the incident acoustic wave [11]):

$$I_s = 2\pi k_0^4 \frac{I_i D_n^4(r)}{r^2} \int_V \Phi_c(2\mathbf{k}_0, x, y, z) dx\, dy\, dz. \quad (2)$$

Here, I_i is the averaged intensity of the incident radiation; $r = H + \dfrac{a^2}{\lambda}$ and H are the distances from the center of the scattered volume to the imaginary apex of the sound cone and to the antenna plane, respectively; a is the antenna diameter; and $D_n(r)$ is the function of the antenna directivity pattern, which is assumed to be dependent only on the distance $r \gg V^{1/3}$. Due to the narrowness of the directivity pattern, we may consider the volume V to be a round cylinder with its diameter and height equal to the transverse size $R_f = (H\lambda + a^2)^{1/2}$ of the Fresnel zone and $\dfrac{c\tau}{2}$, respectively, where τ is the sound pulse width.

For a flow given in the (x, z) plane, the three-dimensional spectrum entering into relationship (2) is formally expressed in terms of the two-dimensional spectrum $F_c(k_x, k_z)$ as $\Phi_c(\mathbf{k}, x, y, z) = \delta(k_y)F_c(k_x, k_z)$. Then, it follows from (2) that, in the case of vertical probing $(k_x = k_y = 0, k_z = k_0)$, the ratio for the intensities of scattered and incident waves has the form

$$W = 2\pi k_0^4 \frac{D_n^4(r)}{r^2} \int_{-R_f}^{R_f} S(y) F(2k_0, y) dy,$$

where $F(2k_0, y) = \dfrac{1}{S(y)} \int_{x(y)} \int_z F_c(2k_0, x, z) dx dz$ is the spectrum averaged over the vertical cross section $S(y)$ of volume V. This quantity slightly depends on y, so that it can be assumed to be constant and equal to the value of $F(2k_0)$ in the middle cross section $(y = 0)$ of volume V. With allowance for this fact, we arrive at

$$W = 2k_0^4 \frac{D_n^4(r)}{r^2} F(2k_0) V.$$

In this form, the ratio between the intensities of an incident and scattered pulses is determined by the averaged spectrum $F(2k_0)$. The scale representation of this spectrum can be found from the two-dimensional energy spectrum $G(k_x, k_z)$ of the plane schlieren pattern, which is proportional to the spectrum of the horizontal density gradient in a laboratory tank. Hence, assuming, in the first approximation, a linear relation between the

fluctuations of the sound velocity and the density [9], we have

$$F(k_x, k_z) = \frac{BG(k_x, k_z)}{k_x^2},$$

where B is a certain constant.

In order to eliminate the effect of random deviations, we take the spectral component $W(k_n)$ for $F(2k_0)$. The quantity $W(k_n)$ is obtained by averaging $F(k_x, k_n)$ within a certain interval of k_x, namely, for $k_z = k_n$, where k_n is the wavenumber closest to $2k_0$ in the significant spectral region. The values of $W(k_n)$ evaluated over all experiments are normalized to the maximum value of W_m and yield the calculated dependence of the relative scattering level as a function of the Reynolds number:

$$W_I(\mathrm{Re}) = \frac{W(k_n)}{W_m}. \quad (3)$$

The subscript I indicates that this quantity is found according to the optical image, in contrast to its analog W_a, which is calculated from the data array for echo signals:

$$W_a(\mathrm{Re}) = \frac{U_s^2}{U_m}, \quad (4)$$

where U_s and U_m are the current and maximum voltages excited by an echo signal in the reception mode for each of the flow regimes.

Our experiments were performed in a laboratory tank ($240 \times 40 \times 60$ cm³ in size) supplied with a schlieren visualization system characterized by a sight field 23 cm in diameter. The tank was filled with a salt solution according to a method that provided linear stratification at an approximately constant buoyancy period $T_b = \dfrac{2\pi}{N} = 5.3$ s. The flow regime was specified by the Reynolds number $\mathrm{Re} = \dfrac{uD}{\nu}$ and the Froude number $\mathrm{Fr} = \dfrac{u}{ND}$, where D and u are the diameter and velocity of the cylinder, respectively. The range of regimes ($\mathrm{Re} = 40$–1000 and $\mathrm{Fr} = 0.005$–3.5) covers those from laminar to turbulent flows, including vortex and wave-vortex regimes.

Acoustical probing was performed by a laboratory sonar operating at a frequency of 1 MHz ($\lambda = 0.15$ cm). The duration of a sound pulse and the pulse-repetition period were $\tau = 40$ μs and 0.16 s, respectively; the antenna diameter was $a = 2.5$ cm; the angular width of the sound beam was $\varphi = \dfrac{\lambda}{a} = 3.5°$; the power of a sound pulse was 0.3 W; and the distance between the antenna
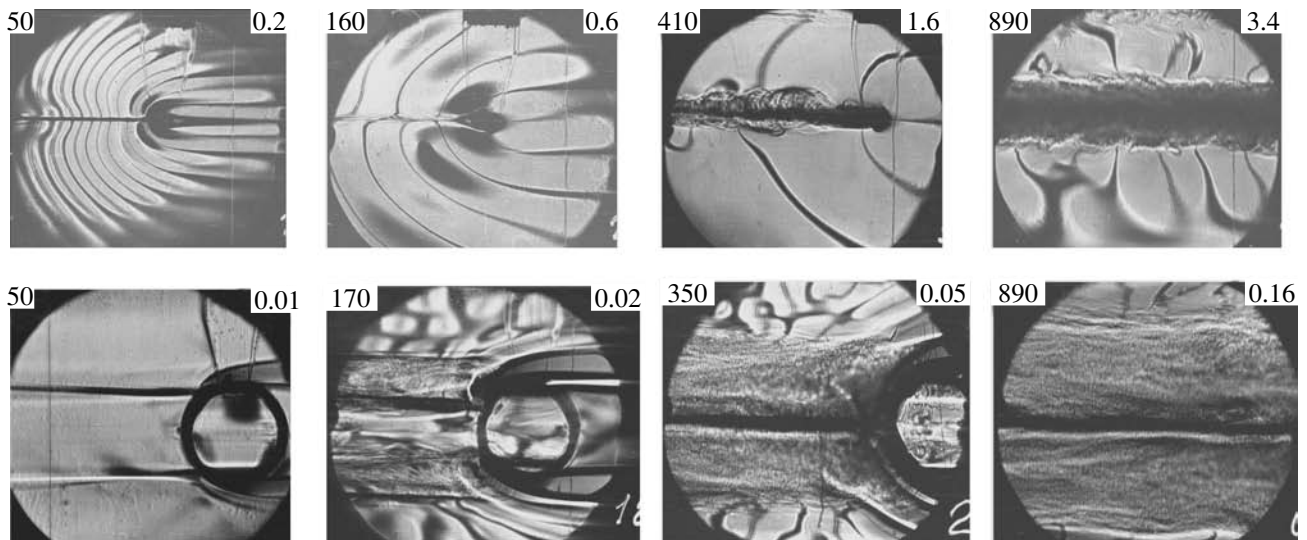
Fig. 1. Schlieren patterns of the wake behind a two-dimensional cylinder moving to the right. For each pattern, the Reynolds number (on the left) and Froude number (on the right) are also indicated. The cylinder diameters are 1.5 and 7.6 cm (the upper and lower rows, respectively).

plane of the sonar and the wake axis was $H = 26$ cm. The axis of the sound beam was directed vertically downward and passed through the tank geometric center. A set of the scattered signals was packed in the form of a matrix in which the row and column numbers were proportional, respectively, to the observation period and to the depth from which a reflected signal arrived.

The cylinder started and moved at a constant velocity u along the longitudinal axis of the tank, crossing the sound beam. In total, we have performed 32 runs with different velocities of motion for two cylinders of small (1.5 cm) and large (7.6 cm) diameters, which made it possible to cover the above range of Reynolds and Froude numbers.

Figure 1 shows the most characteristic flows from the set of regimes under investigation. After the wake of the small-cylinder (1.5 cm, upper row) had been visualized, we installed a filament in the focus of the schlieren device. This made it possible to observe the clear pattern of internal waves. To visualize the flow behind the large cylinder (7.6 cm, lower row), we mounted a knife in the focus. Such a configuration enabled us to separate the solitary discontinuity surfaces that are especially noticeable behind large bodies in laminar-flow regimes. At the left and right boundaries of the regime range, laminar and turbulent structures are present, while in the intermediate region, there exist wave-vortex and vortex regimes. In the wakes behind the small-diameter cylinder, it is possible to distinguish phase surfaces (alternating dark and light arcs) of attached internal waves, their wavelengths being equal to the interval between the phase surfaces. The wavelength increases with the Froude number.

According to (1), the viscous scale can be established from the oscillation frequency of the region

occupied by a given structure. Since only sound-scattering regions participating in wave motion are of interest, the set of frequencies is reduced to those presenting in echo signals and satisfying the condition $\omega_i < N$. Figure 2 shows the backscattering spectrum for the flow regime corresponding to Re = 410 and Fr = 1.6. As seen on the left of the buoyancy frequency, three peaks at the frequencies $\omega_1 - \omega_3$ are present. The scales of a viscous microstructure, which are on the order of the wavelength, correspond to these frequencies (see table).

The normalized two-dimensional spectrum $\dfrac{G(k_x, k_z)}{k_x^2}$ of this flow is shown as a half-tone image in Fig. 3. The spectral intensity is proportional to the darkening density. Hereafter, the wavenumber is assumed to be equal to the reverse scale (without the factor 2π). The given spectrum illustrates the common character of scale variability (having a magnitude comparable with the sound wavelength) in the wavelength millimeter
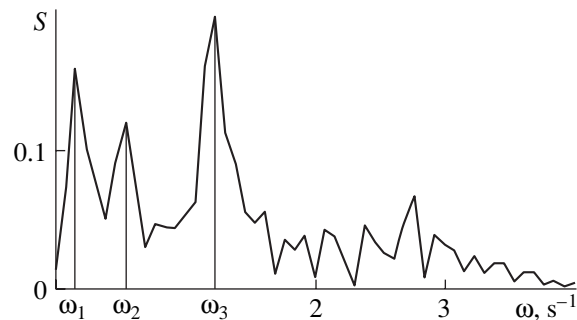
Fig. 2. Normalized frequency spectrum S for backscattering on a wake (Re = 410, Fr = 1.6).

k_z, cm^{-1}

k_x, cm^{-1}
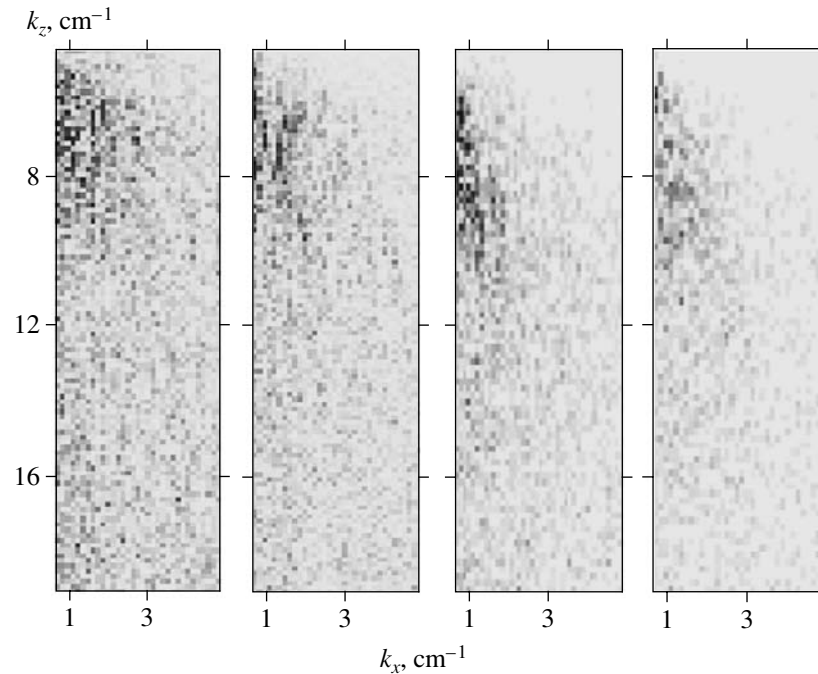
Fig. 3. Two-dimensional spectra $\dfrac{G(k_x, k_z)}{k_x^2}$ in the half-tone image. The flow regime corresponds to Re = 410 and Fr = 1.6. The wake ages $\dfrac{t}{T_b}$ are 3, 4, 6, and 10 (from left to right).

range for all regimes under investigation. The energy-significant spectrum occupies the wavenumber regions $5 < k_z < 12$ cm^{-1} and $0.1 < k_x < 2.5$ cm^{-1}, which corresponds to the scale ranges $0.08 < l_z < 0.2$ cm and $0.4 < l_x < 10$ cm. With increase in the wake age, the range of maximum spectral intensity approaches the k_z axis and shifts towards larger values of k_z. Thereby, the typical evolution of unsteady stratified flow is revealed, namely, the increase and decrease in the horizontal and vertical scales, respectively. At the early and developed stages, the vertical scale of the most intense microstructure is close to 0.14 cm ($k_z = 7$ cm^{-1}) and 0.11 cm ($k_z = 9$ cm^{-1}), respectively. Thus, according to the table and Fig. 2, the significant region of the millimeter-scale microstructure is concentrated in the vicinity of viscous scales. The closeness of their values to the sound wavelength indicates the participation of these structure inhomogeneities in the sound scattering.

Table

ω_i, s^{-1}	l_v, cm	$k_v = l_v^{-1}$, cm^{-1}
$\omega_1 = 0.153$	0.25	4
$\omega_2 = 0.578$	0.13	7.7
$\omega_3 = 1.16$	0.09	11.1

Figure 4 shows the experimental (4) and calculated (3) scattering levels as functions of the Reynolds number for the large cylinder (7.6 cm in diameter) at $k_n = 12$ cm^{-1} and the averaging region of $0.05 < k_x < 0.5$ cm^{-1}. The dependences W(Re) for the small cylinder have a similar character with the same features. It is seen that within the entire range of regimes, the character of spectral representations (3) satisfactorily agrees with that of the curves for experimental dependences (4). Their characteristic feature, namely, the existence of the minimum in the vicinity of Re = 150 is associated with the modification of the scattering type from the gradient (surface) type to volume scattering after the laminar flow regime has passed to the turbulent regime. In the schlieren patterns (Fig. 1), it is seen that, for the weak regimes (Re < 150), the wakes contain one or two horizontal discontinuity surfaces that produce intense mirror scattering [12]. When the regime approaches the value Re = 150, these surfaces begin to erode so that scattering decreases. The flow becomes more intense with the Reynolds number Re, and the concentration of the volume structure rises, which is accompanied by an increase in the scattering level.

According to the data obtained, the microstructure with typical scale (1) is observed at all stages and regimes of stratified flow. The value of the viscous scale obtained from data related to backscattered signals corresponds to the energy-significant part of the optical image spectrum. The dependences of the scattering
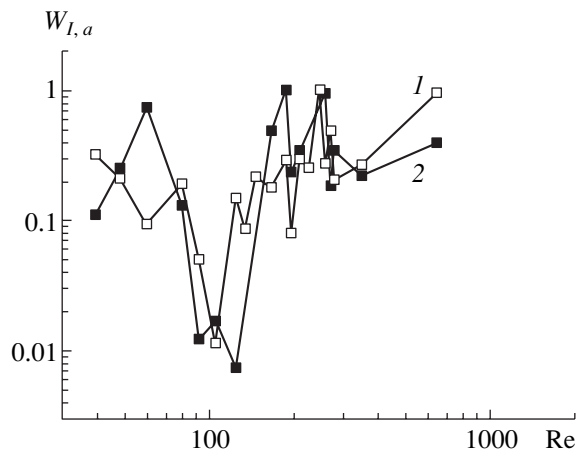
Fig. 4. Relative scattering level in the wake behind the cylinder 7.6 cm in diameter as a function of the Reynolds number according to: (*1*) backscattering data (W_a) and (*2*) spectra of schlieren patterns (W_I).

level on the Reynolds number, which are calculated in terms of the spectral components within the viscous-scale range, are in good agreement with data provided by direct acoustical measurements. These arguments indicate that viscous scale (1) plays a cross-linking role in sound-scattering inhomogeneities. In contrast to turbulence, the above-considered mechanism for generating the microstructure does not require high values for the velocity shear, which favors the universal realization of this mechanism in the wide range of flow regimes in the ocean.

ACKNOWLEDGMENTS

REFERENCES

1. *Physics of Ocean*, Ed. by A. S. Monin (Nauka, Moscow, 1978), Vol. 2.

2. L. Goodman, J. Geophys. Res. C **95** (7), 11 557 (1990).

3. A. C. Lavery, R. W. Schmitt, and T. K. Stanton, J. Acoust. Soc. Am. **114**, 2685 (2003).

4. G. V. Zheleznyak, A. I. Lomeĭko, and A. A. Lyubitskiĭ, Sudostroit. Promyshl., Ser. Akustika, No. 3, 18 (1988).

5. V. G. Korenev, A. I. Lomeĭko, A. A. Lyubitskiĭ, *et al.*, Akust. Zh. **25**, 556 (1979).

6. L. D. Landau and E. M. Lifshitz, *Fluid Mechanics*, 2nd ed. (Nauka, Moscow, 1986; Pergamon Press, Oxford, 1987).

7. Yu. V. Kistovich and Yu. D. Chashechkin, Prikl. Mekh. Tekh. Fiz. **39** (5), 88 (1998).

8. I. Pelech, G. Zipfel, and R. Holford, J. Acoust. Soc. Am. **73**, 528 (1983).

9. V. E. Prokhorov and Yu. D. Chashechkin, Dokl. Akad. Nauk **388**, 334 (2003) [Dokl. Phys. **48**, 51 (2003)].

10. L. A. Vasil'ev, *Schlieren Methods* (Nauka, Moscow, 1968; Israel Program for Scientific Translations, Jerusalem, 1971).

11. S. M. Rytov, Yu. A. Kravtsov, and V. I. Tatarskiĭ, *Introduction to Statistical Radiophysics* (Nauka, Moscow, 1978), Part 2.

12. V. E. Prokhorov, Meteorol. Atmos. Phys. **85** (1–3), 39 (2004).

Translated by Yu. Vishnyakov

=== **MECHANICS** ===

On the Theory of Roll Waves in Inclined Channels

E. A. Demekhin, E. N. Kalaĭdin, and E. M. Shapar'

Presented by Academician V.A. Babeshko April 23, 2004

The stability of a plane-parallel viscous flow in an inclined plane has been analyzed for the first time on the basis of the linearized Reynolds equations for a turbulent flow. The critical Froude number Fr and the surface velocity have been determined as functions of the Reynolds number Re and the channel slope. It was shown that the plane-parallel flow loses stability for Froude numbers ranging from Fr* $\simeq$ 1.2 to Fr* $\simeq$ 1.5.

The rough hydraulic approach used earlier for turbulent flow regime was based on averaging equations of motion and application of the empirical Chezy formula [1, 2]. This determines the instability range for Froude numbers Fr > 2 (the surface wave velocity is equal to 1.5). These results contradict the experimental data [3], which are indicative of much earlier onset of instability (Fr $\approx$ 1).

1. The two-dimensional viscous turbulent flow in a plane inclined at an angle θ to the horizon is governed by the system of Reynolds equations [4]

$$\frac{\partial u}{\partial t} + u\frac{\partial u}{\partial x} + v\frac{\partial u}{\partial y} = -\frac{\partial p}{\partial x} + \frac{\partial \tau_{xx}}{\partial x} + \frac{\partial \tau_{xy}}{\partial y} + \frac{\sin\theta}{\mathrm{Fr}^2},$$

$$\frac{\partial v}{\partial t} + u\frac{\partial v}{\partial x} + v\frac{\partial v}{\partial y} = -\frac{\partial p}{\partial y} + \frac{\partial \tau_{xy}}{\partial x} + \frac{\partial \tau_{yy}}{\partial y} - \frac{\cos\theta}{\mathrm{Fr}^2}, \quad (1)$$

$$\frac{\partial u}{\partial x} + \frac{\partial v}{\partial y} = 0.$$

The boundary conditions imposed on the interface $y = h(x, t)$ and the rigid wall $y = 0$ are as follows:

$$y = h(x, t): \, -p + \tau_{xx}n_x^2 + 2\tau_{xy}n_x n_y + \tau_{yy}n_y^2 = 0,$$

$$(\tau_{xx} - \tau_{yy})n_x n_y + \tau_{xy}(n_y^2 - n_x^2) = 0, \quad (2)$$

$$y = 0: u = v = 0,$$

where $\mathbf{n} = (n_x, n_y)$ is the unit outward normal vector to the surface $y = h(x, t)$.

Kuban State University,
ul. Stavropol'skaya 149, Krasnodar, 350040 Russia
e-mail: Kalaidin@econ.kubsu.ru

The equations are made dimensionless by scaling on the waveless layer thickness $\tilde{h}_0$, the fluid velocity on the interface $\tilde{U}_0$, and the fluid density $\tilde{\rho}$. We define the dimensionless friction coefficients for the shear stress on the wall in the plane flow

$$\tau_{xy}|_{y=0} = \tau_w = c_f,$$

and obtain the following relation between the friction coefficients and the Froude number:

$$c_f = \frac{\sin\theta}{\mathrm{Fr}^2}, \quad \mathrm{Fr}^2 = \frac{\tilde{U}_0^2}{\tilde{g}\tilde{h}_0}.$$

To make the comparison with the experimental data more convenient, we also consider the Reynolds and Froude numbers based on the mean-flow-rate velocity

$$\langle \mathrm{Re} \rangle = \frac{\langle \tilde{U} \rangle \tilde{h}_0}{\tilde{v}}, \quad \langle \mathrm{Fr} \rangle^2 = \frac{\langle \tilde{U} \rangle}{\tilde{g}\tilde{h}_0}.$$

For a given velocity profile, one set of dimensionless parameters can easily be recalculated to another. The Reynolds stresses are as follows:

$$\tau_{ij} = \left(\frac{1}{\mathrm{Re}} + v_T^{ij}\right)\left(\frac{\partial u_i}{\partial x_j} + \frac{\partial u_j}{\partial x_i}\right), \quad i, j = x, y;$$

where

$$v_T^{ij} = l^2\left|\frac{\partial u_i}{\partial x_j} + \frac{\partial u_j}{\partial x_i}\right|.$$

The Van Driest formula [5] is taken for the Prandtl's mixing length

$$l = \kappa y\left[1 - \exp\left(\frac{y\mathrm{Re}\sqrt{c_f}}{A}\right)\right].$$

2. Setting $\frac{\partial}{\partial t} = \frac{\partial}{\partial x} = 0$ in the system of Eqs. (1) and (2), we obtain the equation governing the plane-parallel flow

$$\frac{1}{\mathrm{Re}}\frac{\partial U}{\partial y} + l^2\left(\frac{\partial U}{\partial y}\right)^2 = c_f(1 - y) \quad (3)$$

with the boundary condition

$$y = 1: \frac{\partial U}{\partial y} = 0. \tag{4}$$

The solution of the system of Eqs. (3) and (4) was obtained numerically under the velocity normalization condition $U|_{y=1} = 1$. This condition provides a relation between the friction coefficient and the Reynolds number, i.e., the friction law $c_f = c_f(\text{Re})$. It is interesting to note that

$$U''|_{y=1} = -\text{Re} c_f \neq 0.$$

3. We now investigate the stability of the solution obtained. Let the plane-parallel flow be subjected to small perturbations of the form:

$$u = U(y) + \varepsilon \hat{u}(y)E, \quad v = \varepsilon \hat{v}(y)E,$$

$$h = 1 + \varepsilon \hat{h}E, \quad \tau_{xx} = \varepsilon \hat{\tau}_{xx}E, \quad \tau_{yy} = \varepsilon \hat{\tau}_{yy}E,$$

$$\tau_{xy} = c_f(1-y) + \varepsilon \hat{\tau}_{xy}E, \quad \nu_T^{xy} = \nu_T^{(0)} + \varepsilon \hat{\nu}E,$$

$$E = e^{i(\alpha x - \alpha c t)}, \quad \varepsilon \longrightarrow 0.$$

After these relations have been substituted in system (1) and (2) and the system has been linearized, we obtain the following set of equations:

$$i\alpha(U-c)\hat{u} + U'\hat{v} = -i\alpha\hat{p} + i\alpha\hat{\tau}_{xx} + \hat{\tau}'_{xy},$$

$$i\alpha(U-c)\hat{v} = -\hat{p}' + i\alpha\hat{\tau}_{xy} + \hat{\tau}'_{yy},$$

$$\hat{v} + i\alpha\hat{u} = 0,$$

$$y = 1: -\hat{p} + \frac{\cos\theta}{\text{Fr}^2}\hat{h} + \frac{2}{\text{Re}}\hat{v}' = 0,$$

$$\hat{u}' + i\alpha\hat{v} = c_f\text{Re}\hat{h}, \quad \hat{v} = i\alpha(U-c)\hat{h},$$

$$y = 0: \hat{u} = \hat{v} = 0.$$

We consider the critical point at which the flow loses its initial stability. Assuming instability to be long-wave, we have $\alpha \longrightarrow 0$ in the vicinity of the critical point. We retain only the terms of no greater than first order in α. Then, introducing the stream function $\hat{u} = \varphi'$, $\hat{v} = -i\alpha\varphi$, we arrive at the boundary value problem

$$\left[\left(\frac{1}{\text{Re}} + 2l^2 U'\right)\varphi''\right]' = i\alpha[\hat{p} + (U-c)\varphi' - U'\varphi],$$

$$y = 1: \varphi'' = c_f\text{Re}, \quad \varphi = c - 1, \tag{5}$$

$$y = 0: \varphi = \varphi' = 0.$$

For $\alpha \longrightarrow 0$, we have

$$\varphi \sim A(\varphi_0 + i\alpha\varphi_1 + i\alpha c\varphi_2) + i\alpha\hat{p}\varphi_*,$$

$$c \sim c_0 + i\alpha c_1, \quad A \sim A_0 + i\alpha A_1.$$

For φ_0,

$$\varphi_0'' = \frac{\text{Re}}{1 + 2l^2\text{Re} U'},$$

where φ_0' and φ_0 are determined by integrating with the use of the boundary conditions. For φ_1, we obtain the equation

$$\left[\left(\frac{1}{\text{Re}} + 2l^2 U'\right)\varphi_1''\right]' = U\varphi_0' - U'\varphi_0.$$

Integration of this equation yields

$$\varphi_1'' = \frac{\text{Re}\left(U\varphi_0 - 2\int_0^y U'\varphi_0 dy\right)}{1 + 2l^2\text{Re} U'}.$$

For φ_2 and φ_*, we arrive at the equations

$$\varphi_2'' = \frac{-\text{Re}\varphi_0}{1 + 2l^2\text{Re} U'}, \quad \varphi_*'' = \frac{\text{Re} y}{1 + 2l^2\text{Re} U'}.$$

We now substitute our expansion in boundary conditions (5)

$$(A_0 + i\alpha A_1)(\varphi_0'' + i\alpha\varphi_1'' + i\alpha c_0\varphi_2'') + i\alpha\hat{p}\varphi_*'' = c_f\text{Re},$$

$$(A_0 + i\alpha A_1)(\varphi_0 + i\alpha\varphi_1 + i\alpha c_0\varphi_2) + i\alpha\hat{p}\varphi_*$$
$$= c_0 - 1 + i\alpha c_1.$$

In the zeroth approximation, we have

$$A_0\varphi_0'' = c_f\text{Re},$$

$$A_0\varphi_0 = c_0 - 1.$$

Thence we obtain $A_0 = c_f$; that is, for neutral stability we have
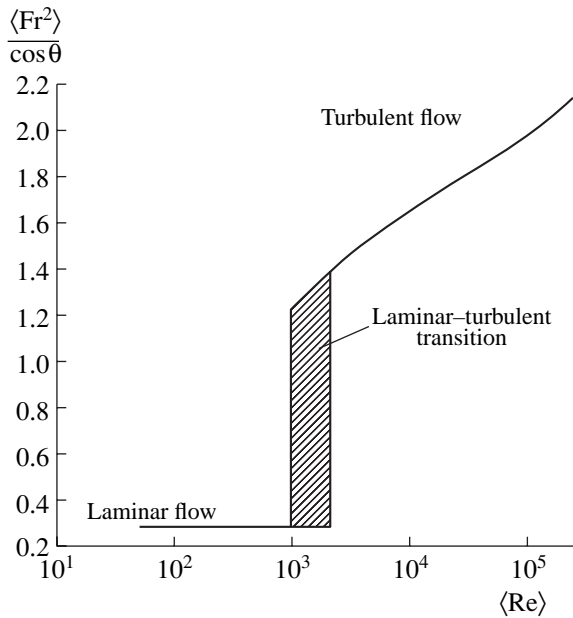
$$c_0 = 1 + c_f\varphi_0|_{y=1}.$$

In the next approximation,

$$A_1\varphi_0'' + A_0(\varphi_1'' + c_0\varphi_2'') + \hat{p}\varphi_*'' = 0,$$

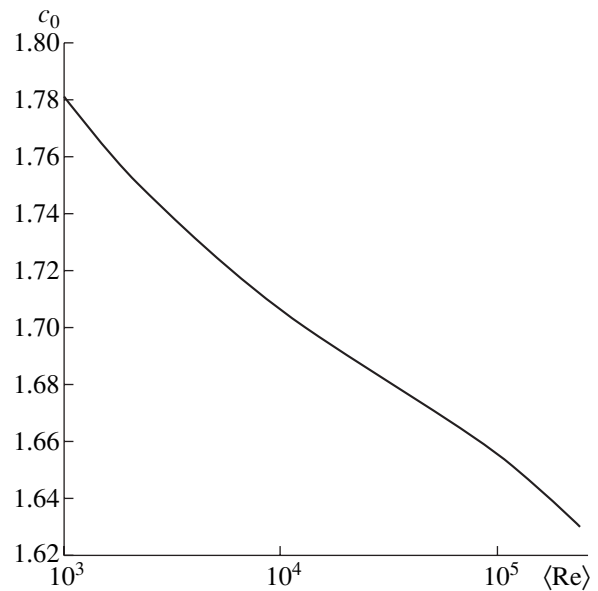$$A_1\varphi_0 + A_0(\varphi_1 + c_0\varphi_2) + \hat{p}\varphi_* = c_1,$$

and $c_1 = 0$ is the critical condition. Transformations of the last system lead to the equation

$$\frac{c_f}{\varphi_0}(\varphi_1 + c_0\varphi_2) + c_f\left(c_0\varphi_0 - \frac{\varphi_1''}{\text{Re}}\right) = \frac{\cos\theta}{\text{Fr}^2}\left(1 - \frac{\varphi_*}{\varphi_0}\right).$$

We present the results in the form of a Re-dependence

Fig. 1. $\dfrac{\langle \mathrm{Fr} \rangle^2}{\cos\theta}$ vs. the mean-flow rate Reynolds number $\langle \mathrm{Re} \rangle$.

Fig. 2. Surface velocity c_0 vs. the mean-flow rate Reynolds number $\langle \mathrm{Re} \rangle$.

of the cotangent of the angle

$$\cot\theta = \frac{\varphi_1 + c_0\varphi_2 + c_0\varphi_0^2 - \dfrac{\varphi_0\varphi_1''}{\mathrm{Re}}}{\varphi_0 - \varphi_*} f(\mathrm{Re}), \qquad (6)$$

where $c_0 = 1 + c_f\varphi_0$.

For any fixed Reynolds number that is so large that the flow is turbulent, φ_0, φ_1, φ_2, φ_*; and, hence, c_0 can be determined by successive integration. We can then also determine the right-hand side of Eq. (6), which depends only on Re, and, hence, the critical angle θ^* and, therefore, Fr*. The calculated results are presented

in Fig. 1 in the form of a dependence of $\dfrac{\langle \mathrm{Fr} \rangle^2}{\cos\theta}$ on the

mean-flow-rate Reynolds number $\langle \mathrm{Re} \rangle$.

We assumed that the laminar–turbulent transition occurs for $\langle \mathrm{Re} \rangle \approx 1000$–1500. This region is shaded in

Fig. 1. In the laminar flow region [6], $\dfrac{\langle \mathrm{Fr} \rangle^2}{\cos\theta} = \dfrac{5}{18}$. In

the laminar–turbulent transition, the critical Froude

number changes abruptly to $\dfrac{\langle \mathrm{Fr} \rangle^2}{\cos\theta} = 1.2$ and then

increases with $\langle \mathrm{Re} \rangle$ up to 2.2. In this case, Fr* varies from 1.1 to 1.5, in contrast to the hydraulic approach predictions (Fr* = 2). Under critical conditions, the sur-

face velocity is greater than the value $c = \dfrac{3}{2}$ predicted

by the hydraulic approach (Fig. 2).

REFERENCES

1. R. F. Dressler, Commun. Pure Appl. Math. **2**, 149 (1949).
2. G. B. Witham, *Linear and Nonlinear Waves* (Wiley, New York, 1974; Mir, Moscow, 1977).
3. M. G. Foley and V. A. Vanoni, J. Hydraul. Div., Am. Soc. Civ. Eng. **8**, 843 (1977).
4. K. K. Fedyaevskiĭ, A. S. Ginevskiĭ, and A. V. Kolesni-kov, *Calculation of Turbulent Incompressible Boundary Layers* (Sudostroenie, Leningrad, 1973) [in Russian].
5. E. R. van Driest, J. Aeronaut. Sci. **23** (2) (1956).
6. T. B. Benjamin, J. Fluid Mech. **2**, 554 (1957).

Translated by M. Lebedev

=== **MECHANICS** ===

On Evolutional and Catastrophic Regimes of Meso–Macro Energy Exchange in Dynamically Loaded Media

Yu. I. Mescheryakov

Presented by Academician N.F. Morozov October 18, 2004

Received November 3, 2004

Study of the role of velocity fluctuations in processes of energy exchange between mesoscopic and macroscopic scale levels represents an important stage in the development of our knowledge about the shock-wave behavior of heterogeneous materials. In the case of dynamic deformation, the concept of mesoparticle has much wider meaning as applied to quasistatic processes, in which mesoparticles are specific structural defects such as dislocation groups, vortex structures, shear bends, and other structural formations of scale 0.1–10 μm [1]; they represent field structures, the only distinct feature of which is the presence of a velocity-correlated group of medium points. This means that a mesoparticle is a space formation, the internal points of which have identical or close velocities. The lifetime of these structures is determined by the duration of the dynamic deformation process. Each mesoparticle, as a separate structural formation, has its own overall velocity. In a heterogeneous medium, a dynamically deformed structure is characterized by velocity scattering. Therefore, mesoparticle velocity fluctuations can remove a considerable part of momentum and energy transferred to the medium.

According to recent experiments [2], the generally accepted opinion that 90% of plastic work is immediately transformed into heat is erroneous. It is found that, in the microsecond range of dynamic loading, only 30–35% of plastic work is transformed into heat, while the rest of the work is spent on the formation of the mesostructure. The main mechanism of structure formation is large-scale velocity fluctuations, the quantitative characteristic of which is the standard deviation of the mesoparticle velocities.

Analysis of the experimental data on shock loading of materials reveals two regimes of energy exchange between mesoscales and macroscales of dynamic deformation—smooth or evolutional and catastrophic regimes. The latter regime implies that the mean particle velocity decreases suddenly at a certain strain rate,

while the standard deviation of velocities increases. This statement was verified by impact tests of two sets of 30XH4M steel targets subjected to different thermal treatments. As an example, Fig. 1 shows the time profiles of the mean velocity and standard deviation of velocities as obtained upon plane impact loading of two targets with velocities of 324 and 320 m/s. The profiles were recorded using a two-channel velocity interferometer [3]. Although the impact velocities are close to each other in these experiments, the time profiles of the mean velocity and standard deviation of velocities are significantly different. In the first case, the mean velocity increases gradually up to 310 m/s, while in the second case, the break of the mean velocity occurs at a velocity of 160 m/s (point *B* in Fig. 1b). The behavior of the standard deviation of velocities is opposite: its increase rate is much higher in the second case. The second case corresponds to the catastrophic regime of energy exchange between the mesoscale and macroscale.

To deduce a criterion for the transition from the evolutional to catastrophic regime of energy exchange between the mesoscopic and macroscopic scales of dynamic deformation, we consider the one-dimensional propagation of an elastoplastic wave in a medium characterized by mesoscopic velocity fluctuations. The equations of momentum and mass conservation have the form

$$\rho \frac{\partial v}{\partial t} = \frac{\partial \sigma_1}{\partial x}, \quad \frac{\partial v}{\partial x} = \frac{\partial \varepsilon_1}{\partial t}. \tag{1}$$

Here, v is the mean velocity of particles, σ_1 is the normal stress, and ε_1 is the total (elastic plus plastic) strain in the direction of wave-propagation. The second equation can be represented in the form

$$\frac{\partial v}{\partial x} - \frac{\partial \varepsilon_1^e}{\partial t} = \frac{\partial v^{pl}}{\partial x}, \tag{2}$$

where v^{pl} is the velocity of plastic mass transfer and ε_1^e is the elastic strain. A similar representation is known in continuum dislocation theory, where the second term on the right-hand side of Eq. (2) is expressed in terms of dislocation density flux tensor [4].

Institute of Problems of Mechanical Engineering,
Russian Academy of Sciences, V.O.,
Bol'shoi pr. 61, St. Petersburg, 199178 Russia
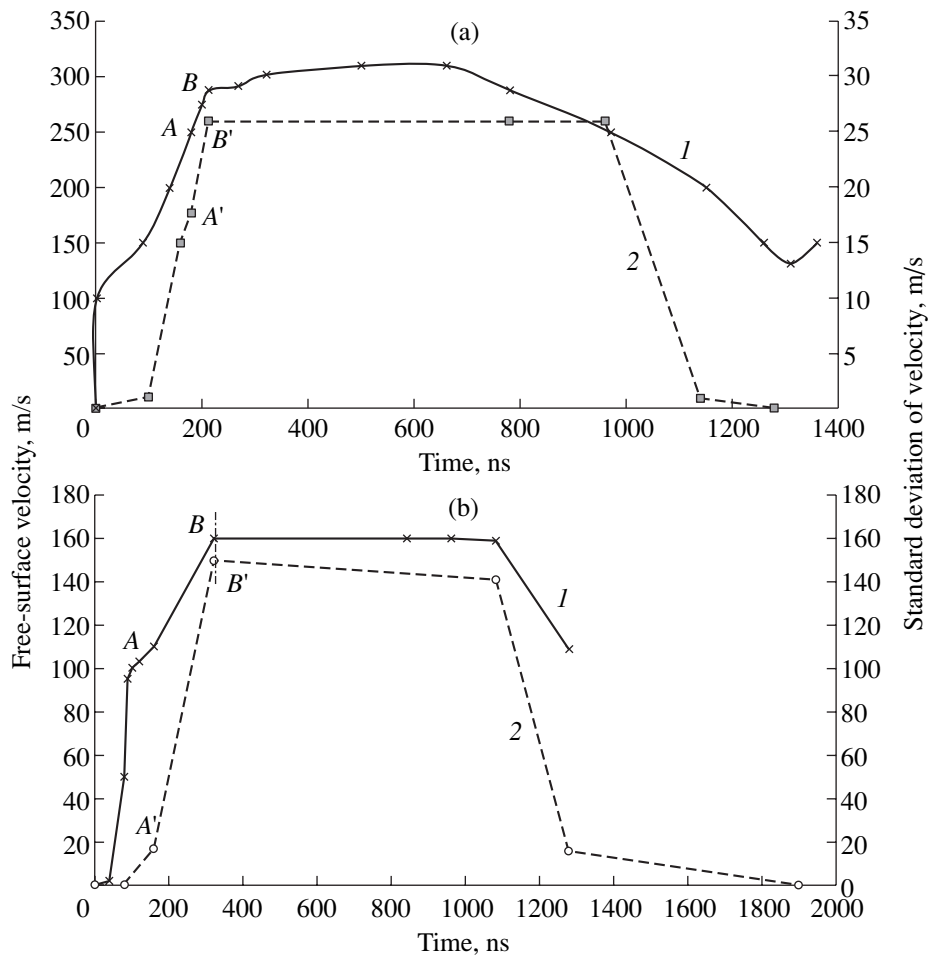
Fig. 1. Profiles of the (*1*) free-surface velocity and (*2*) standard deviations of velocities for a target of the (a) first and (b) second sets of 30XH4M steel.

The normal stress component σ_1 may also be represented as a sum of the elastic and plastic parts, $\sigma_1 = \sigma_1^e + \sigma_1^{pl}$, where the elastic stress is determined by Hooke's law

$$\sigma_1^e = (\lambda + 2\mu)\varepsilon_1^e, \qquad (3)$$

where λ and μ are the Lame constants. In view of Eqs. (2) and (3), the momentum and continuity balance equations are reduced to the equation

$$c_1^2 \frac{\partial^2 v}{\partial x^2} - \frac{\partial^2 v}{\partial t^2} = c_1^2 \frac{\partial^2 v^{pl}}{\partial x^2} - \frac{1}{\rho}\frac{\partial^2 \sigma_1^{pl}}{\partial x \partial t}, \qquad (4)$$

where the left-hand side is the wave operator and c_1 is the longitudinal speed of sound [$c_1^2 = \dfrac{\lambda + 2\mu}{\rho}$]. Let us consider the right-hand side of this equation. For an unsteady wave, the velocity of plastic mass transfer v^{pl}

can be represented as the sum of equilibrium and non-equilibrium components

$$v^{pl} = v_{eq}^{pl} + v_{noneq}^{pl}. \qquad (5)$$

These components are determined by, respectively, the equilibrium f_0 and nonequilibrium f_1 parts of the velocity distribution function $f = f_0 + f_1$ of particles [5]:

$$v_{eq}^{pl} = \frac{1}{\rho}\int_{-\infty}^{\infty} v f_0 dv, \quad v_{noneq}^{pl} = \frac{1}{\rho}\int_{-\infty}^{\infty} v f_1 dv. \qquad (6)$$

To determine the nonequilibrium component of the velocity distribution function f_1, the reciprocal kinetic equation must be solved. When the collision integral is unknown, the most convenient variant of kinetic equation is the relaxation form [6]

$$\frac{\partial f}{\partial t} + v\frac{\partial f}{\partial r} + \langle \dot{v}\rangle\frac{\partial f}{\partial v} = -\frac{f - f_0}{\tau_R}, \qquad (7)$$

where τ_R is the relaxation time for the velocity distribution function of mesoparticles. The velocity distribu-

tion function changes as a consequence of relaxation processes much faster than it does when the change is due to convective mass transfer. Therefore, one can neglect the first two terms on the left-hand side of Eq. (7). In this case,

$$f_1 = \tau_R \langle \dot{v} \rangle \frac{\partial f_0}{\partial v}. \tag{8}$$

For the central interaction, the mean acceleration $\langle \dot{v} \rangle$ of particles may be expressed in terms of the potential as $\langle \dot{v} \rangle = \frac{1}{m} \text{grad}\Pi$. However, the interaction potential for mesoparticles is not central, and its form remains unknown to date. Therefore, we determine the acceleration of mesoparticles in terms of the mean fluctuations of their velocities: $\langle \dot{v} \rangle = \frac{\langle \Delta v \rangle}{\Delta t}$. For the fluctuating medium, the following relation between $\frac{\langle \Delta v \rangle}{\Delta t}$ and the standard deviation of particle velocities is well known [7]:

$$\frac{\langle \Delta v \rangle}{\Delta t} = \frac{1}{2}\frac{dF_2}{dv}. \tag{9}$$

Here, F_2 is the second diffusion coefficient in the Fokker–Planck equation, which can be written in terms of the velocity variance $D^2 = \langle \Delta v \Delta v \rangle$ as

$$F_2 = \frac{\langle \Delta v \Delta v \rangle}{\Delta t}. \tag{10}$$

Taking into account that the mean velocity varies for the relaxation time $\Delta t = \tau_R$, we obtain

$$\langle \dot{v} \rangle = \frac{\langle \Delta v \rangle}{\tau_R} = \frac{1}{\tau_R}\frac{dD^2}{dv}. \tag{11}$$

Then, the nonequilibrium part of the velocity distribution function equals

$$f_1 = -\frac{\partial f_0}{\partial v}\frac{\partial D^2}{\partial v}, \tag{12}$$

and the nonequilibrium component of the average mass transfer rate is expressed as

$$v_{\text{noneq}}^{\text{pl}} = \frac{1}{\rho}\int_{-\infty}^{\infty} v\frac{\partial f_0}{\partial v}\frac{\partial D^2}{\partial v}dv = \frac{\partial D^2}{\partial v}. \tag{13}$$

Let us consider the second item on the right-hand side of Eq. (4). The stress σ_1^{pl} is also the sum of the equilibrium and nonequilibrium parts:

$$\sigma_1^{\text{pl}} = \sigma_{1\text{eq}}^{\text{pl}} + \sigma_{1\text{noneq}}^{\text{pl}}, \tag{14}$$

where

$$\sigma_{1p}^{\text{pl}} = \rho c_p v \tag{15}$$

is the Hugoniot stress. The nonequilibrium part $\sigma_{1\text{eq}}^{\text{pl}}$ of stress is expressed in terms of the spherical component P and deviator S_1 as

$$v_{1\text{noneq}}^{\text{pl}} = S_1 - P. \tag{16}$$

Large-scale velocity fluctuations at the level of mesoscale play the same role as thermal fluctuations at the level of the microscopic scale —they determine a nonequilibrium addition to the mean pressure at the mesoscale in terms of the variance D^2 in velocities of mesoparticles:

$$P = \rho D^2. \tag{17}$$

Since we want to take into account only the effect of dispersion on the shock wave propagation in a heterogeneous medium, we set $S_1 = 0$.

The substitution of Eqs. (13), (15), and (17) into Eq. (4) yields

$$c_1^2\frac{\partial^2 v}{\partial x^2} - \frac{\partial^2 v}{\partial t^2} = c_1^2\frac{\partial^2 v_{\text{eq}}^{\text{pl}}}{\partial x^2} + c_1^2\frac{\partial^2}{\partial x^2}\frac{\partial D^2}{\partial v}$$
$$- \frac{\partial^2}{\partial x \partial t}(c_p v_{\text{eq}}^{\text{pl}}) - \frac{\partial}{\partial t}\left(\frac{\partial D^2}{\partial x}\right). \tag{18}$$

We restrict our consideration to processes in which the plastic-wave velocity is close to the longitudinal speed in the medium. In this case, the first and third terms on the right-hand side of Eq. (18), which refer to the equilibrium component of the mass-transfer velocity, offset each other. Equation (18) can be reduced to the form

$$c_1^2\left[1 - 2\frac{D\partial D}{v\partial v}\right]\frac{\partial^2 v}{\partial x^2} - \frac{\partial^2 v}{\partial t^2} = 2\frac{\partial^2}{\partial x^2}\left[v\frac{D\partial D}{v\partial v}\right]$$
$$+ \frac{\partial v}{\partial x}\frac{\partial}{\partial x}\left[\frac{D\partial D}{v\partial v}\right] + 2v\frac{\partial^2}{\partial x^2}\left[\frac{D\partial D}{v\partial v}\right] \tag{19}$$
$$- 2v\frac{\partial}{\partial t}\left[\frac{D\partial D}{v\partial x}\right] - 2\frac{\partial v}{\partial t}\left[\frac{D\partial D}{v\partial x}\right].$$

The left-hand side of this equation is the wave operator, where the wave propagation velocity depends on the rate of variation in the standard deviation and mean velocity:

$$c_p^2 = c_1^2\left[1 - 2\frac{D\partial D}{v\partial v}\right]. \tag{20}$$

It is seen that, under the condition

$$\frac{D\partial D}{v\partial v} = \frac{D\dot{D}}{v\dot{v}} = \frac{1}{2}, \tag{21}$$

Eq. (21) is reduced to the equation

$$\frac{\partial^2 v}{\partial t^2} = -\frac{1}{2c_1}\left(\frac{\partial v}{\partial t}\right)^2. \tag{22}$$

This equation describes processes in which decay is proportional to acceleration squared. Thus, the wave motion under condition (21) changes to a sharp decrease in the particle velocity. It is also seen that the condition of the catastrophic break of the plastic front is determined by both the ratio of the standard deviation of velocities to the mean velocity of particles and the ratio of their accelerations.

Let us test the above criterion by applying it to the time profiles of the velocity and standard deviation shown in Fig. 1. The steepest part of the plastic front AB of the mean-velocity profile for the first set of 30XH4M steel (Fig. 1a) corresponds to the following rate of change in the mean velocity of particles (acceleration):

$$\dot{v} = \frac{dv}{dt} = \frac{25 \times 10^2 \text{ cm/s}}{(344 - 320) \times 10^{-9} \text{ s}} = 3.14 \times 10^{11} \text{ cm/s}^2.$$

Within the same time interval, the rate of change in the standard deviation of velocities equals

$$\dot{D} = \frac{dD}{dt} = \frac{25.9 \times 10^2 \text{ cm/s}}{(344 - 320) \times 10^{-9} \text{ s}} = 0.15 \times 10^{11} \text{ cm/s}^2.$$

The absolute values of the mean velocity and standard deviation of velocities at the point A are equal to $v = 290$ m/s and $D = 25.9$ m/s. Thus, $\frac{\dot{D}}{\dot{v}} = 0.047$, $\frac{D}{v} = 0.07$, and $\frac{D}{v}\frac{\dot{D}}{\dot{v}} = 0.003 \ll 0.5$, which corresponds to the evolutional regime of energy exchange, in which the plastic front smoothly approaches its maximum value.

Similar calculations for the profiles of mean velocity and standard deviation of velocities (see Fig. 1b) yield $v = 160$ m/s, $D = 140$ m/s, $\dot{v} = 0.3 \times 10^{11}$ m/s^2, $\dot{D} = 0.75 \times 10^{11}$ m/s^2, and $\frac{D}{v}\frac{\dot{D}}{\dot{v}} = 2.18 > 0.5$, which corresponds to the condition of the catastrophic regime of energy exchange (20). In this case, at point B of the pro-

file of mean velocity, the break of the plastic front occurs, and the free-surface velocity on the plateau of the compression pulse is much lower than the impact velocity corresponding to the symmetric collision. This decrease in mean velocity is due to the pumping of momentum and energy from the macroscale to the mesoscale. In our case, the "shortage" of free-surface velocity at the pulse plateau equals $V_{\text{pulse}} - u_{\text{fs}} = (320 - 160)$ m/s = 160 m/s.

Thus, different tempering regimes for 30XH4M steel provide different degrees of mobility for its structure, which, in turn, corresponds to different regimes of energy exchange between macroscopic and mesoscopic scales of dynamic deformation.

The condition obtained above for a change in the regime of energy exchange between the mesoscopic and macroscopic levels of dynamic deformation can play a key role not only in materials science but also in the prognostication and prediction of earthquakes. At present, many diagnostic stations are operating in various regions of the globe to detect crustal motions of the Earth. They record both smooth (evolutional) motion of tectonic plates and chaotic small motions. This information may be used to apply criterion (20) for the prediction of earthquakes in different regions of the Earth.

REFERENCES

1. V. I. Vladimirov, V. N. Ivanov, and N. D. Priemskiĭ, in *Physics of Strength and Plasticity* (Nauka, Leningrad, 1986), pp. 69–80 [in Russian].

2. G. Ravichandran, A. J. Rosakis, J. Hodowany, and P. Rosakis, in *Shock Compression of Condensed Matter-2001*, Ed. by M. D. Furnish, N. N. Thadhani, and Y. Y. Horie (American Institute of Physics, New York, 2002), pp. 557–562.

3. Yu. I. Mescherykov and A. K. Divakov, Dymat. J. **1**, 271 (1994).

4. A. M. Kosevich, *Dislocations in the Theory of Elasticity* (Nauka, Moscow, 1978) [in Russian].

5. Yu. I. Mescheryakov, in *High-Pressure Shock Compression of Solids VI* (Springer, Berlin, 2002), pp. 169–213.

6. T. Kihara and O. Aono, J. Phys. Soc. Jpn. **18**, 837 (1963).

7. J. Hubburd, Proc. Roy. Soc. A **260**, 114 (1960).

Translated by Yu. Mescheryakov